Numerical studies of turbulent Rayleigh-Bénard convection in closed cells: boundary layer dynamics and large scale patterns

Dissertation

zur Erlangung des akademischen Grades

Doktoringenieur

(Dr.-Ing.)

vorgelegt der

Fakultät für Maschinenbau der

Technischen Universität Ilmenau

von Herrn

M.Sc. Mikhail Ovsyannikov

1. Gutachter: Univ.-Prof. Dr. rer. nat. habil. Jörg Schumacher
2. Gutachter: apl. Prof. Dr.-Ing. habil. Christian Karcher
3. Gutachter: Dr. Olga Shishkina

Tag der Einreichung: 24.01.2018
Tag der wissenschaftlichen Aussprache: 17.09.2018

urn:nbn:de:gbv:ilm1-2018000457

Abstract

The present work consists of two parts devoted to study of different aspects of Rayleigh-Bénard convection (RBC) in closed cylindrical and rectangular cells.
The first part is devoted to development of a model of a laminar boundary layer flow. The model based on the classical theory by L. Prandtl incorporates effects of the buoyancy and the longitudinal pressure gradient, which have so far been considered separately. The aim of the development is to improve agreement between results of the model and data obtained in three-dimensional direct numerical simulations (DNS) of convection flows at two Prandtl numbers in a particular cylindrical cell. The improvement is achieved for a lower Prandtl number (Pr), while for a higher Pr the inclusion of the buoyancy does not give significant improvement. A possible explanation related to a coherent structure is provided.
The second part of the work is related to DNS of a turbulent convection flow in a closed rectangular box with a large aspect ratio. At present most of numerical studies of RBC have been performed for convection in closed cylindrical cells or between two horizontal plates without lateral constraints. The presence of additional lateral rigid walls in a rectangular cell imposes limitations on the use of the most effective numerical methods applied for solving equations of an incompressible convection flow. The effectiveness of a numerical method is especially important for RBC in large-aspect-ratio cells. In the frame of the present work a numerical method based on multigrid solvers included in a software package is developed for solving elliptic partial differential equations in a rectangular box. The solution method is integrated into an existing numerical scheme, and a code for performing DNS of RBC in large-aspect-ratio cells is developed.
A problem related to the ergodicity is studied, and data used for analysis are obtained in DNS of convection flows in large-aspect-ratio rectangular cells performed by the new code. The ergodic hypothesis states that time-averaged fluid dynamic fields are identical to those obtained by averaging over statistical ensemble. In the case of turbulent flows, the ergodic hypothesis has not been proved yet. The aim of this study is to find similarities and differences between time-averaged fluid dynamic fields and those averaged over ensemble. It is found that large coherent structures are persistent in a flow after averaging over a long period of time, while the averaging over ensemble tends to destroy these structures. Nevertheless, many macroscopic parameters and second-order moments of some quantities are very close despite the type of averaging. The analysis of the turbulent viscosity and the turbulent thermal diffusivity reveals some differences but requires a deeper study.

Zusammenfassung

Die vorliegende zweiteilige Arbeit beschäftigt sich mit verschiedenen Aspekten der Rayleigh-Benard Konvektion (RBK) in geschlossenen zylindrischen und rechteckigen Zellen. Im ersten Teil wird ein theoretisches Modell für eine laminare Grenzschichtströmung entwickelt, in dem sowohl der Auftrieb und als auch der longitudinale Druckgradient erstmals gemeinsam berücksichtigt werden. Es basiert auf der klassischen Theorie von L. Prandtl. Dieses Modell soll eine bessere Übereinstimmung mit Daten aus dreidimensionalen, direkten numerischen Simulationen (DNS) von Konvektionsströmungen in einer zylindrischen Zelle mit zwei unterschiedlichen Prandtlzahlen aufweisen als bereits bestehende Modelle. Für eine niedrige Prandtlzahl konnte eine Verbesserung erreicht werden. Mit Einbeziehung des Auftriebs für höhere Prandtlzahlen ergeben sich signifikante Unterschiede. Eine mögliche Erklärung anhand von kohärenten Strukturen wird vorgestellt.
Der zweite Teil dieser Arbeit bezieht sich auf DNS von turbulenten Konvektionsströmungen in einer geschlossenen, rechteckigen Zelle mit großem Aspektverhältnis. Bisher wurden die meisten numerischen Untersuchungen der RBK in geschlossenen Zylindern oder zwischen zwei horizontalen Platten ohne Seitenwände gemacht. Die Seitenwände beschränken die Nutzung effizienter numerischer Methoden, welche bei inkompressiblen Konvektionsströmungen angewandt werden. Eine hohe Performance der numerischen Methode ist besonders für RBK mit großem Aspektverhältnis von Vorteil. In der vorliegenden Arbeit wurde deshalb eine numerische Methode für die Lösung elliptischer partieller Differentialgleichungen in einer rechteckigen Zelle entwickelt, die auf Mehrgitterlösern aus einem vorhandenen Programmpaket basiert. Diese numerische Methode ist in ein bestehendes Programm für RBK integriert worden. Der so erweiterte numerischen Code ermöglicht DNS von RBK mit großem Aspektverhältnis.
Eine Fragestellung zur Ergodizität von turbulenter RBK wird hierbei näher untersucht. Dazu werden Daten genutzt, welche mit dem neuen Code aus DNS mit großem Aspektverhältnis in rechteckigen Zellen erhalten wurden. Die Ergodenhypothese besagt, dass das Zeitmittel der hydrodynamischen Felder mit deren Ensemble-Mittelwert übereinstimmt. Für turbulente Strömungen wurde die Ergodenhypothese bislang nicht bewiesen. Das Ziel der Untersuchungen ist es, Gemeinsamkeiten und Unterschiede zwischen Zeitmittel und Ensemblemittel zu finden. Es stellt sich heraus, dass bei einer Zeitmittelung über ein langes Zeitfenster große, kohärente Strukturen der Strömung bestehen bleiben. Bei Ensemble-Mittelung werden diese dagegen zerstört. Dennoch stimmen viele makroskopische Parameter und Momente zweiter Ordnung einiger Größen bei den zwei unterschiedlichen Arten der Mittelung überein. Die Analyse der turbulenten Viskosität und der turbulenten thermischen Diffusivität zeigt dagegen einige Unterschiede und erfordert weitere Untersuchungen.

Contents

Chapter 1

Introduction and scope of thesis

1.1 Convective phenomena

A fluid with an inhomogeneous temperature distribution in the presence of the gravitational field can remain in mechanical equilibrium under certain conditions. If the temperature difference is sufficiently large, the equilibrium becomes linearly unstable, and motion of the fluid appears. Under some conditions the equilibrium state is not possible at all due to infinitesimal disturbances of the temperature. In both cases, the temperature difference leads to the motion of the fluid which tends to equalize the temperature inhomogeneity, and this type of motion is called thermal convection (see e.g. [1]).

One can note that such a situation can be observed almost everywhere, and convective phenomena play an important role in physical processes while transferring mass, momentum and heat. A long list of works on convection flows which occur in natural and technological systems can be found in reviews [2; 3]. Here only several examples of convection systems are briefly mentioned to illustrate how this phenomenon is common. In the atmosphere the motion of air masses due to convection caused by the temperature difference between hotter bottom and colder top layers of air highly influences climate. In the mantle of Earth, where the temperature difference appears between the hotter core and the colder crust, the convective motion has direct effect on plate tectonics, earthquakes, and so on. Convection phenomena are also observed in oceans, in stars (and particularly in the Sun), and in many other natural systems. But as it is typical for natural systems, in most cases the processes are not controllable and very complex, and can only be observed and studied to obtain some knowledge and information. In contrast, engineering systems where convection takes place can be designed properly, if fundamental principles of convective phenomena are known to some

extent. Typical problems which are important from a practical point of view can be those related to ventilation and cooling, when it is necessary to cool down some space or a component of a mechanical or electronic device and to remove a hotter fluid or air effectively.

From a scientific point of view convection systems are interesting for studying problems of hydrodynamic instability and phenomena of transition to a turbulent state as well as turbulence itself (see e.g. [1] or more comprehensive [4]). A systematic study of convection instability began from experiments done by H. Bénard [5], who observed regular periodic patterns in a horizontal layer of a fluid heated from below. The results obtained by Bénard were later examined by Lord Rayleigh [6], who theoretically studied the problem of stability by applying a simplified model and determined parameters of a fluid near the onset of convection. Moreover, convection systems are convenient for investigating in such fields as pattern formation and the theory of chaos (see e.g. [7; 8]).

This ubiquitous occurrence of convection, its tremendous influence on physical processes, and related important problems make it reasonable to study fundamental principles of convection flows both experimentally and numerically. Most of convection phenomena in real systems are accompanied by other physical effects such as an imposed electromagnetic field, rotation of a system, phase transition in a fluid, radiation, thermonuclear fusion, and so on. Even without such additional phenomena, which make a process very complicated, experimental and numerical studies of convection require further simplifications discussed below in section 1.2.

1.2 Rayleigh-Bénard convection in closed cells

In laboratory experiments convection phenomena are studied in closed containers (so-called cells) due to better control of conditions and parameters of a fluid. This assures a reproducibility of the flows with similar characteristics and better conditions for eliminating accompanied effects mentioned above in section 1.1. A convection process in such a cell which is uniformly heated from below and cooled from above is referred to as a Rayleigh-Bénard convection (RBC).

Two simple types of containers are typically applied for studying convection flows: a cylindrical cell of the height H and the radius R schematically shown in figure 1.1(a), and a cell of rectangular cross section (a rectangular box) of the sizes $L \times W \times H$ in figure 1.1(b). These geometries are frequently used due to their symmetry and simplified (optical) access to the convection flow in the experiments. It should be noted that the shape of a container also plays a role,

as it influences properties of a convection flow, which is discussed in more detail below in section 3.1. To initiate convection, the bottom horizontal plate is heated, and the top horizontal plate is cooled. To observe a pure convection phenomenon caused by the temperature difference between the horizontal plates, the sidewalls are usually kept thermally isolated.

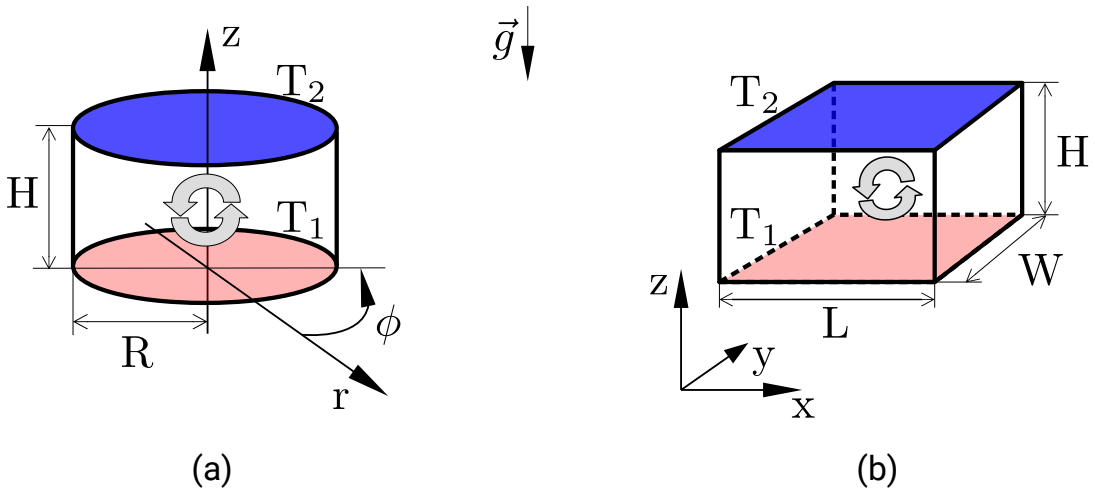

Figure 1.1: The sketches of the RBC cells: (a) the cylindrical cell; (b) the rectangular box. The parameters shown in both figures are dimensional but written without the tilde. The height of both cells is H. The cylindrical cell has the radius R. The rectangular box has the length L and the width W. The temperatures of the heated bottom and cooled top plates of the cells are T_1 and T_2, respectively. The cylindrical coordinate system (ϕ, r, z) is applied in the cylindrical cell, the Cartesian coordinate system (x, y, z) in the rectangular box. The vector $\vec{g}$ is acceleration due to gravity (opposite to the z direction of both coordinate systems). The large-scale circulation is schematically shown inside both cells.

For performing numerical simulations of RBC in a cell, the governing equations of a convection flow to be solved numerically must be specified. In a general case, any flow is described by the Navier-Stokes equations, and to simplify the solution, all parameters of a fluid (the dynamic viscosity, the thermal conductivity, etc.) are assumed to be constant (see e.g. [1]). However, certain assumptions are satisfied for RBC in a closed cell, and the general governing equations of a convection flow can be simplified. The flow velocity magnitude in a convection cell is assumed to be much smaller than the speed of sound. Thus, variations of the mass density due to changes of the pressure are neglected, and the Navier-Stokes equations are written in the simpler form for an incompressible flow. In contrast, small variations of the density are caused by inhomogeneity of the temperature. The

temperature $\tilde{T}$, the density $\tilde{\rho}$ and the pressure $\tilde{p}$ are represented as

$$\tilde{T} = \tilde{T}_0 + \tilde{T}', \qquad \tilde{\rho} = \tilde{\rho}_0 + \tilde{\rho}', \qquad \tilde{p} = \tilde{p}_0 + \tilde{p}', \tag{1.1}$$

where $\tilde{T}_0$ and $\tilde{\rho}_0$ are the mean (reference) constant temperature and density, respectively. It should be noted that all dimensional parameters are written with tilde. It is assumed that $\tilde{T}' \ll \tilde{T}_0$, $\tilde{\rho}' \ll \tilde{\rho}_0$ as well as $\tilde{p}' \ll \tilde{p}_0$. The pressure $\tilde{p}_0$ is the hydrostatic pressure at some level $\tilde{z}$ which corresponds to the mechanical equilibrium at $\tilde{T}_0$ and $\tilde{\rho}_0$. By introducing the thermal coefficient expansion $\tilde{\alpha}$ and by using $\tilde{T}$ and $\tilde{\rho}$ included in (1.1), the equation of state can be written as

$$\tilde{\rho} - \tilde{\rho}_0 = -\tilde{\alpha}(\tilde{T} - \tilde{T}_0). \tag{1.2}$$

The following governing equations for an incompressible convection flow are obtained by substituting $\tilde{p}$ and $\tilde{\rho}$ expressed in (1.1) into the Navier-Stokes equations and by using equation (1.2) (see e.g. [1; 2]):

$$\tilde{\nabla} \cdot \tilde{\boldsymbol{u}} = 0\,, \tag{1.3}$$

$$\frac{\partial \tilde{\boldsymbol{u}}}{\partial \tilde{t}} + (\tilde{\boldsymbol{u}} \cdot \tilde{\nabla})\,\tilde{\boldsymbol{u}} = -\frac{1}{\tilde{\rho}_0}\,\tilde{\nabla}\,\tilde{p}\,' + \tilde{\nu}\,\tilde{\nabla}^2\,\tilde{\boldsymbol{u}} + \tilde{\alpha}\tilde{g}\tilde{T}\,'\boldsymbol{e}_z, \tag{1.4}$$

$$\frac{\partial \tilde{T}\,'}{\partial \tilde{t}} + (\tilde{\boldsymbol{u}} \cdot \tilde{\nabla})\,\tilde{T}\,' = \tilde{\kappa}\,\tilde{\nabla}^2\,\tilde{T}'. \tag{1.5}$$

Equations (1.3)-(1.5) written in the Cartesian coordinate system with the orthonormal basis $(\boldsymbol{e}_x, \boldsymbol{e}_y, \boldsymbol{e}_z)$ are called the Oberbeck-Boussinesq equations. The following notation is applied in equations (1.3)-(1.5): $\tilde{\boldsymbol{u}}(\tilde{\boldsymbol{r}}, \tilde{t})$ is the velocity with the components $(\tilde{u}_x, \tilde{u}_y, \tilde{u}_z)$, $\tilde{\boldsymbol{r}} = (\tilde{x}, \tilde{y}, \tilde{z})$; $\tilde{g}$ the acceleration due to gravity; $\tilde{\nu}$ and $\tilde{\kappa}$ are the kinematic viscosity and the thermal diffusivity of a fluid, respectively. The main idea of the Oberbeck-Boussinesq model is that variations of the density caused by the temperature inhomogeneity are negligible and are taken into account only in the buoyancy force of the momentum equation, the last term of equation (1.4).

Similar to experiments done in containers of the simple geometries shown in figures 1.1(a), 1.1(b), numerical studies based on results of direct numerical simulations (DNS) are performed also in convection cells of these types. The reason to use cells of a simple geometry is their advantages which make possible to apply the most effective numerical methods for solving the governing equations discussed below. This fact is very crucial while performing DNS, because in general such computations are very costly, but they give the richest information

on a turbulent flow. One part of the present work is devoted to search of an effective numerical method applied for performing DNS of RBC in a rectangular cell, and more detailed information on some approaches is given in chapter 3.

To solve numerically the partial differential equations given by (1.3)-(1.5), the following boundary conditions will be applied throughout this work. The velocity has the standard no-slip condition at all rigid walls, $\tilde{\boldsymbol{u}} = 0$. The isothermal condition for the temperature is imposed at both horizontal plates: $\tilde{T}_1$ at the heated bottom plate, $\tilde{T}_2$ at the cooled top plate, $\tilde{T}_2 < \tilde{T}_1$ (see figures 1.1(a), 1.1(b)). The sidewalls are adiabatic with no heat flux, $\partial\tilde{T}/\partial\boldsymbol{n}$. In the case of a cylindrical cell, the cylindrical coordinate system is naturally applied, and equations (1.3)-(1.5) are written accordingly.

It is more convenient (especially for numerical simulations) to avoid the dimensional formulation of a problem and to express equations (1.3)-(1.5) in dimensionless units. While performing this operation, some control parameters which determine a convection system appear immediately. The following reference units are used for the dimensionless formulation of the problem (the tilde denotes dimensional quantities):

$$\tilde{H}, \qquad \Delta\tilde{T}, \qquad \tilde{U}_f, \tag{1.6}$$

where $\tilde{H}$ is the cell height, $\Delta\tilde{T}$ the temperature difference,

$$\Delta\tilde{T} = \tilde{T}_1 - \tilde{T}_2, \tag{1.7}$$

$\tilde{U}_f$ the free-fall velocity defined as

$$\tilde{U}_f = \sqrt{\tilde{\alpha}\tilde{g}\Delta\tilde{T}\tilde{H}}. \tag{1.8}$$

Moreover, in numerical simulations time is expressed in units of the free-fall time $\tilde{T}_f$ given by

$$\tilde{T}_f = \frac{\tilde{H}}{\tilde{U}_f} = \sqrt{\frac{\tilde{H}}{\tilde{\alpha}\tilde{g}\Delta\tilde{T}}}. \tag{1.9}$$

In addition to the free-fall velocity $\tilde{U}_f$ and the free-fall time $\tilde{T}_f$, the diffusive velocity $\tilde{U}_d$ and the diffusive time $\tilde{T}_d$ are also used in the analysis:

$$\tilde{U}_d = \frac{\tilde{\kappa}}{\tilde{H}}, \qquad \tilde{T}_d = \frac{\tilde{H}}{\tilde{U}_d} = \frac{\tilde{H}^2}{\tilde{\kappa}}. \tag{1.10}$$

Equations (1.3)-(1.5) are written in dimensionless units (without the tilde) by

using the reference unites given in (1.6) as follows:

$$\nabla \cdot \boldsymbol{u} = 0\,, \tag{1.11}$$

$$\frac{\partial \boldsymbol{u}}{\partial t} + (\boldsymbol{u} \cdot \nabla)\,\boldsymbol{u} = -\nabla\, p + \sqrt{\frac{Pr}{Ra}}\,\nabla^2\,\boldsymbol{u} + T\boldsymbol{e}_z, \tag{1.12}$$

$$\frac{\partial T}{\partial t} + (\boldsymbol{u} \cdot \nabla)\,T = \frac{1}{\sqrt{Ra\,Pr}}\,\nabla^2\,T. \tag{1.13}$$

The boundary conditions are the same as those applied for solving equations (1.3)-(1.5). For the velocity at rigid walls:

$$\boldsymbol{u} = 0. \tag{1.14}$$

For the temperature at the bottom plate, at the top plate, and at sidewalls, respectively:

$$T = T_1, \qquad T = T_2, \qquad \frac{\partial T}{\partial \boldsymbol{n}} = 0. \tag{1.15}$$

The main dimensionless parameters applied in numerical studies of RBC and included in equations (1.11)-(1.13) are the Rayleigh number Ra defined as

$$Ra = \frac{\tilde{\alpha}\tilde{g}\Delta\tilde{T}\tilde{H}^3}{\tilde{\nu}\tilde{\kappa}}, \tag{1.16}$$

and the Prandtl number Pr defined as

$$Pr = \frac{\tilde{\nu}}{\tilde{\kappa}}. \tag{1.17}$$

The control parameters given by (1.16) and (1.17) are determined by properties of a fluid and the height $\tilde{H}$ of a cell. In the case of convection in a cell of a simple shape (a rectangular box or a cylinder), an important parameter which specifies only the geometry of the cell is the aspect ratio Γ defined as

$$\Gamma = \frac{\tilde{L}}{\tilde{H}}, \tag{1.18}$$

where L is the diameter of a cylindrical cell, $\tilde{L} = 2\tilde{R}$, or the length of a rectangular box when the length is equal to the width, $\tilde{L} = \tilde{W}$ (the notation used is shown in figures 1.1(a) and 1.1(b)). If the horizontal dimensions of a rectangular box are not equal, two values of the aspect ratio are specified:

$$\Gamma_x = \frac{\tilde{L}}{\tilde{H}}, \qquad \Gamma_y = \frac{\tilde{W}}{\tilde{H}}, \tag{1.19}$$

where $\tilde{L}$ and $\tilde{W}$ are the length and the width of the container shown in figure 1.1(b). For a cubic container or a cylindrical cell with the diameter equal to its height, the aspect ratio is one. For laterally extended containers, $\Gamma > 1$.

Thus, to determine a convection flow in a cell uniquely and to set the geometry of the cell, it is enough to specify the Rayleigh number Ra (defined in (1.16)), the Prandtl number Pr (defined in (1.17)), and the aspect ratio Γ or the pair Γ_x, Γ_y (given by (1.18) or by (1.19)). If a problem is specified by these control parameters, equations (1.11)-(1.13) can be solved numerically.

If Ra, Pr, Γ are input parameters, the main response parameters of a convection system are the Nusselt number Nu and the Reynolds number Re. For an incompressible flow, the Nusselt number Nu, which is a dimensionless heat flux, is defined in dimensional units at a fixed coordinate $\tilde{z}$ as

$$Nu = \frac{\langle \tilde{u}_z \tilde{T} \rangle_{A,t} - \tilde{\kappa} \, \dfrac{\partial \langle \tilde{T} \rangle_{A,t}}{\partial \tilde{z}}}{\tilde{\kappa} \, \Delta \tilde{T} / \tilde{H}}. \tag{1.20}$$

The notation $\langle * \rangle_{A,t}$ used in equation (1.20) denotes averaging over time, $\langle * \rangle_t$, and averaging over area, $\langle * \rangle_A$, where the area of averaging is the area of a cross section of a horizontal plane (at the given $\tilde{z}$) and a convection cell. To obtain the vertical profile of Nu, it is computed by using equation (1.20) at every point along the vertical direction $\tilde{z}$ between the bottom and top horizontal plates of a cell. In the dimensionless formulation, equation (1.20) is written as

$$Nu = \sqrt{Ra \, Pr} \, \langle u_z T \rangle_{A,t} - \frac{\partial \langle T \rangle_{A,t}}{\partial z}. \tag{1.21}$$

In addition to the profile $Nu(z)$ computed by equation (1.21), the Nusselt number averaged over volume, Nu_V, which is also applied in analysis, is computed by averaging $Nu(z)$ over the vertical direction z, and the final equation of Nu_V is written as follows:

$$Nu_V = \sqrt{Ra \, Pr} \, \langle u_z T \rangle_{V,t} + 1, \tag{1.22}$$

where the notation $\langle * \rangle_{V,t}$ means averaging over time, $\langle * \rangle_t$, and averaging over volume, $\langle * \rangle_V$. The Reynolds number is defined in the standard way as

$$Re = \frac{\tilde{U} \tilde{H}}{\tilde{\nu}} \tag{1.23}$$

or in dimensionless units as

$$Re = \sqrt{\frac{Ra}{Pr}} \, U, \tag{1.24}$$

where the velocity U is computed by averaging the flow velocity over time and over volume and is referred to as the root mean square velocity, u_{rms}:

$$u_{rms} = \sqrt{\langle \boldsymbol{u}^2 \rangle_{V,t}}. \tag{1.25}$$

There are other ways for choosing $\tilde{U}$ included in equation (1.23) which are discussed in review [3]. The root mean square velocity defined in (1.25) is also used for computing the total kinetic energy E_{TKE}:

$$E_{\mathrm{TKE}} = \frac{1}{2} \langle \boldsymbol{u}^2 \rangle_{V,t}. \tag{1.26}$$

It should be noted that the Nusselt number Nu and the Reynolds number Re, given by (1.21) and (1.24), respectively, can be computed during numerical simulation. But one of the most important and complicated problems of RBC is to predict both response parameters, Nu and Re, in advance when knowing the control parameters Ra, Pr and Γ. A lot of efforts have been put into development of models (or so-called scaling laws) which relate the input parameters with the output data in the form of functional dependencies

$$Nu = Nu(Ra, Pr, \Gamma), \tag{1.27}$$

$$Re = Re(Ra, Pr, \Gamma). \tag{1.28}$$

By knowing these laws, it is possible to predict and to identify some notable states or regimes of a flow in a convection system, when its behaviour changes significantly. The most recent and comprehensive model developed by S. Grossmann and D. Lohse can be found in [9]. This model (also called the GL model) successfully describes many results obtained from experiments and numerical simulations. The GL model assumes the presence of a coherent structure called a large-scale circulation (LSC) or a large-scale roll shown schematically in figures 1.1(a) and 1.1(b). The existence of the LSC was proven experimentally, as it is discussed in work [9], and in the present work it is also mentioned in chapter 2. The main idea of the GL model is to divide a convection cell into two regions: the bulk of the cell, and the boundary layer (BL) near its walls. For both regions one then makes estimates of the kinetic energy dissipation rate and the thermal dissipation rate, the control quantities of this theory.

1.3 Scope of the thesis

The aim of the present work is to study some dynamical and statistical aspects of thermal convection in a closed RBC cell by means of a simplified mathematical model and three-dimensional direct numerical simulations. The work is divided into two independent parts which are related to two different subproblems of Rayleigh-Bénard convection. While the first subproblem is related to the boundary layer dynamics (chapter 2), the second subproblem is concerned with convection in large-aspect-ratio cells (chapters 3 and 4).

Chapter 2 is devoted to development of a model of a two-dimensional incompressible steady flow within the laminar boundary layer governed by Prandtl's equations. The new approach combines effects of the buoyancy and of the prescribed longitudinal pressure gradient, which were considered separately in previous BL models of this class. Because similarity solutions are not possible, the idea of searching solutions in a form of series with some perturbation parameter, suggested by E.M. Sparrow and W.J. Minkowycz in work [10], is applied to reduce the initial partial differential equations to a system of ordinary differential equations of higher order. The obtained equations were solved numerically, and their solutions were compared with corresponding profiles of three-dimensional DNS of a convection flow in a cylindrical cell of $\Gamma = 1$.

Chapter 3 describes development of a numerical method for solving two elliptic partial differential equations which arise in the numerical finite difference scheme applied for solving the governing equations of an incompressible convection flow in a closed rectangular cell. The code was integrated into a program applied initially for performing DNS of duct flows, and the obtained solver is applied for DNS of turbulent convection flows in closed rectangular cells with large aspect ratios. Due to large computational costs for numerical simulations of such problems, the main requirements of the method are efficiency and high level of parallelization. Different publicly available software packages were tested at parameters close to those of the problem of the convection flow at hand.

Chapter 4 reports results of a numerical examination of the ergodic hypothesis in a turbulent convection flow in a closed rectangular cell of a large aspect ratio. Data for analysis were obtained in DNS of a turbulent convection flow performed by the new code. The problem requires a special setup of initial conditions and careful settings, and involves thorough analysis to find similarities and differences of two approaches applied independently for mathematical study of turbulence and for its experimental investigation.

Chapter 2

Boundary layer model

2.1 Motivation

The boundary layers of the velocity and temperature field play a central role for a deeper understanding of the mechanisms of turbulent momentum and heat transfer in thermal convection flows [2; 3]. In the simplest setting of Rayleigh-Bénard convection they form in the vicinity of the isothermal plates at the top and bottom. In the past decade, intensive experimental, numerical and theoretical studies of the structure of the boundary layers in convection have been conducted (see [2; 3]). In particular, direct numerical simulations [11; 12; 13; 14] demonstrated that the boundary layer structure is time-dependent and fully three-dimensional. The latter property can be clearly assigned with the detachment of thermal plumes, hot (cold) fragments of the thermal BL which rise (fall) into the bulk of the convection layer. The boundary layers in turbulent RBC are found to be neither fully laminar nor fully turbulent, at least for the range of Rayleigh numbers Ra that is accessible for fully resolved simulations, i.e. $Ra \leq 10^{12}$. This behavior has also been confirmed in recent particle image velocimetry measurements at a Rayleigh number $Ra \approx 10^{12}$ [15]. It was also shown in [13] that the pressure gradient fluctuates strongly across the convection BL. In addition, all simulation studies verified that the BL dynamics is connected in multiple ways with a large-scale circulation which always occurs in a closed convection cell as it is discussed in more detail in [3]. When the diameter or side length equals the height, one expects a single large-scale circulation roll that fills the closed cell.

Although direct numerical simulations and laboratory studies gave us deep insights into the BL dynamics, it remains interesting and necessary to extend the theoretical foundations for the dynamics in the BL of turbulent convection. One way to progress in this direction is to extend classical and dimensionally

reduced BL models that exhibit similarity solutions [16] to perturbative expansions in form of series solutions [10]. Such an extension is in line with a dynamical coupling of velocity and temperature fields. How well do such extended and joint models for velocity and temperature approximate the BL dynamics in turbulent convection? The motivation for such a step stems from the frequent use of BL models in scaling theories for the global momentum and heat transfer across the convection layer. For example, BL models of the Prandtl-Blasius (PB) type [16] are used in the scaling theory developed by Grossmann and Lohse [9]. The BL model is necessary there to predict the mean BL thicknesses in order to split the dissipation rates for kinetic energy and temperature variance into BL and bulk contributions. The original PB boundary layer with a zero pressure gradient is also known as the forced convection BL. It is one limiting case. Another limit is the free or natural convection BL [17; 18], i.e., a heated plate without any prescribed inflow. The latter case is frequently discussed in the context of plume formation in turbulent convection [19]. Perturbative expansions to mixed convection which start either from the forced or free convection limits, respectively, have been discussed for example by Sparrow and Minkowicz [10] and Hieber [20]. Such expansions have also been compared with local sequences of the BL dynamics in turbulent convection [13]. In all cases, differences between BL theory predictions and data obtained from direct numerical simulations of RBC have been found, particularly in the range for which the mean temperature and velocity profiles cross over from a linear viscous behavior to a constant value.

Very recently, the BL theory has been adapted successfully to the particular situation which is observed in closed convection cells. The presence of the LSC and the resulting contributions to the pressure gradient have been incorporated by an adaption of the classical Falkner-Skan boundary layer model [21] to a closed cylindrical RBC cell [22], the typical configuration in most laboratory experiments. In detail, the authors took advantage of the fact that the LSC is always accompanied by smaller recirculation rolls close to the edges of the cell. These recirculation rolls were used to determine the starting point of the BL. As a result of this extension, the agreement between model predictions and simulation results could be improved. In a further application of this framework to larger Prandtl numbers $Pr \geq 1$ [23], it was found that the match between model and data is diminished.

This sets the stage for our present work. In the following, we want to combine the efforts which have been discussed in [13] and [22; 23] and present a BL model which is a perturbative expansion of the RBC-adapted Falkner-Skan model with

respect to buoyancy effects. We obtain boundary layer equations which are derived from the Boussinesq equations for a two-dimensional, incompressible and steady flow. The prescribed pressure gradient is thought to be induced by the LSC. Furthermore, buoyancy forces in the vertical direction are not neglected, in contrast to the Falkner-Skan model applied in [22]. We will also show that the buoyancy force contributes to the overall longitudinal pressure gradient. By combination of the prescribed pressure gradient and the buoyancy force in the BL model, we want to answer two questions. Does such an extension of the Falkner-Skan model further improve the agreement between BL model and numerical data? Will free convection contributions due to buoyancy become increasingly important as the Prandtl number of the working fluid is increased?

Obtained solutions of equations of the developed model are compared with data obtained from DNS, and the analysis of results is provided at the end of this chapter. The content of the present chapter was published in [24].

2.2 Numerical simulations in cylindrical cell

Data used for the comparison with the model solutions were obtained from three-dimensional DNS of a turbulent convection flow in a cylindrical cell of the aspect ration one schematically shown in figure 1.1(a). Equations (1.11)-(1.13) are written in the cylindrical coordinate system with components ϕ, r, z and solved numerically. In this system the velocity field $\boldsymbol{u}$ has azimuthal u_ϕ, radial u_r, and axial u_z components. The numerical solution of the governing equations is based on the finite volume method. The detailed explanation of the numerical method for solving equations (1.11)-(1.13) is given in [13; 25; 26].

Two sets of data from the DNS performed in advance were provided. The DNS for generating the first data set were performed at $Ra = 3 \times 10^9$ and $Pr = 0.7$ ($\Gamma = 1$) on exactly the same numerical grid as in work [13] by the same co-author, who also generated the second data set at $Ra = 3 \times 10^9$ and at the larger Prandtl number $Pr = 7$ ($\Gamma = 1$). The sufficient resolution of the BL at $Pr = 0.7$ is assured and was discussed in [13; 27]; the grid resolution for the DNS at $Pr = 7$ was increased. The parameters of the problems and the configuration of the applied grids are given in table 2.1.

Table 2.1: Parameters of DNS: N_ϕ, N_r, N_z are the numbers of azimuthal, radial and axial nodes, respectively, Nu is the Nusselt number, N_{BL} is the number of axial nodes within the thermal BL, N_s is the number of snapshots available for processing, t_s is the corresponding time interval (in units of T_f).

Ra	Pr	Γ	N_ϕ	N_r	N_z	Nu	N_{BL}	N_s	t_s
3×10^9	0.7	1	512	301	360	90 ± 1	17	850	42
3×10^9	7	1	600	321	441	91 ± 1	14	201	200

2.3 Derivation of boundary layer model

2.3.1 Two-dimensional boundary layer equations

For completeness, the boundary layer equations and their simplification are given first. All classical BL models are two-dimensional and assume a steady flow. In addition, the classical BL theory applied here was developed for the laminar flow within the BL. The transition to the turbulent regime of the boundary layer flow in a cylindrical RBC cell is thoroughly discussed in [12] and in [9]. Particularly, in [12] for the small Prandtl number $Pr = 0.786$ close to our $Pr = 0.7$, the estimated critical Rayleigh number is $Ra^{crit} \sim 10^{14}$. In [9] it is reported that the transition happens near $Ra^{crit} \approx 10^{14}$ for $Pr = 1$ and $Ra^{crit} \approx 10^{16}$ for $Pr = 0.025$. All these estimations are greater by more than five orders of magnitude than $Ra = 3 \times 10^9$ used in the DNS for generating the data to be compared, and the turbulent flow within the BL is not expected in these simulations. The most significant restriction of all BL models which are based on the classical theory developed by Prandtl is the existence of the potential flow outside the BL, when the flow velocity $\boldsymbol{u}$ satisfies $\operatorname{rot} \boldsymbol{u} = 0$, and a scalar function $\phi = \phi(x, y, z)$, $\boldsymbol{u} = \operatorname{grad} \phi$, exists. This kind of flow cannot be present in a turbulent convection system by default, but nevertheless, these BL models are still applied to approximate the BLs in a RBC cell as it is said above in section 2.1. In this work the BL model is developed assuming the existence of the potential outer flow, and the obtained solutions are compared with the results of the DNS of the turbulent convection flows described above in section 2.2.

The BL model is derived from the Boussinesq equations given by (1.3)-(1.5). For the sake of simplicity, all dimensional units are written without the tilde until section 2.3.3. Moreover, in the current section the components of the velocity $\boldsymbol{u} = (u_x, u_y, u_z)$ are denoted by $u = u_x$, $v = u_y$, and $w = u_z$. Thus, equations (1.3)-(1.5) are written for a two-dimensional steady flow, when $\partial/\partial y = 0$ and

$\partial/\partial t = 0$, as follows:

$$u\frac{\partial u}{\partial x} + w\frac{\partial u}{\partial z} = -\frac{1}{\rho}\frac{\partial p}{\partial x} + \nu\left(\frac{\partial^2 u}{\partial x^2} + \frac{\partial^2 u}{\partial z^2}\right), \tag{2.1}$$

$$u\frac{\partial w}{\partial x} + w\frac{\partial w}{\partial z} = -\frac{1}{\rho}\frac{\partial p}{\partial z} + \nu\left(\frac{\partial^2 w}{\partial x^2} + \frac{\partial^2 w}{\partial z^2}\right) + \alpha g(T - T_{mid}), \tag{2.2}$$

$$\frac{\partial u}{\partial x} + \frac{\partial w}{\partial z} = 0, \tag{2.3}$$

$$u\frac{\partial T}{\partial x} + w\frac{\partial T}{\partial z} = \kappa\left(\frac{\partial^2 T}{\partial x^2} + \frac{\partial^2 T}{\partial z^2}\right). \tag{2.4}$$

Here, the temperature $T_{mid} = (T_1 + T_2)/2$ is considered as the temperature outside the BL. Following ref. [16], equations (2.1)–(2.4) are further reduced to

$$u\frac{\partial u}{\partial x} + w\frac{\partial u}{\partial z} = -\frac{1}{\rho}\frac{\partial p}{\partial x} + \nu\frac{\partial^2 u}{\partial z^2}, \tag{2.5}$$

$$\frac{1}{\rho}\frac{\partial p}{\partial z} = \alpha g(T - T_{mid}), \tag{2.6}$$

$$\frac{\partial u}{\partial x} + \frac{\partial w}{\partial z} = 0, \tag{2.7}$$

$$u\frac{\partial T}{\partial x} + w\frac{\partial T}{\partial z} = \kappa\frac{\partial^2 T}{\partial z^2}. \tag{2.8}$$

In the classical theory (see ref. [16]), the gradient of the pressure p (within the BL) in the vertical direction is assumed to be zero, i.e. $\partial p/\partial z = 0$, giving the distribution of $p = p(x)$. Here the term on the right-hand side of equation (2.6) is not neglected, and the pressure p depends both on x and on z, i.e. $p = p(x, z)$. This pressure can be decomposed and expressed as the sum of the pressure p_h at some height outside the BL, $p_h = p(x, h)$, and an additional term as follows:

$$p(x, z) = p(x, h) + g\int_z^h \rho(x, \hat{z})\,\mathrm{d}\hat{z}\,. \tag{2.9}$$

The locations of the pressure p and its component p_h included in (2.9) are shown in figure 2.1. The pressure gradient in x direction is found from (2.9) by

$$\frac{\partial p}{\partial x} = \frac{\partial p_h}{\partial x} + g\frac{\partial}{\partial x}\int_z^h \rho(x, \hat{z})\,\mathrm{d}\hat{z}\,, \tag{2.10}$$

with the dummy variable $\hat{z}$. With the Boussinesq approximation

$$\rho(x, z) - \rho_\infty = \rho_\infty\alpha(T_\infty - T(x, z)), \tag{2.11}$$

equation (2.10) is rewritten as

$$\frac{\partial p}{\partial x} = \frac{\partial p_h}{\partial x} + \rho_\infty \alpha g \frac{\partial}{\partial x} \int_z^h (T_\infty - T(x, \hat{z}))\, \mathrm{d}\hat{z}. \tag{2.12}$$

If $\rho_\infty = \rho$, $T_\infty = T_{mid}$ and $T' = T - T_{mid}$ then the final expression of the longitudinal pressure gradient follows to

$$\frac{\partial p}{\partial x} = \frac{\partial p_h}{\partial x} - \rho \alpha g \frac{\partial}{\partial x} \int_z^h T'(x, \hat{z})\, \mathrm{d}\hat{z}. \tag{2.13}$$

The first term on the right-hand side of equation (2.13) is the prescribed pressure gradient outside the BL which is induced by forced convection. The integral on the right-hand side of (2.13) is caused by variations in density, and it does not vanish due to the growth of the boundary layer thickness. Here, it is assumed that the density variations contribute only to the buoyancy force. By substituting the longitudinal pressure gradient from (2.13) into (2.5), the final set of equations of the boundary layer can be written as follows:

$$u\frac{\partial u}{\partial x} + w\frac{\partial u}{\partial z} = -\frac{1}{\rho}\frac{\partial p_h}{\partial x} + \alpha g \int_z^\infty \frac{\partial T'}{\partial x}\, \mathrm{d}\hat{z} + \nu \frac{\partial^2 u}{\partial z^2}, \tag{2.14}$$

$$\frac{\partial u}{\partial x} + \frac{\partial w}{\partial z} = 0, \tag{2.15}$$

$$u\frac{\partial T}{\partial x} + w\frac{\partial T}{\partial z} = \kappa \frac{\partial^2 T}{\partial z^2}, \tag{2.16}$$

where the upper limit of the integral, h, is replaced by infinity without any loss of generality.

2.3.2 Falkner-Skan model and large-scale flow

Falkner and Skan [21] considered the general case of a two-dimensional incompressible steady boundary layer flow with a prescribed longitudinal pressure gradient, when the vertical component of the pressure gradient is neglected within the BL. Thus, the pressure p within the BL depends only on the horizontal coordinate x. Due to the assumption of the thin BL (with respect to a characteristic dimension of a body which is flowed), the streamlines of the outer flow are almost parallel to the surface of the body, and the distribution of the pressure $p(x)$ within the BL is the same as the one outside the BL. Assuming that the outer flow is potential, the horizontal component of the pressure gradient (or the prescribed longitudinal pressure gradient) is connected with the velocity $U = U(x)$ outside

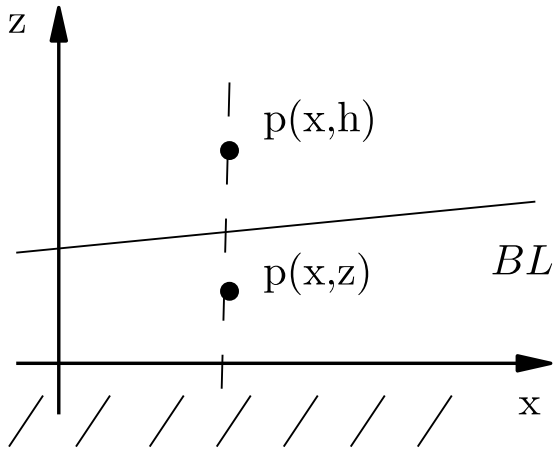

Figure 2.1: The sketch of the locations of the pressure p (defined within the BL) and its component p_h (outside the BL).

the BL via Bernoulli's equation. The velocity U of the flow outside the BL in [21] has a form of a power law:

$$U = U_0\, x^k\,, \tag{2.17}$$

with U_0 and k being constants. It was shown in [16; 22] that the prescribed flow (2.17) corresponds to a flow along a corner with an angle Ω which will be defined further below. Shishkina et al. [22] showed that such corner flow is present in closed convection cells of aspect ratio one. In this case smaller recirculation rolls form in the vicinity of the edges. These smaller rolls vary in size and intensity and have the opposite spin as the LSC roll. In ref. [22] it is shown in detail, how the power k of (2.17) is related to the angle Ω.

The recirculation flow in the corner together with the LSC roll can be seen in figures 2.2(a) and 2.2(b). We show a plot of the two-dimensional velocity field that is spanned by components u_χ and u_z. The new coordinate χ runs along the radial direction. Thus $\chi \in [-0.5, 0.5]$ and $z \in [0, 1]$. Consequently, u_χ is defined as

$$u_\chi = -u_r \quad \text{if} \quad \chi < 0, \tag{2.18}$$

$$u_\chi = u_r \quad \text{if} \quad \chi \geq 0. \tag{2.19}$$

In particular for the time averaged flow in figure 2.2(a), the angle Ω can be clearly defined by the lines $\overline{AC}$ and $\overline{C0}$, i.e. $\Omega = \angle AC0 \neq 0$. The line $\overline{AC}$ separates the LSC roll and the secondary recirculation roll. Such a secondary roll is always found at the side wall where the LSC roll is downwelling. Points A at

the left sidewall and C at the bottom plate are found as the locations with zero wall shear stress τ_w,

$$A: \quad \tau_w = \rho\nu \frac{\partial u_z}{\partial \chi}\bigg|_{\chi=-0.5} \quad \text{with} \quad \tau_w = 0\,, \tag{2.20}$$

$$C: \quad \tau_w = \rho\nu \frac{\partial u_\chi}{\partial z}\bigg|_{z=0} \quad \text{with} \quad \tau_w = 0\,. \tag{2.21}$$

With line segments $\overline{BA} = d_v$ and $\overline{BC} = d_h$ given, the angle $\angle ACB$ is computed. The angle $\Omega = \pi - \angle ACB$ is computed as (see also figure 2.4(b))

$$\Omega = \pi - \arctan\left(\frac{d_v}{d_h}\right). \tag{2.22}$$

In addition, figure 2.2(b) shows an instantaneous snapshot for comparison. The same features are observed, but much less pronounced as in the time average. According to [22], the power law exponent k of (2.17) is directly related to the angle Ω by

$$k = \frac{\pi}{\Omega} - 1. \tag{2.23}$$

With these relations, the momentum equation (2.5) is reduced to the Falkner-Skan equation. The energy equation (2.8) is in parallel converted to an ordinary differential equation which was first obtained by Pohlhausen [28]. In the classical Falkner-Skan model, the temperature field is treated as a passively advected scalar field.

2.3.3 Extended boundary layer model

We derive now the extended boundary layer model for joint effects of prescribed pressure gradient and buoyancy. From now on, all dimensional parameters are denoted with a tilde, $\tilde{x}$, $\tilde{U}$, etc., and non-dimensional ones are written as $x = \tilde{x}/\tilde{H}$, $U = \tilde{U}/\tilde{U}_f$, etc.

Equations (2.14) and (2.16) are coupled and similarity solutions are not possible. Sparrow and Minkowycz [10] suggested therefore to include the buoyancy effect as a small perturbation to a forced convection problem and to search for series solutions. We will apply the same ansatz. The unperturbed equations are given here by the Falkner-Skan and Pohlhausen equations, respectively. Thus the free-stream velocity outside the BL is set to the following power law,

$$\tilde{U} = \tilde{U}_0\, x^k. \tag{2.24}$$

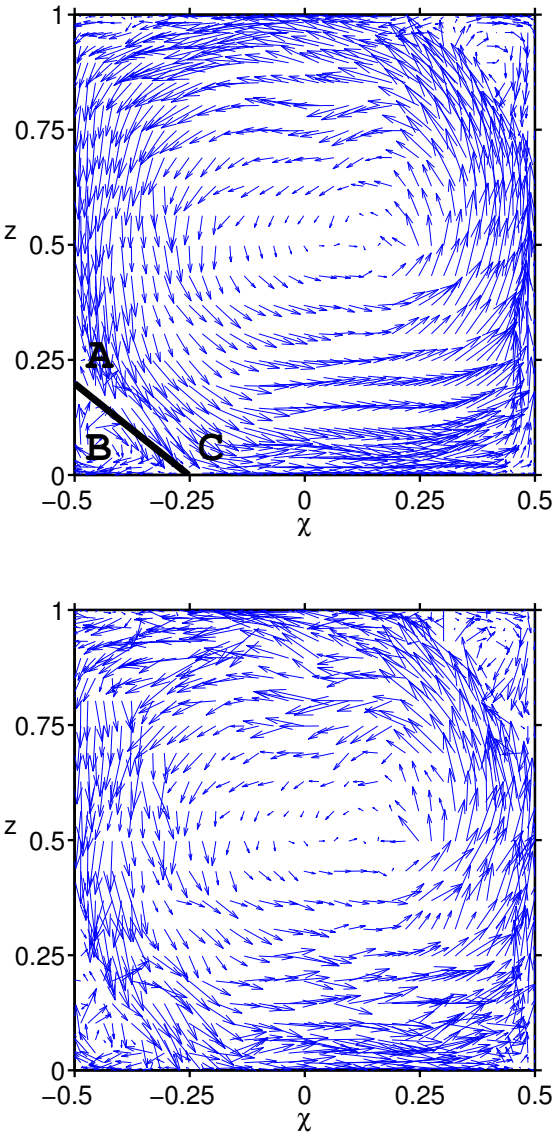

Figure 2.2: The two-dimensional velocity field (u_χ, u_z) in the vertical plane through the center line of the cylindrical cell. Simulation data are for $Ra = 3 \times 10^9$ and $Pr = 0.7$. (a) Field which is averaged over 1.2 T_f. Such a field will be used for the comparison with the BL model. We also indicate the three points which are used for the definition of Ω. (b) Instantaneous snapshot of the same data set.

The Falkner-Skan equation is derived by introducing a dimensionless stream function $f = f(\xi)$ depending on the similarity variable ξ (see [22]):

$$\tilde{\psi} = \tilde{\nu} B x^n f(\xi), \tag{2.25}$$

$$\xi = z B n x^{n-1}, \tag{2.26}$$

where $\tilde{\psi}$ is the dimensional stream function which is derived from continuity

equation (2.15). The constants n and B which enter equations (2.25) and (2.26) are defined as

$$n = \frac{k+1}{2}, \quad B = \sqrt{\frac{1}{n}}\sqrt{\frac{\tilde{U}_0\tilde{d}}{\tilde{\nu}}}. \tag{2.27}$$

In addition, a dimensionless temperature $\theta = \theta(\xi)$ is defined as

$$\theta = \frac{\tilde{T} - \tilde{T}_{mid}}{\Delta\tilde{T}/2}\,. \tag{2.28}$$

The series solutions are given by

$$f(\xi,\varepsilon) = f_0(\xi) + \sum_{m=1}^{\infty} \varepsilon^m f_m(\xi), \tag{2.29}$$

$$\theta(\xi,\varepsilon) = \theta_0(\xi) + \sum_{m=1}^{\infty} \varepsilon^m \theta_m(\xi), \tag{2.30}$$

where the leading terms f_0, θ_0 are solutions of the Falkner-Skan and Pohlhausen equations, respectively. Higher order terms stand for contributions due to buoyancy.

The introduced variable ε is referred to as the perturbative parameter which measures the strength of free relative to forced convection. It is given by

$$\varepsilon = \frac{\left|\tilde{\alpha}\tilde{g}\,\dfrac{\partial}{\partial\tilde{x}}\displaystyle\int_{\tilde{z}}^{\infty}\tilde{T}'(\tilde{\lambda})\,\mathrm{d}\tilde{\lambda}\right|}{\left|\dfrac{1}{\tilde{\rho}}\,\dfrac{\partial\tilde{p}_h}{\partial\tilde{x}}\right|}. \tag{2.31}$$

The forced convection term due to the prescribed pressure gradient is estimated as

$$\frac{1}{\tilde{\rho}}\,\frac{\partial\tilde{p}_h}{\partial\tilde{x}} \sim \frac{\tilde{U}^2}{\tilde{x}}, \tag{2.32}$$

where $\tilde{U}$ is the velocity outside the BL. Similarly, the free convection term due to buoyancy is estimated as

$$\tilde{\alpha}\tilde{g}\,\frac{\partial}{\partial\tilde{x}}\int_{\tilde{z}}^{\infty}\tilde{T}'(\tilde{\lambda})\,\mathrm{d}\tilde{\lambda} \sim \tilde{\alpha}\tilde{g}\,\frac{(\tilde{T}_w - \tilde{T}_\infty)}{\sqrt{Re_{\tilde{x}}}}, \tag{2.33}$$

where the temperature at the wall $\tilde{T}_w = \tilde{T}_1$, the temperature at infinity $\tilde{T}_\infty = \tilde{T}_{mid}$.

The Reynolds number is given by

$$Re_{\tilde{x}} = \frac{\tilde{U}\tilde{x}}{\tilde{\nu}}. \tag{2.34}$$

A substitution of (2.32) and (2.33) into (2.31) and the introduction of the Grashof number

$$Gr_{\tilde{x}} = \frac{\tilde{\alpha}\tilde{g}(\tilde{T}_1 - \tilde{T}_{mid})\tilde{x}^3}{\tilde{\nu}^2} = \frac{\tilde{\alpha}\tilde{g}\,\Delta\tilde{T}\,\tilde{x}^3}{2\,\tilde{\nu}^2}, \tag{2.35}$$

result in

$$\varepsilon = \frac{Gr_{\tilde{x}}}{Re_{\tilde{x}}^{5/2}}\,. \tag{2.36}$$

For completeness, we list stream function $\tilde{\psi}$ and temperature $\tilde{T}$ which follow to

$$\tilde{\psi} = \tilde{\nu} B x^n \sum_{m=0}^{\infty} \varepsilon^m f_m, \tag{2.37}$$

$$\tilde{T} = \frac{\Delta\tilde{T}}{2} \sum_{m=0}^{\infty} \varepsilon^m \theta_m + \tilde{T}_{mid}. \tag{2.38}$$

Both series are substituted into (2.14)-(2.16). Some essential intermediate derivation steps are given in appendix A.1. Finally, the extended boundary layer model is obtained by grouping the terms with the same factors ε^m, $m = 0, 1, \ldots$ Here the series are truncated after the first-order term such that the functions f_0, f_1, θ_0, θ_1 are the unknowns, and $f = f_0 + \varepsilon f_1$ and $\theta = \theta_0 + \varepsilon\theta_1$. The perturbative parameter ε must be small enough to neglect the terms of a higher order. A way to estimate ε from our DNS data will be given in subsection 2.4.2. The obtained set of ordinary differential equations for the functions f_0, f_1, θ_0, θ_1 is given by

$$f_0''' + f_0'' f_0 + \frac{2n-1}{n}\left(1 - (f_0')^2\right) = 0, \tag{2.39}$$

$$\theta_0'' + Pr\, f_0 \theta_0' = 0, \tag{2.40}$$

$$f_1''' + f_0 f_1'' - \frac{1-n}{n} f_0' f_1' + \frac{3-4n}{n}\, f_0'' f_1 = -\frac{n-1}{n\sqrt{n}} \int_{\xi}^{\infty} \hat{\xi}\, \theta_0'\, \mathrm{d}\hat{\xi}, \tag{2.41}$$

$$\frac{n}{Pr}\,\theta_1'' + n f_0 \theta_1' - (3-5n) f_0' \theta_1 + (3-4n) f_1 \theta_0' = 0. \tag{2.42}$$

In agreement with the original RBC boundary conditions, we assume $\tilde{u} = \tilde{w} = 0$ and $\tilde{T} = \tilde{T}_1$ at the bottom plate with $\tilde{z} = 0$ and $\xi = 0$. Furthermore, we take $\tilde{u} \to \tilde{U}$ and $\tilde{T} \to \tilde{T}_{mid}$ well above the BL with $\tilde{z} \to \infty$ and thus $\xi \to \infty$. The

boundary conditions for (2.39)-(2.42) are as follows:

$$f_0(0) = 0, \qquad f_0'(0) = 0, \qquad f_0'(\infty) = 1; \tag{2.43}$$

$$\theta_0(0) = 1, \qquad \theta_0(\infty) = 0; \tag{2.44}$$

$$f_1(0) = 0, \qquad f_1'(0) = 0, \qquad f_1'(\infty) = 0; \tag{2.45}$$

$$\theta_1(0) = 0, \qquad \theta_1(\infty) = 0. \tag{2.46}$$

Equation (2.39) is the Falkner-Skan equation [21], and (2.40) the Pohlhausen equation [28]. Both are required for f_1 and θ_1 which is consistent with the idea of a series solution. Equations (2.39)-(2.42) are solved numerically. The numerical method is described in detail in appendix A.2.

2.4 Comparison of results of model and numerical simulations

2.4.1 Reduction of three-dimensional to planar fields

Three-dimensional time-dependent data are obtained from the DNS and have to be reduced to time-averaged two-dimensional ones for the extraction of velocity and temperature profiles (see, e.g. figure 2.2(a)). The starting point is a sequence of full snapshots. For each single snapshot, the angle of the LSC, ϕ_{LSC}, is determined as the direction of the mean horizontal velocity vector in the plane at $z = \delta_T$ (more details can be found in [13]). Here δ_T is the thermal boundary layer thickness which is given by

$$\delta_T = \frac{H}{2Nu}, \tag{2.47}$$

where Nu is the Nusselt number given by (1.20) or by (1.21). A typical snapshot of the horizontal vector field (u_ϕ, u_r) is shown together with the corresponding temperature field T in figure 2.3. The white line denotes the orientation of the mean horizontal velocity, i.e. the angle of the LSC close to the bottom plate. It should be noted that in the current work the way of determining the LSC angle via the vector field (u_ϕ, u_r) considered at the horizontal plane differs from the method applied in [12], [22], where the angle ϕ_{LSC} is determined by the distribution of the temperature on the vertical wall of the RBC cell, which was initially suggested in [29]. The first method, which we apply in our analysis, is based on the idea that the LSC (frequently called "wind of turbulence") is primarily related to motion of the fluid. Inasmuch as we use data obtained from the DNS, we have

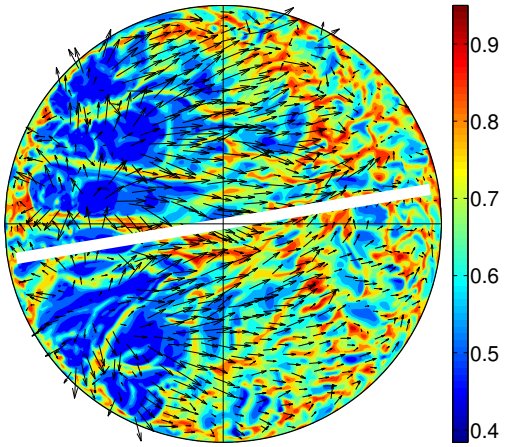

(a)

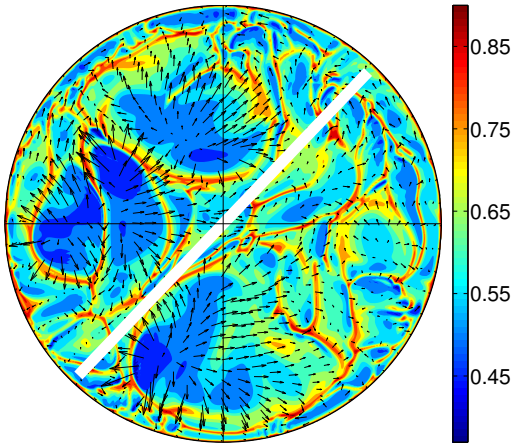

(b)

Figure 2.3: Two instantaneous plots of the temperature (T) and the velocity fields (u_ϕ, u_r) in the horizontal plane at $z = \delta_T$. (a) $Pr = 0.7$. (b) $Pr = 7$. We also indicate the orientation of the large-scale circulation, $\phi_{LSC}(t_0)$, for these snapshots by a white solid line.

the access to the velocity field (and the temperature field) in the whole domain of the cylindrical convection cell. To do the same in experimental setups is quite difficult, and the second method proposed in [29] is a good alternative.

After determining the angle of the LSC, the vertical projection plane is then oriented at the angle ϕ_{LSC}. The data reduction is sketched in figures 2.4(a) and 2.4(b). It is repeated for each snapshot thus giving a series of instantaneous two-dimensional fields u_χ, u_z, T which are averaged with respect to time and

result eventually in the time-averaged two-dimensional fields that are used in the analysis.

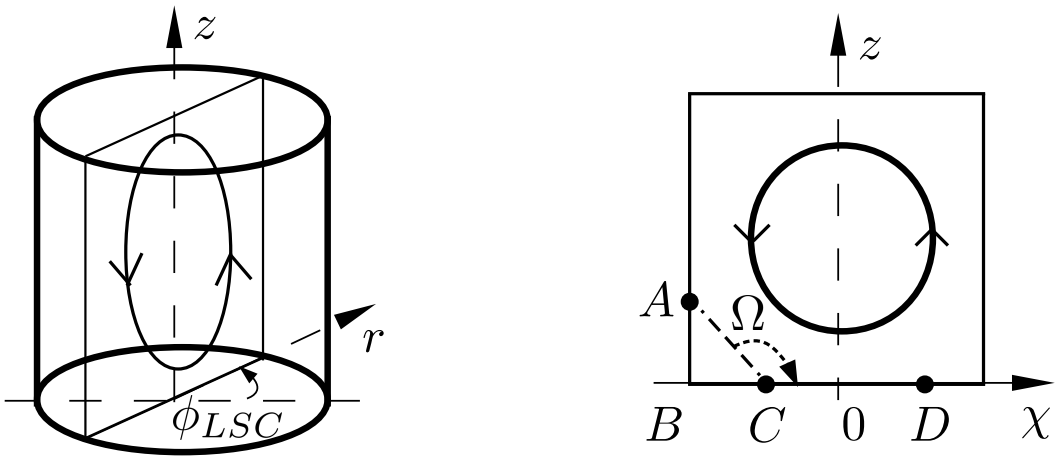

(a) (b)

Figure 2.4: Sketch of the reduction of the time-dependent three-dimensional data to two-dimensional planar data. (a) The convection cell and the vertical plane which is aligned with the angle ϕ_{LSC} are shown. (b) The LSC roll and the vertical plane are shown. Points A and C are locations where the time-averaged wall shear stress is equal to zero. B is the left bottom corner point. D is the point at which the influence of the right sidewall becomes significant. O is the center line point. The coordinates of C and D are given by $(\chi_C, 0)$ and $(\chi_D, 0)$, respectively. We denote $\overline{BA} = d_v$, $\overline{BC} = d_h$, and Ω is the angle formed by $\overline{CA}$ and $\overline{C0}$.

These time-averaged two-dimensional fields are used to determine the power k of the power law (2.24). The coefficient n is computed from equation (2.27) and the Prandtl number Pr is an input parameter. For the comparison of BL model results and data we will take the vertical profiles of the horizontal velocity component u_χ computed by (2.18) and (2.19) and the temperature T. In addition, the wall shear stress τ_w which is defined in (2.20) and (2.21) has to be computed on the basis of the time-averaged planar velocity field. The wall shear stress zero point C with the coordinates $(\chi_C, 0)$ (see also figures 2.2(a) and 2.4(b)) is taken as the leading edge of the BL. Point $D(\chi_d, 0)$ shown also in figure 2.4(b) denotes the location, where the influence of the opposite sidewall on the flow along the BL becomes significant. The determination of the location of point D is discussed further in subsection 2.4.3.

2.4.2 Conversion of profiles of extended boundary layer model

The solutions f_0, f_1 of the boundary value problem are used to construct the series solution of the horizontal component $\tilde{u}$ which follows by

$$\tilde{u}(x,\xi) = \tilde{U}_0 x^{2n-1}\,(f_0' + \varepsilon f_1'), \tag{2.48}$$

with $\tilde{U}_0$ given by (2.24). By fixing $x = x_0$, the profile $\tilde{u}(x_0,\xi) = \tilde{u}(\xi)$ is obtained from the BL model. The velocity field $u_\chi = u_\chi(\chi, z)$ is used for the extraction of a profile at fixed $\chi = \chi_0$, i.e. $u_\chi(\chi_0, z) = u_\chi(z)$. The coordinates between model and data are related by

$$x_0 = \chi_0 - \chi_C. \tag{2.49}$$

For choosing χ_0 we set the interval between points $C(\chi_C, 0)$ and $D(\chi_D, 0)$ shown in figure 2.4(b), i.e. $\chi_C < \chi_0 < \chi_D$. Before comparing the profiles $\tilde{u}(\xi)$ and $u_\chi(z)$, the former must be converted into the non-dimensional units by using the reference units of the DNS given in section 2.2. With equation (2.26) one obtains

$$z = \frac{\xi}{Bnx_0^{n-1}}\,. \tag{2.50}$$

The velocity $u = \tilde{u}/\tilde{U}_f$ is given by

$$u = \frac{\tilde{U}_0}{\tilde{U}_f}\,(\chi_0 - \chi_C)^{2n-1}\,(f_0' + \varepsilon f_1'). \tag{2.51}$$

The velocity amplitude $\tilde{U}_0/\tilde{U}_f$ can be rewritten with the help of Ra and Pr to

$$\frac{\tilde{U}_0}{\tilde{U}_f} = \frac{\tilde{H}\tilde{U}_0}{\tilde{\nu}}\sqrt{\frac{Pr}{Ra}}\,. \tag{2.52}$$

The coefficient B results with $\tilde{d} = \tilde{H}$ for $\Gamma = 1$ to

$$B = \sqrt{\frac{1}{n}}\sqrt[4]{\frac{Ra}{Pr}}\sqrt{\frac{\tilde{U}_0}{\tilde{U}_f}}. \tag{2.53}$$

The velocity $U = \tilde{U}/\tilde{U}_f$ can be taken directly from the time-averaged two-dimensional velocity field u_χ. In this work, we use the first local maximum of the velocity profile as the typical velocity outside the BL. If two profiles are extracted at different positions χ_i and χ_j within (χ_C, χ_D), their first maxima U_i and U_j will

differ. Consequently, the resulting amplitudes U_0 will differ, i.e.

$$U_{0,i} = \frac{U_i}{(\chi_i - \chi_C)^k} \neq \frac{U_j}{(\chi_j - \chi_C)^k} = U_{0,j}\,. \tag{2.54}$$

In order to obtain a unique value of U_0 we take an average of a series of profiles which are extracted at fixed $\chi_i \in (\chi_C, \chi_D)$, $i = 1, \ldots, N_{pr}$ with N_{pr} being the total number of the extracted profiles. For each profile, the amplitude $U_{0,i}$ is computed by using the formula included in (2.54):

$$U_{0,i} = \frac{U_i}{(\chi_i - \chi_C)^k}, \tag{2.55}$$

where U_i is the first local maximum of the current velocity profile extracted at χ_i. Averaging over all amplitudes results in the distribution

$$\langle U_{0,i} \rangle\, x^k = U_0\, x^k, \tag{2.56}$$

where $x = \chi - \chi_C$ according to (2.49).

The temperature obtained from the BL model is derived from equation (2.38) as

$$\tilde{T} = \frac{\Delta\tilde{T}}{2}\,(\theta_0 + \varepsilon\theta_1) + \tilde{T}_{mid}\,, \tag{2.57}$$

and with

$$T = \frac{\tilde{T} - \tilde{T}_2}{\Delta\tilde{T}}\,, \tag{2.58}$$

used in the DNS, the following dimensionless form is obtained:

$$T = \frac{1}{2}\,(\theta_0 + \varepsilon\theta_1) + \frac{1}{2}\,. \tag{2.59}$$

The transformation of ξ into z is performed in the same way as described at the beginning of this section.

The perturbation parameter ε (see equation (2.36)) can be rewritten in terms of the control parameters of RBC, Ra and Pr, as follows:

$$\varepsilon = \frac{1}{2}\sqrt[4]{\frac{Pr}{Ra}}\,\sqrt{\frac{x}{U^5}}\,, \tag{2.60}$$

where U is determined from the DNS data by using the above procedure.

2.4.3 Comparison of profiles for both Prandtl numbers

The DNS were conducted for the Prandtl numbers $Pr = 0.7$ and $Pr = 7$ by keeping the other control parameters unchanged. Each data set has a number of snapshots obtained from the simulations: the first set for $Pr = 0.7$ contains 850 snapshots which corresponds to a total simulation time $\Delta t_{850} \approx 42\ T_f$. For $Pr = 7$ we have 201 snapshots and $\Delta t_{201} \approx 200\ T_f$. Thus the time step between two snapshots is $0.05\,T_f$ for $Pr = 0.7$ and $1\,T_f$ for $Pr = 7$.

The time series of the angle $\phi_{LSC}(t)$ are shown in figure 2.5(a) for $Pr = 0.7$ and in figure 2.5(b) for $Pr = 7$. For each Prandtl number we determine ϕ_{LSC} at $z = \delta_T$ and at $z = H - \delta_T$. The phase shift of the data records supports the twisted structure of the LSC (see [2; 3] for further references). As a whole the LSC roll obeys a complex three-dimensional shape.

It is seen that the angle ϕ_{LSC} changes significantly with respect to time in both cases which confirms former results in [13]. Due to this reorientation, the number of snapshots for a time average is limited. The choice of the time window is determined by two points. On the one hand, the variation of ϕ_{LSC} should not be too large. On the other hand, the time window should be sufficiently long to obtain better statistics.

For the Prandtl number $Pr = 0.7$, the time window contains 25 samples, which corresponds to an averaging time $1.2\,T_f$. For this series, the angle ϕ_{LSC} does not change significantly. The values of the exponent k obtained from the time-averaged planar fields are $k \approx 0.27$ and $k \approx 0.45$, and the corresponding coefficients $\beta = 2k/(k+1)$ are $\beta \approx 0.43$ and $\beta \approx 0.62$, respectively. The two sets (k, β) result from two zeros of the time-averaged wall shear stress at the side wall. It has been discussed for example in [30] that the wall shear stress field will have several zero points. For $Pr = 7$, we took a series of 29 snapshots. The exponent $k \approx 0.54$ corresponds to the coefficient $\beta \approx 0.70$.

In order to choose one of the two values of k (and thus of β) for $Pr = 0.7$, the following procedure is performed. First, the location of point D, which is introduced at the end of subsection 2.4.1 and shown in figure 2.4(b), is determined for each distribution $U_0\,(\chi - \chi_C)^k$ obtained for the two values of k by comparing these distributions with the distribuation of the velocity $U(\chi)$ taken outside the BL at the point of the first local maximum of the velocity profile. Note that values of $U(\chi)$ are used for computing U_0 by using (2.55), where $U_i = U(\chi_i)$. The comparison is done by computing the relative difference δr which is given by

$$\delta r = \frac{||f - g||}{||f||}\,. \tag{2.61}$$

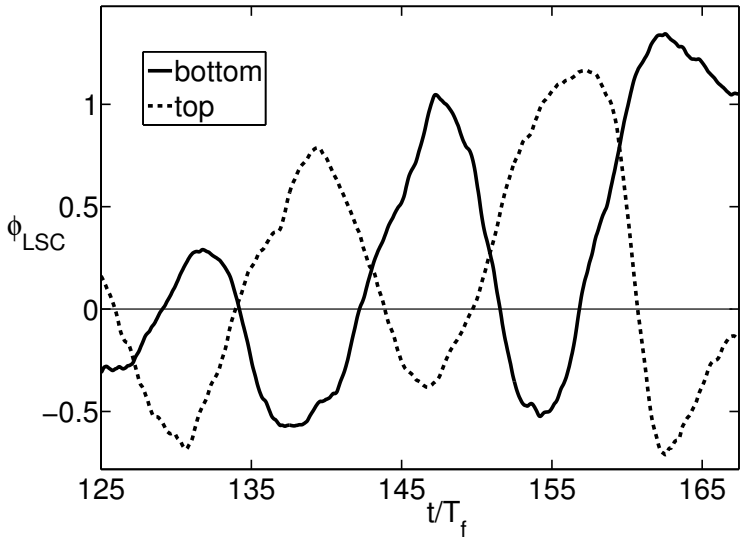

(a)

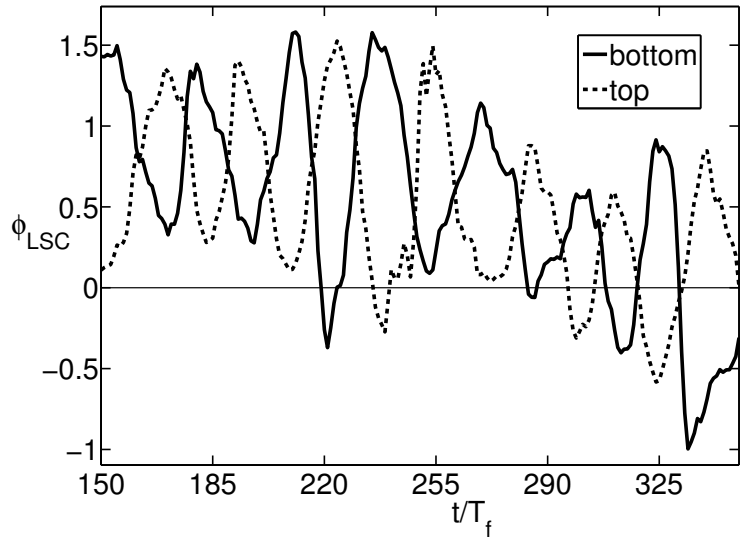

(b)

Figure 2.5: Time series of the angle of the LSC (in radians) computed based on the mean horizontal velocity at $z = \delta_T$ (*bottom*) and $z = H - \delta_T$ (*top*) where δ_T is the thermal BL thickness. (a) data for $Pr = 0.7$. (b) data for $Pr = 7$. The variations of the angle are about the same for both Prandtl numbers when the time interval is of the same size.

Here f and g are the functions to be compared. The norm is computed in two different ways, either as a supremum norm or as an L_2 norm. Thus, the location of point D (for each distribution $U_0\,(\chi - \chi_C)^k$) is determined, when the minimum of δr is found. Finally, having found the coordinate of point D, χ_D, for each distribution $U_0\,(\chi - \chi_C)^k$, the proper value of k corresponds to the distribution

$U_0\,(\chi - \chi_C)^k$ which has the minimum value of δr obtained while searching the "best" location of point D. The value $k \approx 0.27$ appeared to be the optimal choice. The resulting profiles of $U = U(\chi)$ and the computed fits $U_0\,x^k$ with $x = \chi - \chi_C$ are shown in figure 2.6(a) for $Pr = 0.7$ and figure 2.6(b) for $Pr = 7$.

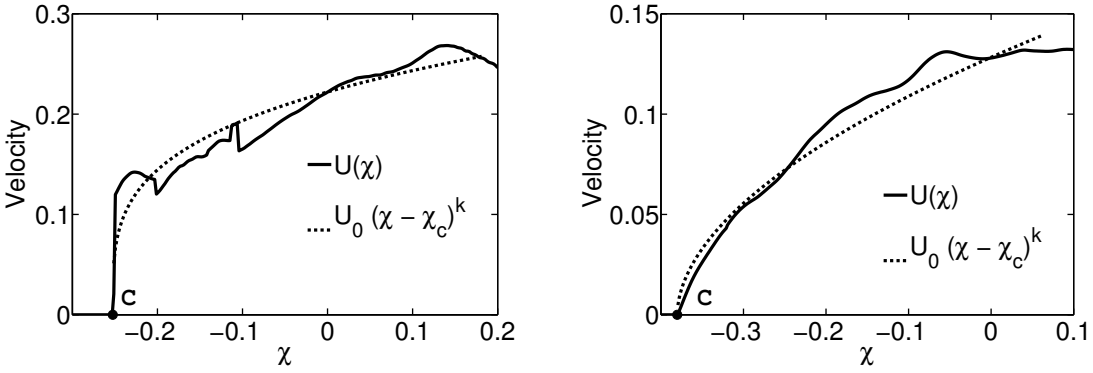

Figure 2.6: The distribution of the velocity $U = U(\chi)$ which is obtained as the first local maximum of profiles extracted from the time-averaged planar fields of u_χ together with the fit $U_0\,(\chi - \chi_C)^k$. (a) data for $Pr = 0.7$ with $k \approx 0.27$. (b) data for $Pr = 7$ with $k \approx 0.54$.

Before we proceed to the comparison with DNS data, the dependence of the extended boundary layer model on k and Pr is discussed briefly. First, we show the effect of k on the first-order correction terms f_1, θ_1 for $Pr = 0.7$, the case for which we determined two sets (k, β). The power k is connected with the absolute value of the longitudinal pressure gradient so that $|\partial\tilde{p}/\partial\tilde{x}|$ increases as k grows. The plots of f_0, f_1, θ_0, θ_1 are shown in figure 2.7. It is seen that the magnitude of the first-order terms f_1, θ_1, and thus the buoyancy effect, decreases for growing k.

Secondly, we show the influence of the Prandtl number on f_1 and θ_1. The power k is fixed in this comparison to $k \approx 0.27$ ($\beta \approx 0.43$). The functions f_0, f_1, θ_0, θ_1 are shown in figure 2.8. The figure reveals that the contribution of the first-order correction terms decreases again as the Prandtl number increases.

Figure 2.9 displays the comparison of the profiles obtained from the DNS and the extended BL model (EBLM). We also list the Blasius and Pohlhausen solutions for $\beta = 0$ and ε=0 as well as the Falkner-Skan solution for $\varepsilon = 0$. The error bars of all relevant parameters were again estimated by evaluating the results over the first and second halves of the corresponding data records and subsequently taking the difference of both results. Table 2.2 summarizes all parameters which are necessary for our comparison of the model with the DNS data.

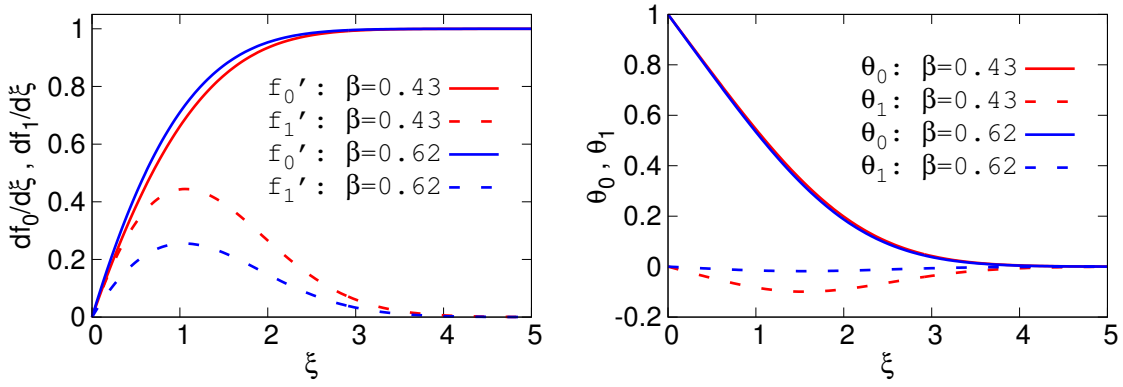

(a) (b)

Figure 2.7: The numerical solutions obtained from the extended BL model for $\beta \approx 0.43$ ($k \approx 0.27$) and $\beta \approx 0.62$ ($k \approx 0.45$), at fixed $Pr = 0.7$: (a) f_0' and f_1'; (b) θ_0 and θ_1.

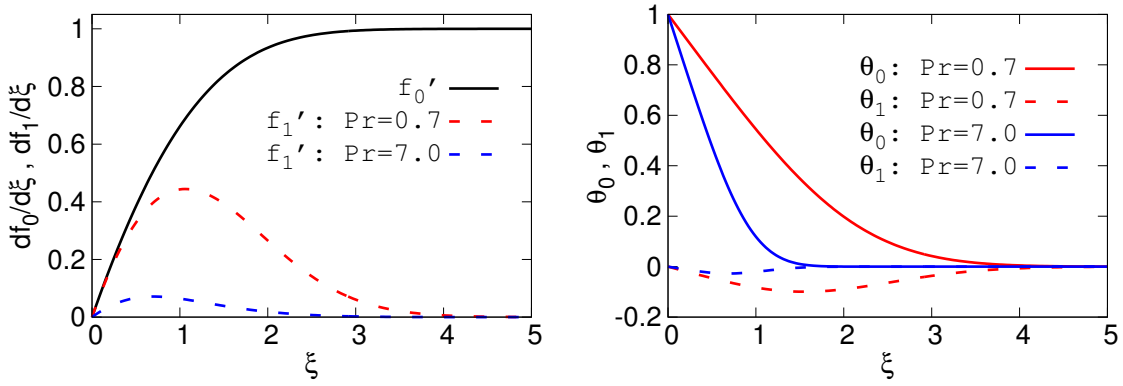

(a) (b)

Figure 2.8: The numerical solutions obtained from the extended BL model for $Pr = 0.7$ and $Pr = 7$ at fixed $\beta \approx 0.43$ ($k \approx 0.27$): (a) f_0' and f_1'; (b) θ_0 and θ_1.

In figure 2.9, we show fits for the two values of ε which follow from (2.60). These are $\varepsilon \approx 0.04$ for $Pr = 0.7$ and for $\varepsilon \approx 0.36$ for $Pr = 7$. In addition, we show profiles of the EBLM with larger values of ε in order to demonstrate how sensitive the expansion is with respect to the buoyancy corrections.

It can be seen that the extended boundary layer model allows to improve the agreement between the model solutions and the DNS data for $Pr = 0.7$ as the contribution of buoyancy increases. The agreement becomes very good for the velocity profiles (see $\varepsilon = 0.3$) while the improvements remain smaller in the case of the temperature field. The situation is different for the larger Prandtl number. The BL model works better than the classical Blasius-Pohlhausen case, but it is nearly insensitive to the additional buoyancy corrections.

In order to understand better the reasons for the observed insensitivity at

Table 2.2: Parameters for the comparison between simulation data and BL model. For $Pr = 0.7$ we list the set of parameters only which is eventually used for the comparison. $\chi_0 = 0.0$ for the analysis. The large uncertainty in χ_D at $Pr = 7$ is a result of the weaker LSC.

Pr	k	β	Ω	χ_C	χ_D
0.7	0.27 ± 0.02	0.43 ± 0.03	2.5 ± 0.1	-0.25 ± 0.01	0.18 ± 0.05
7	0.54 ± 0.04	0.70 ± 0.03	2.0 ± 0.1	-0.38 ± 0.04	0.06 ± 0.29

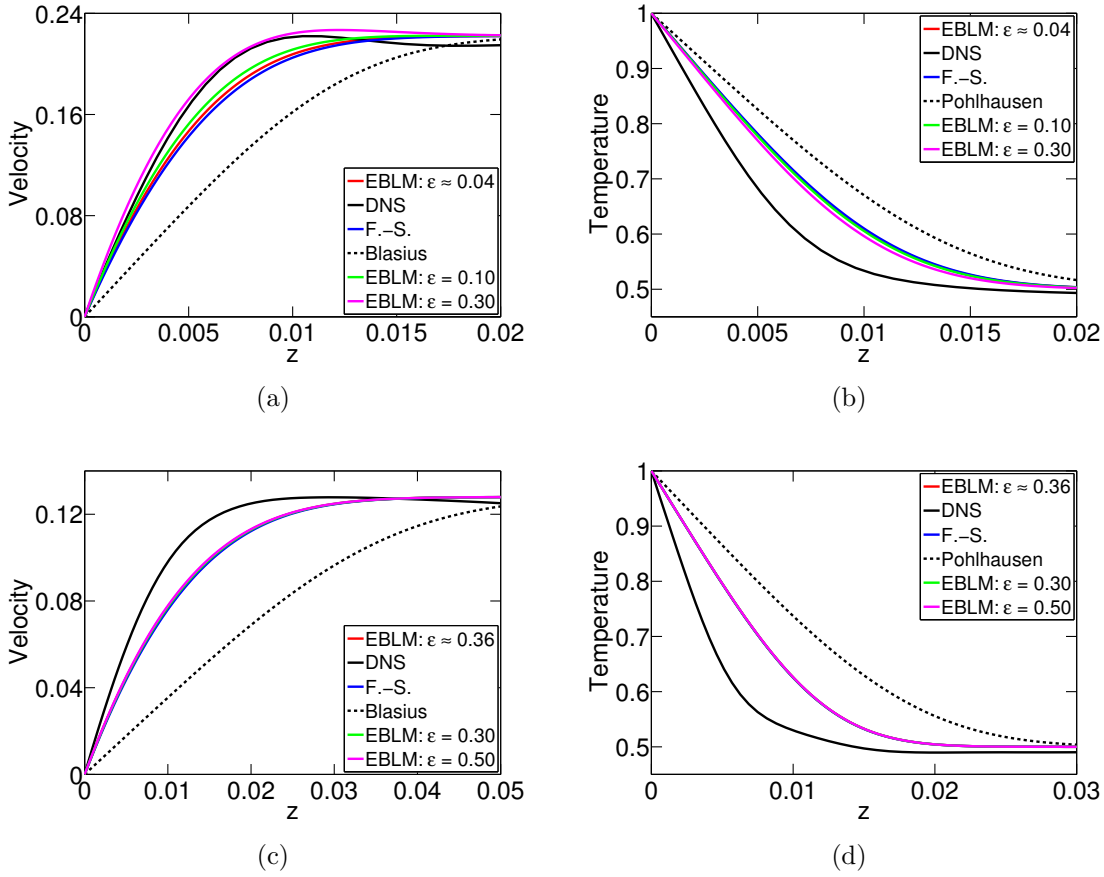

Figure 2.9: Comparison of the DNS profiles at $\chi_0 = 0.0$ with the ones obtained from the extended BL model (EBLM). The profiles of EBLM are constructed by using the perturbation parameter ε computed by (2.60) and other values. The Falkner-Skan case corresponds to $\varepsilon = 0$. The Blasius and Pohlhausen cases correspond to $\varepsilon = 0$ and $\beta = 0$. (a) and (b) are for $Pr = 0.7$ with $k \approx 0.27$ ($\beta \approx 0.43$) and $\chi_C \approx -0.25$. (c) and (d) are for $Pr = 7$ with $k \approx 0.54$ ($\beta \approx 0.70$) and $\chi_C \approx -0.38$. (a) and (c) compare the velocities u_χ and u. (b) and (d) compare the corresponding temperature profiles.

$Pr = 7$, we go back to figure 2.3 where two typical horizontal slice cuts at $Pr = 0.7$ (2.3(a)) and $Pr = 7$ (2.3(b)) are displayed. Both plots show the temperature

contours together with the instantaneous horizontal velocity field close to the bottom plate. We observe that the fluid motion for the lower Pr is much more coherent. The orientation of the LSC, which is indicated by the solid line, coincides well with the orientation of the majority of the velocity vectors. The situation is different for the larger Prandtl number where the direction of the velocity vectors is varying strongly across the plane and the LSC orientation is much less representative. Amplitude and coherence of the LSC decrease as the Prandtl number grows. In order to demonstrate this decrease of the LSC amplitude, we plot in figure 2.10 time series of the root mean square velocity. It is defined by

$$U_{RMS}(t) = \sqrt{\langle u_\phi^2 \rangle_V + \langle u_r^2 \rangle_V + \langle u_z^2 \rangle_V}\,, \tag{2.62}$$

calculated for each snapshot as a volume average in the whole three-dimensional cell. The reduced value for the larger Prandtl number is clearly visible.

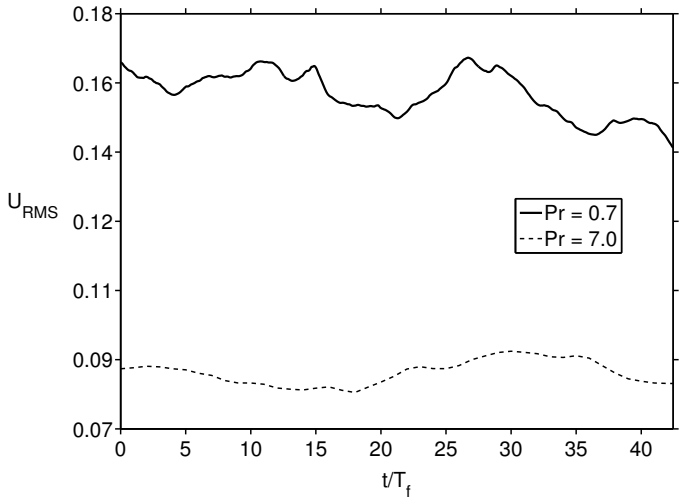

Figure 2.10: The time series of the root mean square of the velocity for both Prandtl numbers.

2.5 Conclusions

We compared the boundary layers of velocity and temperature, which have been obtained from direct numerical simulations of turbulent convection in a closed cylindrical cell, with a boundary layer model that combines the effects of a prescribed horizontal pressure gradient and buoyancy. We used two data records for this comparison, Rayleigh-Bénard convection at Prandtl numbers $Pr = 0.7$ and $Pr = 7$, respectively. Both records were obtained for a Rayleigh number

$Ra = 3 \times 10^9$ and an aspect ratio $\Gamma = 1$. In order to perform such comparison, the original three-dimensional and time-dependent simulation data were reduced to two-dimensional and time-averaged fields in a vertical plane which crosses the center line of the cell. This plane is aligned with the instantaneous orientation angle of the large-scale circulation flow for each snapshot.

The comparison of the mean boundary layer profiles shows that our extended model can improve the matching of the simulation profiles and model solutions. This holds particularly for the smaller Prandtl number. In the case of the larger Prandtl number the improvements remain negligible. This can be explained from the decrease of the thermal boundary layer thickness. In turn, the effects of pressure gradient seem to dominate increasingly the dynamics as Pr grows. Note that the value of β is larger. This holds albeit the amplitude and coherence of the large-scale circulation flow is found to decrease for the larger Prandtl number case.

Our study shows thus that the magnitude of the buoyancy impact relative to driving by the pressure gradient becomes weaker. However, pressure gradients in the boundary layer seem to be generated by local downwellings of cold fluid to the bottom plate rather than by a coherent LSC which fills the whole cell. These circumstances might explain the observed insensitivity of the BL model which builds on a reduction of the dynamics on a plane. Other BL models, which have been discussed for example in [19], start with the free convection case. As a result of this discussion, a perturbative expansion that starts from the free convection case might be the preferable way for the large Prandtl number limit of turbulent convection.

On the one hand, it is expected that the fluctuations in the BL will grow and that the LSC will become weaker when the Rayleigh number is increased at a given Prandtl number. On the other hand, we see for example in figure 1 of ref. [13] that the boundary layer flow can be divided into an plume impact region, a shear flow region and a plume ejection region, at least for cells with aspect ratio one. Such clear separation is observed for sufficiently large flow Reynolds numbers only. This in turn could improve the matching to BL models, in particular in the shear region. This could hold even for larger Ra.

Meanwhile, the boundary layer model can be extended by including more terms of higher orders of the series, which would make the mathematical manipulations more complex. Given our results, this improvement seems not reasonable, particularly for the larger Prandtl numbers. A further refinement of the analysis can be achieved by splitting the boundary layer dynamics into periods with a

strong plume detachment and periods of re-laminarization as discussed in [13]. Our results suggest also that lower Prandtl numbers could be better represented by the present extended BL model. Since simulations at lower Prandtl numbers are much more demanding in terms of the grid resolution, we have to postpone this point into the future. We saw that the temperature profile deviations between data and model are the most persistent ones. A different and promising extension of the boundary layer model was suggested very recently in [31]. This model improved predictions for the temperature profiles by an inclusion of fluctuations and worked particularly well for larger Prandtl numbers. So far this approach relies on a prescribed velocity profile. An extension to a joint velocity-temperature model could be a further interesting aspect of future work.

Chapter 3

Numerical method for turbulent convection in extended rectangular boxes

3.1 Introduction

As it is stated in section 1.2, the convection flow is typically studied both numerically and experimentally using containers of the simple geometries such as cells of cylindrical shape or containers of rectangular cross section (a long list of works can be found in reviews [2; 3]). Both types of samples have advantages and disadvantages and are applied depending on a problem to be investigated. A notable feature of a cylindrical cell is its natural symmetry in the azimuthal direction which makes the flow simpler to some extent and means the following: in the simplest case of a cylindrical cell of the aspect ratio one, when one large-scale circulation roll is established (see e.g. [27] or [32]), this convection roll is not restricted in its azimuthal rotation and can be oriented at any angle (if the cell is not tilted or locally deformed).

In the case of a rectangular box, there is no such symmetry, and the LSC roll can be oriented along some preferable direction. For example, [33] and [34] report that in a cubic cell the main circulation is oriented along one of the diagonals of a horizontal plate, and it remains in this fixed position for a long time. Moreover, it is shown in [35] that the structure of the mean flow in cubic containers is rather complicated: in addition to secondary flows located near opposite corners, which take place also in cylindrical cells of the aspect ratio one (see e.g. [22]), there is a flow of the opposite direction (with respect to the main flow) which is located near another corner and breaks the symmetry about the LSC flow. On the one hand,

the fixed position of the mean flow in cubic cells can be useful for accumulating statistical data during a long-term period of time. On the other hand, it is not clear how such a complicated flow influences obtained small-scale statistical results. To make the flow more symmetrical and fixed in one direction, a rectangular box with different Γ_x and Γ_y given by (1.19) is used (see e.g. [36; 37]). Nevertheless, such samples are hardly applicable to reproduce phenomena occurring in natural convection systems due to the artificial preferable direction, and the emphasis of the present work is on rectangular boxes which have the same length along both horizontal directions.

All the information about convection cells given above in this section is related to closed samples of the aspect ratio one, but even in this simplest case it becomes obvious that behaviour of a flow depends on the shape of a container. Moreover, the fact that properties of a turbulent flow depend on a geometry of a convection cell was directly confirmed in [38], where it is reported on a significant difference in fluctuations measured in the interior of a $\Gamma = 1$ cylindrical cell and of a cubic container. In [39] it was also showed that structures of the temperature field obtained in a $\Gamma = 1$ cylindrical cell differ from those obtained in a cubic sample. Both experimental works described in [38] and [39] were done with using containers of $\Gamma = 1$ at moderate Rayleigh numbers (up to $Ra \sim 10^{10}$). In this regard the following question arises: what will happen with characteristics of a turbulent convection flow in a convection cell of larger Γ and at higher Ra? The question becomes more interesting, if one recalls that convection flows in nature occur at very high Rayleigh numbers and at large horizontal scales. Some examples of natural convection systems and their parameters can be found in [2]. But the achievement of higher Ra and larger Γ simultaneously becomes a challenging problem in conducting experiments. Once some Rayleigh number is achieved, it can further be increased either by changing the parameters of the fluid or by increasing the height of the cell, which in turn means a decrease in the aspect ratio of the cell. To keep Γ fixed, one needs to extend the cell in the horizontal direction as well, and the relative extension is much greater than that in the vertical direction (it is multiplied by Γ). From a computational point of view, achieving larger values of Ra and Γ requires higher grid resolution for large computational domains and involves greater computational costs. The computational costs rise with Γ^2 at a fixed Ra.

Another interesting question related to laterally extended convection cells is that it is still not clear how lateral constraints influence properties of convection flows. For example, in [12] it is reported about an increase in the heat flux in

the vicinity of the sidewall of a cylindrical cell of $\Gamma = 1$. Meanwhile, there is an assumption that sidewalls effects become negligible in samples of $\Gamma \gg 1$, but it has not been yet studied thoroughly. Experimentally it is difficult to do, because almost all experiments are done with using a fluid confined between rigid walls to control the temperature at the walls with high accuracy and to reproduce the flow at the same conditions. In this case, carefully performed numerical simulations can facilitate and shed new light on the problem, at least in the frame of the simplified model of an incompressible flow derived by applying the Oberbeck-Boussinesq approximation.

Despite the difficulties related to samples extended laterally, some steps in the direction towards higher Γ (but still moderate Ra) were done by conducting both numerical (see e.g. [27; 40] or recent work [41]) and experimental (see e.g. [42; 43]) studies. Particularly, at the Institute of Thermodynamics and Fluid Mechanics of Technische Universität Ilmenau laboratory experiments with air ($Pr \approx 0.7$) at $Ra = 2.0 \times 10^4 \ldots 5.5 \times 10^5$ are being conducted in a sample of rectangular cross section of the aspect ratio $\Gamma = 10$. It was noted that in such samples of larger aspect ratios structures of convection flows are much more complicated due to the presence of multiple LSC rolls (see examples of patterns in [27; 40]). Nevertheless, there are not so much works in comparison with those devoted to convection cells of lower aspect ratios.

Thus, the goal of the present work is to perform direct numerical simulations of turbulent convection flows at high Rayleigh numbers and in closed rectangular boxes with large aspect ratios. In the frame of the present work, the corresponding code for performing three-dimensional DNS of a turbulent convection flow in a rectangular box was developed. The base of the code for convection problems is the program which is described in [44] and which was initially developed for performing three-dimensional DNS of electrically conducting incompressible fluids in ducts (and channels) to study phenomena related to magnetohydrodynamics. The code for duct flows is based on the finite difference method and requires relatively lower computational costs in comparison with other techniques applied for numerical simulations of incompressible flows confined by rigid walls, which is beneficial to numerical studies of problems in convection cells of large aspect ratios. The geometry of a duct shown in figure 3.1 is similar to a rectangular box shown in figure 1.1(b), and the governing equations of duct flows and convection flows in cells are almost the same, as it is demonstrated below in section 3.5. By taking into account both factors, one can assume that possible changes of the initial code for adapting it to perform DNS of convection flows in rectangular cells

are minimum.

In section 3.5 the applied numerical method for solving the governing equations given by (1.11)-(1.13) is provided. Having obtained the new code for DNS of turbulent convection flows in closed extended rectangular boxes, which have rigid walls at all boundaries, one problem related to the ergodic theory was solved, and it is discussed below in chapter 4.

Before going into details on the applied method, it should be noted that the presence of rigid walls of a box imposes some limitations on choice of available numerical approaches. The natural symmetry of the cylindrical geometry explained above in this section allows to apply a family of numerical methods for accelerating computations significantly (see e.g. [13]). In the absence of rigid sidewalls, a similar approach applied for a cylindrical cell can be applied also for a rectangular domain (see e.g. [40]). Nevertheless, such approaches are not applicable for problems when a flow is studied in a closed rectangular cell, or their application involves extra overheads and computational costs.

3.2 Numerical scheme

As already said at the end of section 3.1, the new code for RBC in a rectangular box is based on the one which is described in [44] and which is applied for performing three-dimensional numerical simulations of electrically conducting incompressible flows in ducts. A typical geometry of a duct is shown in figure 3.1, where the x direction of the Cartesian coordinate system is a streamwise direction, the z axis is opposite and parallel to the vector of acceleration due to gravity $\boldsymbol{g}$, all the horizontal and vertical sides (parallel to the streamwise direction) are rigid walls which confine the flow. In the mathematical model of a duct flow described in [44] a periodic boundary condition is applied along the x direction: if L_x is some periodicity length, then the velocity $\boldsymbol{u}(x + L_x, y, z) = \boldsymbol{u}(x, y, z)$, and the computational domain is restricted along x by the length L_x.

The corresponding system of governing equations written in non-dimensional units and applied for performing direct-numerical simulations of incompressible duct flows include the continuity equation written in the differential form as

$$\nabla \cdot \boldsymbol{u} = 0, \tag{3.1}$$

where the velocity $\boldsymbol{u}$ have the three components u_x, u_y, u_z in the Cartesian

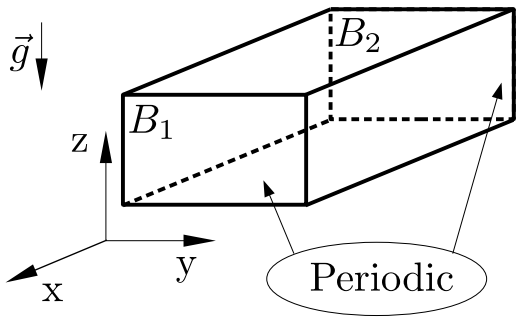

Figure 3.1: The sketch of a duct with the marked periodic boundary conditions B_1 and B_2 which are perpendicular to the streamwise direction x.

coordinate system shown in figure 3.1, and the momentum equation

$$\frac{\partial \boldsymbol{u}}{\partial t} + (\boldsymbol{u} \cdot \nabla)\, \boldsymbol{u} = -\nabla p + \frac{1}{Re}\, \nabla^2\, \boldsymbol{u}, \tag{3.2}$$

where the Reynolds number Re is defined as

$$Re = \frac{\tilde{U}\, \tilde{L}}{\tilde{\nu}}, \tag{3.3}$$

$\tilde{U}$ is the mean streamwise velocity, $\tilde{L}$ some characteristic size of the duct, $\tilde{\nu}$ the kinematic viscosity (see [44]). Equation (3.2) is written without the Lorentz force induced by the moving conducting fluid in the presence of a magnetic field, because such problems are not considered in the current work, and all terms and equations related to electromagnetic effects are dropped out without loss of generality. The continuity equation given by (3.1) or by (1.11) remains the same, while the momentum equation given by (3.2) can be easily converted into equation (1.11) by including the buoyancy force and by choosing proper reference values (see below in section 3.5). To solve equations (3.1) and (3.2) numerically, the standard no-slip condition for the velocity at the rigid walls of a duct is imposed, i.e. $\boldsymbol{u} = 0$ at the walls. The rest two boundaries of the duct, which are perpendicular to the streamwise direction x and denoted in figure 3.1 by B_1 and B_2, are periodic, as it is stated above.

The numerical model applied for solving (3.1) and (3.2) is based on scheme B introduced in [44] and originally devised in [45]. The scheme is highly conservative with respect to the mass and momentum (and electric charge) balance, while the conservation of kinetic energy is fulfilled up to the dissipative error of the third order. The discretization in time is done by using the second order explicit Adams-Bashforth/backward differentiation method. To advance in time from the

current step $t^{(n)}$ to the next step $t^{(n+1)}$, the following procedure is performed ($t^{(n-1)}$ is the previous step, Δt is a fixed time step, $\Delta t = t^{(n+1)} - t^{(n)} = t^{(n)} - t^{(n-1)}$).

1. The right-hand side vector $\boldsymbol{F}^{(n)}$ of the current step is computed as

$$\boldsymbol{F}^{(n)} = -(\boldsymbol{u}^{(n)} \cdot \nabla)\, \boldsymbol{u}^{(n)} + \frac{1}{Re} \nabla^2 \boldsymbol{u}^{(n)}. \tag{3.4}$$

   The the right-hand side vector $\boldsymbol{F}^{(n-1)}$ of the previous step is computed similarly by using the velocity field $\boldsymbol{u}^{(n-1)}$ obtained on $t^{(n-1)}$.

2. Having computed $\boldsymbol{F}^{(n)}$ and $\boldsymbol{F}^{(n-1)}$, the integration over time to obtain the intermediate velocity $\boldsymbol{u}^{(*)}$ is done as follows:

$$\frac{3\,\boldsymbol{u}^{(*)} - 4\,\boldsymbol{u}^{(n)} + \boldsymbol{u}^{(n-1)}}{2\,\Delta t} = 2\,\boldsymbol{F}^{(n)} - \boldsymbol{F}^{(n-1)}. \tag{3.5}$$

3. After the velocity $\boldsymbol{u}^{(*)}$ has been obtained, the pressure $p^{(n+1)}$ on the next step is computed by solving the equation

$$\nabla^2 p^{(n+1)} = \frac{3}{2\,\Delta t} \nabla \cdot \boldsymbol{u}^{(*)}. \tag{3.6}$$

4. The velocity $\boldsymbol{u}^{(n+1)}$ on the next step is obtained by correcting the intermediate velocity $\boldsymbol{u}^{(*)}$ as follows:

$$\boldsymbol{u}^{(n+1)} = \boldsymbol{u}^{(*)} - \frac{2}{3}\,\Delta t\, \nabla p^{(n+1)}. \tag{3.7}$$

Equation (3.6) is the well-known Poisson equation discussed in more detail in section 3.3. The boundary conditions needed for solving equation (3.6) are obtained immediately by applying the no-slip condition for the velocity $\boldsymbol{u}^{(n+1)}$ and by multiplying both sides of (3.7) by the unit vector $\boldsymbol{n}$ normal to a corresponding wall:

$$\boldsymbol{u}^{(n+1)} \cdot \boldsymbol{n} = 0 = \boldsymbol{u}^{*} \cdot \boldsymbol{n} - \frac{2}{3}\,\Delta t\, \frac{\partial p^{(n+1)}}{\partial \boldsymbol{n}}, \tag{3.8}$$

where the directional derivative $\partial p^{(n+1)}/\partial \boldsymbol{n} = \nabla p^{(n+1)} \cdot \boldsymbol{n}$ is introduced (see e.g. [46]). The obtained condition given by (3.8) is referred to as the Neumann boundary condition discussed below in section 3.3. In the case of a duct, there are four rigid walls, and the rest two boundaries (B_1 and B_2 in figure 3.1) are periodic and incorporated in the solution method of equation (3.6), which is explained below in section 3.4.1. As for a closed rectangular box, all the six boundaries are walls, and the condition given by (3.8) is set at all the boundaries. It should

be noted that the above procedure is performed by using data obtained on the two previous steps, $t^{(n)}$ and $t^{(n-1)}$. If numerical simulations are started from the very beginning, when only initial fields of parameters are given, step 2 for the time integration is done by applying the forward Euler method of the first order instead of (3.5), which is applied further for integrating over time.

For the space discretization a regular collocated grid shown in figure 3.2 is introduced to divide the computational domain into rectangular cells. The fields of $\boldsymbol{u}$ and p (and some other parameters) are computed at nodes of the grid. In the case of a duct, the grid is uniform along the streamwise direction x, while it is non-uniform in the y and z directions and is getting denser close to the walls to resolve properly boundary layers. In the case of a closed rectangular box, there is no streamwise direction, periodic boundary conditions cannot be imposed due to rigid walls, and the grid is non-uniform for reasons related to resolution of boundary layers at the walls, as it is discussed below in section 3.4.1. The Laplacian and the gradient operator included in (3.4), (3.6), (3.7) are approximated by applying the central difference scheme on the collocated grid. To apply the central difference formula at all nodes of the domain including boundaries, a layer of ghost nodes is added to each boundary of the rectangular domain (unknown values at ghost nodes are extrapolated by using the Lagrange interpolating polynomial based on four interior points). In addition to the collocated grid, an auxiliary staggered grid shown in figure 3.2 is introduced at the centers of edges of cells formed by nodes of the collocated grid. This new grid is used for velocity fluxes which are computed initially by interpolating the intermediate velocity field $\boldsymbol{u}^{(*)}$ (obtained from equation (3.5) at nodes of the collocated grid) and are corrected after solving equation (3.6). Velocity fluxes are applied for the discretization of the non-linear term of the momentum equation given by (3.2) on the next step $t^{(n+1)}$ and for the assessment of the incompressibility of the flow given by (3.1) and approximated at a node (x_i, y_j, z_k) of the collocated grid as

$$\nabla \cdot \boldsymbol{u} \approx \frac{f_{x,i+1/2} - f_{x,i-1/2}}{x_{i+1/2} - x_{i-1/2}} + \frac{f_{y,j+1/2} - f_{y,j-1/2}}{y_{j+1/2} - y_{j-1/2}} + \frac{f_{z,k+1/2} - f_{z,k-1/2}}{z_{k+1/2} - z_{k-1/2}}, \qquad (3.9)$$

where $f_{x,*}$, $f_{y,*}$, $f_{z,*}$ are the components of the flux in the Cartesian coordinate system given at nodes of the staggered grid with corresponding coordinates $(x_{i\pm1/2}, y_j, z_k)$, $(x_i, y_{j\pm1/2}, z_k)$, $(x_i, y_j, z_{k\pm1/2})$, which can be seen in figure 3.2 for the two-dimensional case. Approximate values of $\operatorname{div} \boldsymbol{u} = \nabla \cdot \boldsymbol{u}$ computed by (3.9) depend on the accuracy of the solution of equation (3.6). More information on the time and space discretization as well as the computation of velocity fluxes can

be found in [44].

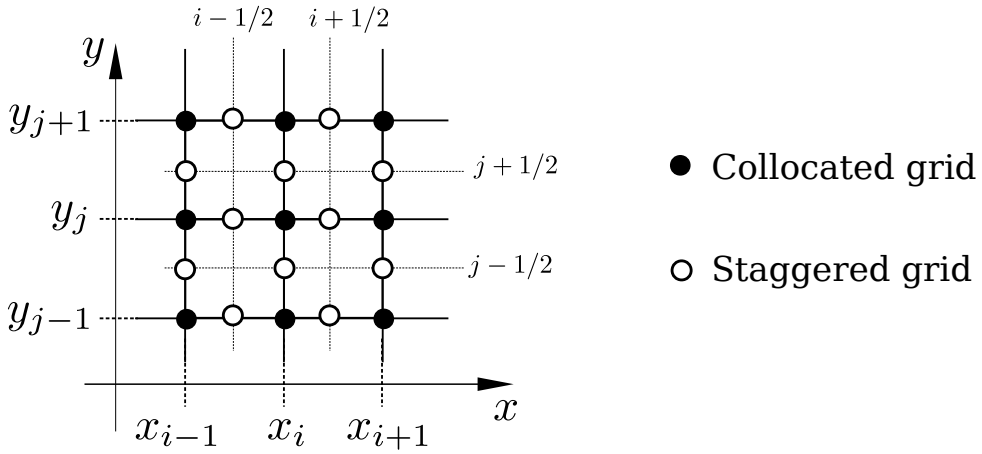

Figure 3.2: The sketch of the collocated and staggered grids for two-dimensional case. The auxiliary intermediate horizontal and vertical lines labeled by $i \pm 1/2$ and $j \pm 1/2$ pass through nodes of the staggered grid. Coordinates of nodes of the staggered grid are located at the centers between corresponding coordinates of the collocated grid. Coordinates of nodes of the staggered grid along the z direction are found similarly.

To solve problems related to convection flows (see e.g. [47]), the code introduced in [44] was extended by including the buoyancy force which is given in dimensionless units by

$$\boldsymbol{F}_B = T\,\boldsymbol{e}_z, \tag{3.10}$$

where the vector $\boldsymbol{e}_z$ is the unity vector in the z direction. The buoyancy term given by (3.10) is added to the right-hand side of the momentum equation given by (3.2):

$$\frac{\partial \boldsymbol{u}}{\partial t} + (\boldsymbol{u}\cdot\nabla)\,\boldsymbol{u} = -\nabla p + \frac{1}{Re}\,\nabla^2\,\boldsymbol{u} + T\,\boldsymbol{e}_z \tag{3.11}$$

To close the system which consists of the continuity equation given by (3.1) and the momentum equation given by (3.11), the energy equation has to be solved:

$$\frac{\partial T}{\partial t} + (\boldsymbol{u}\cdot\nabla)\,T = \frac{1}{Pe}\,\nabla^2 T, \tag{3.12}$$

where the Peclet number Pe is defined as

$$Pe = \frac{\tilde{U}\tilde{L}}{\tilde{\kappa}}. \tag{3.13}$$

Boundary conditions required for solving (3.12) depend on a problem, and in the case of RBC in a closed cell, they are given by (1.15). Moreover, the

Reynolds number Re defined by (3.3) and the Peclet number Pe defined by (3.13) are written in terms of the reference units given by (1.6) (see section 3.5).

When convection is taken into account, the time discretization of the momentum equation is also changed by adding the buoyancy term defined by equation (3.10) to the right-hand side vectors $\boldsymbol{F}^{(n)}$ and $\boldsymbol{F}^{(n-1)}$ computed by (3.4). Equation (3.12) is dicretized in time in a similar way as the momentum equation according to (3.5):

$$\frac{3\,T^{(n+1)} - 4\,T^{(n)} + T^{(n-1)}}{2\,\Delta t} = 2\,N^{(n)} - N^{(n-1)} + \frac{1}{Pe}\,\nabla^2\,T^{(n+1)}, \tag{3.14}$$

where $N^{(n)} = -(\boldsymbol{u}^{(\boldsymbol{n})} \cdot \nabla)\,T^{(n)}$. As it can be seen in (3.14), the diffusive term of the energy equation given by (3.12) is treated implicitly. This is done to improve the stability of the numerical scheme at larger values of the time step Δt, and this brings another equation with the Laplacian which is written as

$$\left(\nabla^2 - \frac{3\,Pe}{2\,\Delta t}\right)\,T^{(n+1)} = Pe\,\left(-2\,N^{(n)} + N^{(n-1)} - \frac{4\,T^{(n)} - T^{(n-1)}}{2\,\Delta t}\right) \tag{3.15}$$

and referred to as the Helmholtz equation.

The solution method implemented in the code for DNS of duct flows and applied for solving equation (3.15) is similar to the numerical method applied for solving equation (3.6).

3.3 The Poisson and Helmholtz equations

When integrating with respect to time the equations (3.11) and (3.12), equation (3.6) and equation (3.15) must be solved simultaneously. Both equations discussed in this section in more detail belong to the class of elliptic partial differential equations and require significant computational costs. The Poisson equation for the pressure given by (3.6) is considered first. At the end of this section some remarks about the solution of the Helmholtz equation for the temperature given by (3.15) are made.

3.3.1 The Poisson equation and its discretization

The Poisson equation can be written in a general form by introducing an unknown function $f = f(x, y, z)$ and a right-hand side function $r = r(x, y, z)$ as follows:

$$\nabla^2\,f = r, \quad (x, y, z) \in \Omega, \tag{3.16}$$

where Ω is a bounded, open domain in $\mathbb{R}^3$, with the following boundary conditions imposed at the boundary $\partial\Omega$, $(x, y, z) \in \partial\Omega$:

$$f = f_D, \tag{3.17}$$

$$\frac{\partial f}{\partial \boldsymbol{n}} = f_N, \tag{3.18}$$

where $\partial f/\partial \boldsymbol{n} = \nabla \cdot \boldsymbol{n}$ is the directional derivative of f, $\boldsymbol{n}$ is a unit vector which is normal to $\partial\Omega$ and directed outwards (see e.g. [46]). Condition (3.17) is referred to as the Dirichlet boundary condition, and (3.18) is the Neumann one (see e.g. [46]). In many cases both types of boundary conditions are imposed at separate sections of the boundary $\partial\Omega$. In addition, the third common type of boundary conditions which is a linear combination of (3.17) and (3.18) and which is referred to as the Cauchy (or Robin) boundary condition can be imposed, but it is not applied for solving problems discussed in the current work, and the first two conditions given by (3.17) and (3.18) are enough here.

Before going into details on numerical aspects of the Poisson equation given by (3.16), some remarks on a special problem should be given. The most problematic case is the Poisson equation with the pure Neumann boundary condition imposed at the whole boundary $\partial\Omega$, when it is not possible to obtain a unique solution. Namely, if f_0 is some solution of equation (3.16) with condition (3.18), then $f_0 + C$, C is any constant, is also solution. Usually, solutions of such problems are not interesting, but the gradient of the obtained solutions, ∇f_0, is needed. In this case, the right-hand side function r of (3.16) must be consistent with the Neumann boundary condition given by (3.18), which can be easily shown by integrating (3.16) over Ω and by using the Gauss-Ostrogradsky theorem:

$$\iiint\limits_{\Omega} r \, \mathrm{d}\Omega = \iiint\limits_{\Omega} \operatorname{div}(\nabla f) \, \mathrm{d}\Omega = \oiint\limits_{\partial\Omega} \nabla f \cdot \boldsymbol{n} \, \mathrm{d}S \oiint\limits_{\partial\Omega} \frac{\partial f}{\partial \boldsymbol{n}} \, \mathrm{d}S. \tag{3.19}$$

Thus, the function r and the directional derivative $\partial f/\partial \boldsymbol{n}$ cannot be arbitrary and must be carefully specified. Once the condition in (3.19) is satisfied, the problem given by (3.16) and (3.18) is well posed.

In the case of a rectangular box shown in figure 1.1(b), the directional derivative computed at any boundary as

$$\frac{\partial f}{\partial \boldsymbol{n}} = \nabla f \cdot \boldsymbol{n} = n_x \frac{\partial f}{\partial x} + n_y \frac{\partial f}{\partial y} + n_z \frac{\partial f}{\partial z} \tag{3.20}$$

is reduced to a partial derivative, because normal vectors at boundaries of a

rectangular cell have only one non-zero component ± 1, if the Cartesian coordinate system is chosen properly: each pair of opposite boundaries is perpendicular to one of the axes, which is schematically shown in figure 1.1(b).

To solve (3.16) numerically, a regular non-uniform grid is introduced into a computational domain, and a solution is found at nodes of the grid. The second order partial derivatives of the Laplacian are approximated by applying a central finite difference scheme according to the seven-point stencil shown in figure 3.3(a). For example, the second order partial derivative of the function f with respect to x is approximated at some node with coordinates (x_i, y, z) as

$$\frac{\partial^2 f}{\partial x^2} \approx \hat{a}_x\, f(x_{i-1}, y, z) + \hat{b}_x\, f(x_i, y, z) + \hat{c}_x\, f(x_{i+1}, y, z), \tag{3.21}$$

where index i runs over nodes along the x axis excluding nodes of the boundaries which are processed depending on a type of boundary conditions (see below in this section), $\hat{a}_x$, $\hat{b}_x$, $\hat{c}_x$ are constants computed by differentiating twice a quadratic polynomial which fits the unknown function f at the nodes with the x coordinates x_{i-1}, x_i, x_{i+1} and fixed y and z. It is clear that the coefficients $\hat{a}_x$, $\hat{b}_x$, $\hat{c}_x$ change from one node to another node in the general case of the non-uniform grid. The detailed description of the approximation done according to (3.21) is given in appendix B.1. The second order partial derivatives $\partial^2 f/\partial y^2$ and $\partial^2 f/\partial z^2$ are approximated in a similar way and are also given in appendix B.1. After approximating the second order partial derivatives included in the Laplacian, which is in turn included in equation (3.16), a system of linear equations to be solved is obtained:

$$A\,\boldsymbol{f} = \boldsymbol{r}. \tag{3.22}$$

The right-hand side vector $\boldsymbol{r} = (r_1, \ldots, r_N)^T$ of equation (3.22) consists of values of the right-hand side function r of equation (3.16) given at nodes of the grid enumerated from 1 to N (e.g. by using a lexicographic ordering). Thus, values of the unknown function f of (3.16) which form the vector of unknowns $\boldsymbol{f} = (f_1, \ldots, f_N)^T$ of (3.22) are found at the same nodes of the grid where the right-hand side function r is given.

3.3.2 Discretization of boundary conditions

Both the Dirichlet and Neumann boundary conditions can be incorporated into system (3.22). In the case of the Dirichlet boundary condition given by (3.17) and imposed at a boundary of a box, the function f at nodes of this

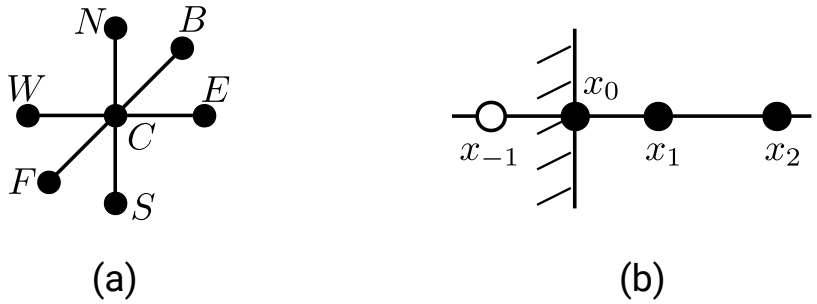

Figure 3.3: Sketches of the seven-point stencil *(a)* and the arrangement of nodes of the grid along the x direction near the boundary including ghost nodes *(b)*. In figure *(b)* the boundary is located at $x = x_0$; the ghost node is at $x = x_{-1}$; the successive nodes with the coordinates x_1 and x_2 belong to internal domain; coordinates y, z of the four nodes are fixed.

boundary is known, and corresponding values are added to the right-hand side vector $\boldsymbol{r}$ of (3.22). For example, if the boundary at $x = x_0$ has the Dirichlet condition, the term $\hat{a}_x\, f(x_0, y, z)$ of approximation (3.21) written for the node (x_1, y, z) is known and is transferred to the right-hand side, i.e. the vector $\boldsymbol{r}$. If the Neumann boundary condition given by (3.18) is imposed at a boundary, a corresponding partial derivative, which is obtained from the reduction of the directional derivative, can be approximated in two ways depending on a solution strategy.

1. The central finite difference scheme is applied with involving ghost nodes.

2. The one-sided finite difference scheme is applied without ghost nodes.

To explain ghost nodes introduced above and to illustrate the application of the two approaches, the partial derivative of the function f with respect to x, $\partial f/\partial x$, is considered only. The sketch of nodes applied for the discretization of $\partial f/\partial x$ is shown in figure 3.3(b). The approximation of the partial derivative at the node with the coordinates (x_0, y, z) can be done as follows:

$$\frac{\partial f}{\partial x} \approx \frac{f_1 - f_{-1}}{2\,\Delta x}, \tag{3.23}$$

$$\frac{\partial f}{\partial x} \approx a_x\, f_0 + b_x\, f_1 + c_x\, f_2, \tag{3.24}$$

where $f_i = f(x_i, y, z)$, $i = \{-1, 0, 1, 2\}$; the ghost node has $x = x_{-1}$; the boundary has $x = x_0$; x_1 and x_2 are the x coordinates of the successive internal nodes. The ghost node applied in (3.23) is symmetrical with respect to the boundary, i.e. $\Delta x = x_0 - x_{-1} = x_1 - x_0$. The distribution of the nodes with x_0, x_1, x_2 is

non-uniform, and approximation (3.24) is obtained by differentiating a quadratic polynomial which fits the unknown function f at nodes with the x coordinates x_i, $i = 0, 1, 2$ (y and z are fixed). This is similar to the procedure of computing the coefficients included in approximation (3.21). The procedure of the computation of the coefficients a_x, b_x, c_x included in (3.24) is given in detail in appendix B.2. The formulae applied for approximating the other two partial derivatives of f with respect to y and z in the case of the Neumann condition imposed at corresponding boundaries are similar to (3.23) and (3.24) and are provided in appendix B.2.

3.3.3 First computational strategy: ghost nodes

The first computational strategy assumes the application of ghost nodes which are excluded from the solution process by applying the central finite difference scheme which are similar to (3.23). The obtained expression of f at the ghost node is substituted into the formula of finite differences for equation (3.16) given at the node of the boundary close to the ghost node. One part of the expression is added to a corresponding coefficient of the matrix A of system (3.22), and another part is added to a corresponding element of the right-hand side vector $\boldsymbol{r}$. Thus, the matrix A contains unknown values of f at nodes of the internal domain and at nodes of boundaries with the Neumann boundary condition. All the unknowns are computed by solving the linear system given by (3.22).

To demonstrate the usage of the first strategy, the example given in (3.23) and shown in figure 3.3(b) is taken again, and the following expression of the value of f at the ghost node, $f_{-1} = f(x_{-1}, y, z)$, is obtained from (3.23):

$$f_{-1} = f_1 - 2\,\Delta x\,\frac{\partial f}{\partial x}, \tag{3.25}$$

where $\partial f/\partial x$ is given at the node of the boundary with the coordinates (x_0, y, z) The second order partial derivative of f with respect to x included in the Laplacian is approximated at the boundary node (x_0, y, z) by applying the central difference scheme as follows:

$$\frac{\partial^2 f}{\partial x^2} \approx \frac{f_1 - 2\,f_0 + f_{-1}}{\Delta x^2}, \tag{3.26}$$

where the notation is the same as the one used in (3.23) and (3.24). The value f_{-1} in (3.26) is replaced by the right-hand side of (3.25), and the obtained approximation of $\partial^2 f/\partial x^2$ at the boundary node with (x_0, y, z) contains only the unknowns $f_0 = f(x_0, y, z)$ and $f_1 = f(x_1, y, z)$ excluding the ghost node.

3.3.4 Second computational strategy: one-sided finite differences

The second computational strategy is realized by applying the one-sided difference formulae, which are similar to (3.24), for approximating first order partial derivatives on the non-uniform grid without using ghost nodes. In this case corresponding second order partial derivatives included in the Laplacian are approximated by the central differences similar to (3.21) at nodes of the internal domain near boundaries which have the Neumann condition. Corresponding first order partial derivatives are approximated by the one-sided difference formulae similar to (3.24), and values of f at nodes of the boundaries with the Neumann condition are expressed via values of f at the two successive adjacent nodes of the internal domain. The obtained expressions are substituted into approximations of the corresponding second order partial derivatives. Thus, the matrix A of system (3.22) does not contain unknown values of the function f at nodes of the boundaries with the Neumann condition. If the solution at such nodes is needed, it can be computed by using (3.24) and the solution obtained at internal nodes by solving system (3.16).

When returning to our example in (3.24), the value $f_0 = f(x_0, y, z)$ is expressed now as

$$f_0 = \frac{1}{a_x}\left(\frac{\partial f}{\partial x} - b_x\, f_1 - c_x\, f_2\right), \tag{3.27}$$

where the notation is the same as the one used in (3.24) and schematically shown in figure 3.3(b), and the partial derivative $\partial f/\partial x$ is given at the boundary node with (x_0, y, z). The expression of f_0 given in (3.27) is substituted into the approximation of $\partial^2 f/\partial x^2$ at the node (x_1, y, z) done according to (3.21) as follows:

$$\frac{\partial^2 f}{\partial x^2} \approx \hat{a}_x\, f_0 + \hat{b}_x\, f_1 + \hat{c}_x\, f_2. \tag{3.28}$$

After the substitution, the second order partial derivative included in the Laplacian and given by (3.28) contains only the values f_1 and f_2 and does not contain f_0. After solving system (3.22) the value f_0 at the boundary node can be computed by using (3.27).

3.3.5 Comparison of both computational strategies

Both strategies concern the realization of the Neumann boundary condition and differ mainly in the size of the matrix A of (3.22). In terms of computational costs, the second strategy can be more beneficial, because less unknowns are

included in system (3.22). The final step for computing values of the unknown function f at nodes of boundaries with the Neumann condition is done by applying simple arithmetical operations of the one-sided formulae, which are similar to (3.24). This advantage of the second strategy becomes especially important, if iterative methods, as discussed below in section 3.4.3, are applied for solving (3.22).

The drawback of the second strategy is that the solution of system (3.22) cannot be found at nodes of an edge which is common to two adjacent boundaries with the Neumann boundary conditions. An approximate solution at such nodes can be obtained only by extrapolating values at neighbour nodes where the solution is directly obtained. Nevertheless, the main question in choosing the computational strategy is whether values of the unknown function at such nodes are needed or not.

3.3.6 The Helmholtz equation

The Helmholtz equation given by (3.15) is similar to equation (3.6) and can be written by using $f = f(x, y, z)$ and $r = r(x, y, z)$ as follows:

$$\nabla^2 f + Cf = r, \quad (x, y, z) \in \Omega, \tag{3.29}$$

where C is a constant, and the other notation is the same as for the Poisson equation given by (3.16). Equation (3.29) is specified together with any type of the standard boundary conditions: the Dirichlet boundary condition given by (3.17) and the Neumann boundary condition given by (3.18). After applying the central differences to approximate the partial derivatives and after incorporating specified boundary conditions in the same way as it is done for the Poisson equation described above in this section, the Helmholtz equation with imposed boundary conditions are converted into a system of linear equations similar to the one given by (3.22). In the case of the pure Neumann problem, the Helmholtz equation has always a unique solution as opposed to the Poisson equation. Nevertheless, both equations are elliptic partial differential equations, and methods applied for solving the obtained linear systems can be exactly the same. A number of such solution methods are discussed below in section 3.4. Only the Poisson equation is used as an example of an elliptic partial differential equation.

3.4 Solution methods of elliptic equations

3.4.1 The Poisson equation and duct flows

In the case of duct flows, there is a streamwise direction, which coincides with the x direction shown in figure 3.1, and has the periodic boundary conditions imposed at the boundaries perpendicular to the x axis also shown in 3.1. The periodicity allows, in turn, to apply uniform grids along the x direction and to represent the unknown function f and the right-hand side function r included in equations (3.16) as Fourier series. In this case corresponding Fourier coefficients depend on the coordinate x and can be computed by applying an algorithm of the Fast Fourier Transform. By substituting the series into (3.16) and by grouping terms with the same Fourier coefficient, smaller problems are obtained:

$$\frac{\partial^2 \hat{f}_n}{\partial y^2} + \frac{\partial^2 \hat{f}_n}{\partial z^2} - \alpha_n^2 \, \hat{f}_n = \hat{r}_n, \tag{3.30}$$

where n is a Fourier mode, $\hat{f}_n = \hat{f}_n(y, z)$ and $\hat{r}_n = \hat{r}_n(y, z)$ are the Fourier coefficients of the unknown function and the right-hand side function, respectively, $\alpha_n = 2\pi n / L_x$ is the wavenumber, L_x the periodicity length, $n = 0, \ldots, N_x/2 - 1$ (the number of nodes along the x direction is equal to $N_x + 1$). After the decomposition along the x direction, every two-dimensional problem has boundaries at the rigid walls of a duct. Thus, boundary conditions for (3.30) are of the Neumann type and are given by (3.8). Each equation of the form given by (3.30) is discretized by using the central differences, and the obtained system of linear equations has to be solved.

In the DNS code for duct flows [44] the Poisson equation for the pressure given by (3.6) is solved in the way described just above, and the linear systems obtained after discretizing the two-dimensional problems given by (3.30) are solved by applying the cyclic reduction algorithm (see e.g. [46]) implemented in the FISHPACK package [48]. Each linear system is solved independently and in parallel, but the applied algorithm of FISHPACK is serial, which means a one-dimensional decomposition (along x) of the three-dimensional problem (i.e. into so-called "slices"). This type of decomposition imposes a limitation on a number of processors used for solving the three-dimensional problem in parallel. Nevertheless, the applied solution method for solving the Poisson equation is very effective and belongs to the class of direct methods. The same solution method is applied for solving the Helmholtz equation for the temperature given by (3.15). More detailed information on algorithmical aspects can be found in [44].

It should be noted that the advantage of the streamwise direction with the imposed periodic boundary conditions can be easily applied to the cylindrical geometry with its azimuthal direction due to the natural symmetry of the cylinder. A similar approach based on the FFT can be also applied to a rectangular computational domain which does not have lateral constraints in the horizontal directions (see e.g. [40]).

In the case of a rectangular box, which confines a convection flow by rigid walls, the presence of the walls perpendicular to both x and y, as shown in figure 1.1(b), leads to the formation of the viscous boundary layer. In order to resolve it well, a space interval of a grid along the horizontal directions should be chosen properly. Moreover, if a grid is uniform in one of the horizontal directions, it should be uniform in another one due to the requirement of the symmetry of the horizontal directions to avoid any preferable (horizontal) direction. If a grid is uniform in the vertical direction, proper resolution of the viscous and thermal boundary layers at the horizontal plates is needed, and it is more important than in the case of the uniform horizontal directions which should resolve only the viscous boundary layer at the sidewalls. In any case, for grids of a rectangular box which are uniform in one or more directions, the adequate resolution of the BL at the walls leads to an excessive number of nodes in the bulk of a convection cell. Thus, the application of such grids is not reasonable, because they involve computational overheads due to additional nodes and extra data to be processed. But in the case of a non-uniform grid, the approach for solving the Poisson and Helmholtz equations based on the Fourier series expansion is not applicable anymore.

As for the other arithmetical operations involved in the numerical scheme described above in section 3.2, they do not depend on the type of boundary conditions and on applied grids. Thus, to develop new code for DNS of turbulent convection flows in extended closed rectangular boxes based on the code applied for DNS of duct flows, the solution method of the Poisson equation for the pressure given by (3.6) and of the Helmholtz equation for the temperature given by (3.15) should be replaced in the old code. In this regard, the following base requirements are to be satisfied while choosing a new numerical method.

1. The grid is non-uniform in all directions and is clustered near rigid walls.
2. Both horizontal directions are symmetrical without a preferable direction.
3. All computations are done in parallel (at least on the level of distributed memory architectures with using the MPI specification).
4. Two-dimensional decomposition of computational domain is supported.

The fourth point of the above list is important while solving problems with cells of large aspect ratio and means that the domain is divided into "blocks" along two axes rather than "slices" along one axis only as it is the case in the original code for duct flows.

It is demonstrated above in section 3.3 that both the Poisson equation and the Helmholtz equation given by (3.16) and (3.29), respectively, can be reduced together with their boundary conditions to systems of linear equations of the form given by (3.22) after performing the discretization. The matrix A of the system is typically structured and has seven non-zero diagonals according to the applied seven-point stencil shown in figure 3.3(a), i.e. the matrix is mostly sparse. The sparsity of the matrix is highly exploited in developing numerical methods for solving such systems as it gives an advantage in terms of memory storage. There are two large classes of methods for solving sparse systems of linear equations: direct methods (see e.g. [49] and [50]) and iterative methods (see e.g. [46]). Solution methods of both groups are discussed and compared below in the next subsections of the current section. The tested techniques meet all the four general requirements of the new code for performing DNS of a turbulent convection flow in a rectangular box. But the fact that such convection flows are in cells of large aspect ratios and at high Rayleigh numbers implies the use of large grids, and this imposes limitations on application of possible techniques.

3.4.2 Direct methods

Direct methods for solving sparse linear systems are robust and allow to obtain an exact solution (up to machine precision). Most of such approaches are based on the LU factorization of the initial matrix A of a system of the type given by (3.22). The idea is to present A as the product of the lower triangular L and upper triangular U matrices, i.e. $A = LU$. Once the factorization has been done, the initial system written in (3.22) is converted into $LU\,\boldsymbol{f} = \boldsymbol{r}$, which is solved by performing two steps: the system $L\,\boldsymbol{y} = \boldsymbol{r}$, where $\boldsymbol{y} = U\,\boldsymbol{f}$, is solved to obtain $\boldsymbol{y}$ (a forward elimination step); the system $U\,\boldsymbol{f} = \boldsymbol{y}$ is solved to find $\boldsymbol{f}$ (a backward elimination step). Both solution steps are straightforward as the involved matrices are tridiagonal. However it is much more difficult to obtain the LU decomposition at the very beginning. The significant problem while performing the factorization is to minimize introduced non-zero elements (fill-ins) of the factors L and U. Algorithms applied for factorizing can be very different and can also use other properties of the matrix A (whether it is symmetric, positive definite, etc.). They involve a lot of techniques from numerical algebra, graph theory, permutations,

and other topics of discrete mathematics (see e.g. [49; 50]). More difficulties arise, if such algorithms are developed for a parallel execution (see e.g. book [51] or review [52]). All this material cannot be covered in the frame of the current work, and further details on direct methods and applied techniques can be found in the above cited literature.

The MUMPS package [53] can be considered as an example of implementation of a direct method applied for solving the sparse system of linear equations given by (3.22). This software tool was chosen and tested due to advantages it offers.

- It is applied for solving general unsymmetric matrices.
- It performs all computations in parallel on distributed memory computers.
- It is robust and requires minimum settings for a solution.
- There are also options for fine-tuning and controlling the solution process (interface for including different ordering algorithms, error analysis, etc.).

At the same time, the main disadvantage of the direct solver, which is intrinsic to all methods based on the LU factorization, is a significant memory consumption during the factorization step. Despite many precautions done for eliminating the memory issue (i.e. the emergence of fill-ins), it is still problematic for very large systems, and it is getting more considerable as long as the linear system grows. Another limitation is related to the factorization process, which is also time consuming and is done once before solving the system of equations. At the time when the MUMPS was being tested, it did not have any option to store the matrices L and U of the obtained decomposition for reading them afterwards. This meant that the factorization had to be done each time after restarting computations, even if the matrix A of the system was not changed.

Thus, the experience showed that direct methods based on the LU factorization are not very well suited for solving large problems as discussed above in section 3.1, mainly because of the large memory consumption during the factorization. The property to preserve the sparsity of the matrix becomes more significant rather than the capability to obtain the exact solution.

3.4.3 Iterative methods

As opposed to direct methods applied for solving systems of linear equations of the form given by (3.22), iterative methods provide an approximate solution of a system by taking an initial guess and by performing a finite number of operations

referred to as an iterative process. Usually a stopping criterion of the iterative process is a given tolerance ϵ being compared with the ratio of the norm of a residual vector, computed as $A\,\boldsymbol{f}_k - \boldsymbol{r}$, and the norm of the right-hand side vector $\boldsymbol{r}$:

$$\frac{\|A\,\boldsymbol{f}_k - \boldsymbol{r}\|}{\|\boldsymbol{r}\|} \leq \epsilon, \tag{3.31}$$

$\boldsymbol{f}_k$ is an approximate solution obtained on the kth iteration, and the norm of a vector is computed by any conventional formula (see e.g. [46]). If the given tolerance ϵ is not achieved within a given number of iterations, then the applied method does not converge. In this case, the iterative process can be restarted, or the tolerance can be increased. The convergence rate of the solution process significantly depends on an initial approximate solution and on properties of the matrix A of the system. The latter can be improved in terms of the convergence speed by applying preconditioning techniques for transforming the initial system (the matrix A) into another one with the same solution.

During the last decades some efficient iterative methods were developed and thoroughly studied. The most applicable and practical iterative techniques for solving large systems of linear equations are based on a projection process, when an approximate solution is extracted from some subspace (particularly the Krylov subspace). The outstanding property of iterative methods to preserve the sparsity of the matrix A was successfully incorporated in algorithms, and the issue of significant memory consumption which is typical for direct methods based on the LU factorization was resolved. Thus, iterative methods could be considered as more applicable for problems with large systems of linear equations, if they converge quite well. A nice description of the theory on such methods and the best techniques can be found in book [46].

Nevertheless, a common drawback of all standard iterative techniques (regardless use of preconditioning) is a significant decrease of their convergence rate as long as the size of the problem increases. In other words, the number of iterations to be performed to achieve a given tolerance is getting larger as long as the number of unknowns (i.e. the grid size) increases. To overcome the deterioration in the convergence rate, special iterative techniques referred to as multigrid methods were devised (see e.g. [46; 54]). It should be noted that multigrid is not a single method which can be easily described as a distinct algorithm and implemented accordingly. Rather, it is an approach based on many ideas which build a solution method of a particular system of linear equations, and a single method can be implemented in many different ways which primarily depend on a problem (equations to be solved, discretization scheme, eigenvectors of the corresponding system, computational

domain, and so on). A notable distinction between multigrid and other iterative techniques is that the former takes much more information on a problem (rather than just the matrix of the system and the right-hand side).

Multigrid methods were initially developed for problems obtained from the discretization of elliptic partial differential equations, which is the case of equation (3.16). A basic idea of a multigrid method came from an observation of behaviour of some "general-purpose" iterative techniques and was related to reduction of components of errors (or residuals) during the iterative process. Namely, such methods (e.g. the Jacobi and Gauss-Seidel methods) eliminate effectively high-frequency components of the error (or oscillatory modes) but leave low-frequency components (so-called smooth modes) almost unchanged. While the latter are difficult to dump on a current (fine) grid, a lot of them can be mapped into high-frequency modes on a coarser grid, where they can be reduced much faster. Thus, the idea is to move through a hierarchy of coarse grids for eliminating smooth components of the error and to return an obtained solution back on the original (fine) grid to use it further. Multigrid techniques were later extended for solving other types of equations including non-linear ones.

Implementation of a multigrid method (even for the simplest case of an elliptic equation in a rectangular box) involves a lot of questions (starting from constructing the hierarchy of grids and finishing with algorithms for transferring solutions back and forth between the grids). Known issues arise in dealing with non-uniform grids and variable-coefficients problems, which slow down the convergence of multigrid, and there are different measures to handle these problems. A lot of further difficulties are related to parallelization of applied algorithms, which is an important issue in solving large problems. Thus, implementation of multigrid becomes an independent challenging project.

3.4.4 Multigrid solvers of the Hypre package

A number of iterative methods (or solvers), which were designed especially for high-performance computing, can be found in the Hypre package [55; 56] developed in the Lawrence Livermore National Laboratory. Particularly, two parallel semicoarsening multigrid solvers, SMG and PFMG, are available in the package and are applied for solving systems of linear equations obtained after finite difference, finite volume, or finite element discretizations of the diffusion equation, which is the generalization of equations (3.16), (3.29). In this case, the computational domain must consist of adjacent rectangular boxes (or subdomains) with regular grids applied for discretizing. The two solvers are similar in common

but have some differences in algorithms, and in practice it leads to different behaviour while computing: SMG is more robust but less efficient in terms of memory/performance as opposed to PFMG. Both multigrid solvers are available via the Structured-Grid System interface (Struct) which was introduced in Hypre along with other so-called conceptual interfaces. The Struct interface allows to describe a problem in terms of grids and stensils without forming the matrix A of a linear system directly, and this simplifies also realization of boundary conditions. Moreover, this interface gives the advantage to use large regular grids, and the total number of unknowns of the system (i.e. the size of the matrix A) is not needed to be stored. The access to nodes of a grid is done by using indices of the nodes along three directions which form the Cartesian coordinate system rather than by using the global index (e.g. in the case of the lexicographic ordering). Further details on the implementation of SMG and PFMG, and conceptual interfaces can be found in [56]. The application of these multigrid solvers in the code for DNS of convection flows in rectangular boxes is discussed below in section 3.5.

3.5 Mathematical model for turbulent convection in rectangular box

As it can be seen, the governing equations of duct flows given by (3.1), (3.11), and (3.12) are easily converted to the governing equations of convection flows in rectangular boxes given by (1.11)-(1.13), if the free-fall velocity $\tilde{U}_f$ defined in (1.8) and the cell height $\tilde{H}$ are substituted into the Reynolds number Re defined in (3.3) and the Peclet number Pe defined in (3.13). The obtained Reynolds Re_f and Peclet Pe_f numbers are expressed in terms of Ra and Pr as follows:

$$Re_f = \sqrt{\frac{Ra}{Pr}}, \qquad Pe_f = \sqrt{Ra\,Pr}. \tag{3.32}$$

The code obtained after integrating the new numerical method for solving the system of linear equations of the form given by (3.22) obtained after discretizing the Poisson and Helmholtz equations given by (3.16) and (3.29), respectively, together with included boundary conditions, is applied for performing direct numerical simulations of Rayleigh-Bénard convection in laterally confined samples of rectangular cross section. The governing equations given by (1.11)-(1.13) are solved numerically by applying the scheme described above in section 3.2. The multigrid solver of Hypre, SMG or PFMG, is applied to solve the Poisson equation for the pressure given by (3.6) and the Helmholtz equation for the temperature

given by (3.15) on each time step. The former is solved with the Neumann boundary conditions given by (3.8) and imposed at all the walls of a rectangular box. The latter has the Dirichlet boundary conditions at the bottom ($T = T_1$) and top ($T = T_2$) plates, and the Neumann boundary conditions $\partial T/\partial \boldsymbol{n} = 0$ at the sidewalls.

As it is stated above in section 3.3, the Laplacian included in the elliptic partial differential equations is discretized by applying the seven-point stencil shown in figure 3.3(a) and the central differences similar to (3.21) and discussed in more detail in appendix B.1. The Neumann boundary condition is realized according to the second computational strategy discussed above in section 3.3.4. Thus, regardless the type of imposed boundary conditions, the linear system of the form given by (3.22) obtained after discretizing either the Poisson equation or the Helmholtz equation includes only unknown values at nodes of the internal domain. One of the multigrid solvers of Hypre is applied to solve this system and to obtain an approximate solution at nodes of the internal domain (excluding boundaries). Having obtained the solution at nodes of the internal domain, values at nodes of boundaries with the Dirichlet conditions are known, the solution at nodes of boundaries with the Neumann conditions is computed by using the one-sided finite difference formulae, which are similar to (3.27). Further information on the computation of the solution at boundaries with the Neumann condition can be found in appendix B.2. The computational domain is schematically shown in figure 3.4 for the case of the pure Neumann problem.

It should be noted that according to the chosen computational strategy, if the Neumann boundary conditions are imposed at two boundaries of a rectangular box which have a common edge, the solution at nodes of the common edge cannot be defined. For the particular case of the box shown in figure 3.4, the solution at nodes of the edges of the box is unknown. The only way to obtain the solution at nodes of such edges could be extrapolation by using the obtained solution at neighbour nodes. Without extrapolating, if the solution is not defined at nodes of edges, the main question is whether these values are needed in further computations or not.

Particularly, in the case of the Poisson equation for the pressure given by (3.6) with the Neumann boundary conditions imposed at all the boundaries of a rectangular box, the pressure $p^{(n+1)}$ is unknown at nodes of the edges, but it is needed to correct the velocity $\boldsymbol{u}^{(n+1)}$ from equation (3.7) computed at nodes of the collocated grid and velocity fluxes computed at nodes of the staggered grid, as it is discussed above in section 3.2. As a fact, the velocity at the boundaries is

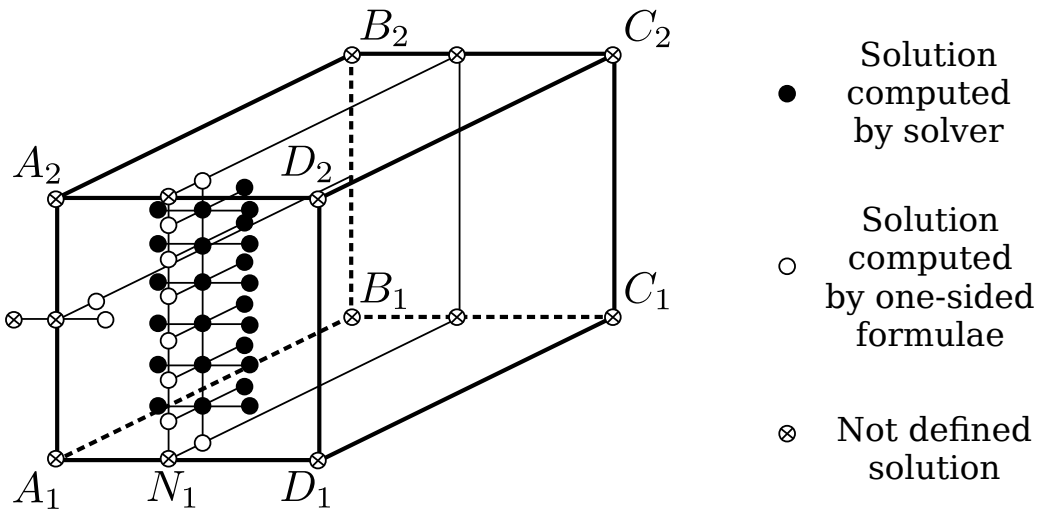

Figure 3.4: The sketch of the computational domain where some nodes are shown with different symbols to distinguish the ways of the computation of corresponding values of the solution according to the second computational strategy discussed in section 3.3.4. All the boundaries of the box are assumed to have the Neumann condition, and the solution at nodes of the edges is not defined. For example, node N_1 and corner nodes A_i, B_i, C_i, D_i, $i = 1, 2$, are not processed. Nodes which belong to the internal domain are denoted by the *solid circles*. Nodes of the boundaries excluding edges are denoted by the *empty circles*. Nodes of the edges (including the corners) are denoted by the *circles with crosses*.

defined automatically due to the no-slip condition at the walls, i.e. $\boldsymbol{u}^{(n+1)} = 0$. As for velocity fluxes, first they are applied for discretizing the term $(\boldsymbol{u} \cdot \nabla)\,\boldsymbol{u}$ included in (1.12) and the term $(\boldsymbol{u} \cdot \nabla)\,T$ in (1.13). In every case the operator is expressed in the Cartesian coordinate system as

$$\boldsymbol{u} \cdot \nabla = u_x \frac{\partial}{\partial x} + u_y \frac{\partial}{\partial y} + u_z \frac{\partial}{\partial z}, \tag{3.33}$$

and again, it is equal to zero at the walls due to the no-slip condition. In addition, velocity fluxes are used for estimating the incompressibility of the flow by applying approximation (3.9). In the Cartesian coordinate system $\operatorname{div} \boldsymbol{u}$ is expressed as

$$\operatorname{div} \boldsymbol{u} = \frac{\partial u_x}{\partial x} + \frac{\partial u_y}{\partial y} + \frac{\partial u_z}{\partial z}. \tag{3.34}$$

If the divergence of the velocity given by (3.34) is computed at any node of any edge of a box (e.g. node N_1 and all the corner nodes shown in figure 3.4), it must be equal to zero due to the definition of the partial derivatives included in (3.34) and the no-slip condition, i.e. $\operatorname{div} \boldsymbol{u} = 0$ at nodes of the edges. Thus, values of the pressure $p^{(n+1)}$ at nodes of the edges of a rectangular box are not needed, and the

second solution strategy is applicable in this case. From the computational point of view, it facilitates the solution process of equation (3.6), and this is especially important for iterative methods. In this regard, the second computational strategy is more beneficial.

In the case of the temperature $T^{(n+1)}$ obtained by solving (3.15), its values at nodes of the edges are computed by using the Dirichlet boundary conditions imposed at the bottom and top plates, which are enough to compute the solution at all nodes of the sidewall which have the zero Neumann boundary condition (no heat flux).

The Hypre solvers, SMG and PFMG, which are used for solving the elliptic partial differential equations, support three-dimensional decomposition of the computational domain. But in the current version of the code the two-dimensional decomposition is realized by dividing the domain into "blocks" (or partitions) along the axes y and z. Each partition is processed in parallel by using the MPI specification and has layers of ghost nodes of both the collocated grid and the staggered grid. Values of parameters at such ghost nodes are computed in two ways depending on a type of a boundary of a partition. If a boundary is a part of the walls of a rectangular box, values at ghost nodes are computed by extrapolating from the internal domain as it is mentioned above in section 3.2. If a boundary belongs to the internal domain and to a neighbour partition, values at ghost nodes attached to the first boundary are copied from the neighbour partition, and after computation both partitions exchange obtained values, and so on. The idea of the arrangement of ghost nodes is explained by figure 3.5 where the one-dimensional decomposition along the y axis is shown for the sake of simplicity.

An important question while dealing with iterative solvers is to choose the tolerance used as the stopping criterion of the iterative process. In the case of the temperature, there is no ambiguity, because it is obtained directly by solving (3.15). As for the pressure obtained by solving (3.6), the main criterion of a proper tolerance is $\operatorname{div} \boldsymbol{u}$ approximated by (3.9). The divergence of the velocity estimated after correcting velocity fluxes by the pressure depends both on the tolerance of the solver used for the pressure and on the time step Δt applied for integrating over time and introduced above in section 3.2. Thus, to satisfy the condition of the incompressibility, the tolerance of the applied multigrid solver has to be changed, if the time step is changed. The overall level of the divergence of the velocity is naturally defined by searching for supremum over the whole domain of

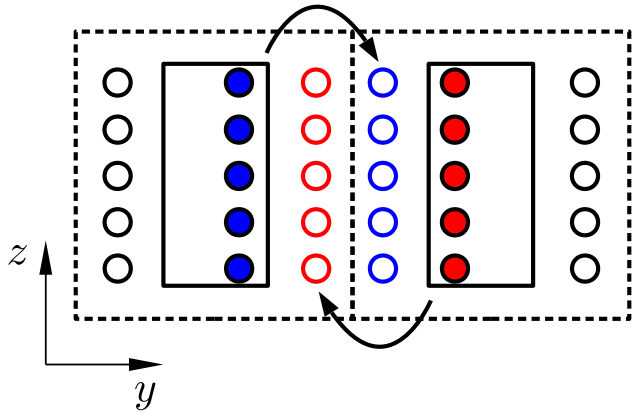

Figure 3.5: The sketch of the one-dimensional decomposition along the y axis where the two neighbour partitions have ghost nodes and exchange data with each other. Ghost nodes are denoted by the *empty circles*. Nodes which are processed within the partitions and copied into ghost nodes are denoted by the *solid circles*. The arrows show the directions of movement of data transferred before and after computations between the partitions being processed in parallel. Ghost nodes at the other boundaries are arranged similarly but not shown in the figure.

a rectangular box, Ω, which is simply the maximum:

$$\sup_{\Omega} |\operatorname{div} \boldsymbol{u}|, \tag{3.35}$$

where the divergence is approximated by using (3.9) and computed at every node.

3.6 Conclusions

The multigrid solvers included in the package Hypre (SMG and PFMG) were successfully implemented for solving the elliptic partial differential equations given by (3.6) and by (3.15). The obtained solver was successfully integrated in the old code for duct flows, and the new code can be applied for performing three-dimensional DNS of turbulent convection flows in closed rectangular cells. All the main requirements listed above in section 3.4.1 are satisfied. As an example of application of the new DNS code, the study related to the hypothesis of the ergodicity was done (see chapter 4).

It should be noted that iterative techniques become more efficient in comparison with FFT-based methods especially for problems with large aspect ratios, because the application of non-uniform grids allows to avoid excessive nodes in the bulk of a cell, while the FFT requires only uniform grids, which involves computational overheads. In this regard, the development of the numerical method which deals

with non-uniform grids was rewarded, because the study of the ergodicity requires storage of large data. The use of the old FFT-based method would make the study impossible due to lack of storage, time-consuming analysis, and other issues discussed in section 3.4.1.

In addition to the two multigrid solvers, the Struct interface of Hypre mentioned above in section 3.4.4 allows to apply easily some other iterative solvers available in the package for solving the elliptic equations. Particularly, the GMRES and some of its variations were tested and compared with the multigrid solvers. As it is stated in literature (see e.g. [46; 54]), experience showed that multigrid techniques are the most efficient, if they work for a particular problem.

As a further extension of the numerical method, the Dirichlet and Neumann boundary conditions given by (3.17) and (3.18) can be supplemented with periodic boundary conditions. On the one hand, it will be possible to study the effect of lateral constraints in extended convection systems by applying the same solver based on the same technique. On the other hand, such conditions allow to use grids which are uniform in both horizontal directions, and the FFT becomes applicable (see e.g. [40]). In this case the efficiency of the multigrid solver in comparison with the FFT could be questionable, but this should be tested.

As an extension for ordinary convection problems, the developed DNS solver can be easily adapted to magnetohydrodynamic problems in closed rectangular cells by including equations related to electrically conducting fluids in the presence of the magnetic field. In this case, an additional elliptic equation for the electric potential arises (see e.g. [44; 47]), and the numerical method based on the multigrid solvers is applicable for solving this equation.

Chapter 4

Numerical studies of ergodicity in convection flows

4.1 Introduction

4.1.1 Study of turbulent flows and main issues

Direct study of turbulent flows by analysing instantaneous fluid dynamic fields is challenging, because such flows, as opposed to the laminar case, are characterized by irregular, complex, and disordered variations of macroscopic parameters (the velocity, the temperature, the pressure, and so on). One can say that these varying fields consist of fluctuations which change rapidly both in space and in time making the structure of a turbulent flow very complicated for analysis. If the Navier-Stokes equations are applied to describe turbulent flows, their solutions should be represented by very complex integrals which are difficult to be found and should be very sensitive to initial conditions with imposed small disturbances which are almost always not known in advance. Another problem related to uncontrollable infinitesimal disturbances is that turbulent flows cannot be exactly reproduced in experiments. In other words, giving the same control parameters of a flow, the same boundary conditions, and almost the same initial conditions, any fluid dynamic field of the turbulent flow measured at a fixed moment of time and at a fixed point of space will have completely different values in every new experiment. The fact that each realization of a turbulent flow gives different unpredictable values of fluid dynamic parameters allows to consider corresponding fields as random and to apply methods of the probability theory, which is discussed below in section 4.1.3.

All these difficulties connected with analysis and study of a turbulent flow

make it reasonable to average instantaneous fluid dynamic fields by any procedure and to study mean ("smooth") fields which vary slowly and have a more regular structure without sharp fluctuations. In this case, obtained averaged smooth quantities of a turbulent flow can be studied by means of ordinary mathematical analysis and can provide some invariant characteristics of the flow which are preserved despite its detailed turbulent nature. In this regard, averaged quantities are reproducible despite small perturbations of initial conditions.

The question of the choice of an applied procedure for averaging is crucial and is determined by general requirements. As it is stated in [57], the most important requirement of an averaging procedure is to obtain relatively simple differential equations of mean quantities. The first and well-known approach for obtaining such equations in the case of an incompressible flow was suggested by O. Reynolds. The idea used for deriving the Reynolds equations is based on the decomposition of any fluid dynamic quantity f into the mean value $\overline{f}$ and the fluctuating part f', which is today known as the Reynolds decomposition (see e.g. [16; 57]):

$$f = \overline{f} + f'. \tag{4.1}$$

In correspondence with equation (4.1), the velocity components u_i, $i = 1, 2, 3$, the temperature T, and the pressure p, which are important in studying incompressible convection flows, are represented as follows:

$$u_i = \overline{u}_i + u_i', \qquad T = \overline{T} + \theta', \qquad p = \overline{p} + p'. \tag{4.2}$$

The quantities represented in the forms given by (4.2) are substituted in the Navier-Stokes equations given by (1.11)-(1.13) for an incompressible convection flow, and the obtained equations which include the mean quantities and the fluctuating parts are averaged by using a proper procedure (two common types of averaging are discussed in sections 4.1.2 and 4.1.3). To obtain the Reynolds equations, the chosen procedure of averaging must satisfy the following conditions:

$$\overline{f + g} = \overline{f} + \overline{g}, \tag{4.3}$$

$$\overline{af} = a\overline{f}, \tag{4.4}$$

$$\overline{a} = a, \tag{4.5}$$

$$\overline{\frac{\partial f}{\partial s}} = \frac{\partial \overline{f}}{\partial s}, \tag{4.6}$$

$$\overline{\overline{f} g} = \overline{f}\,\overline{g}, \tag{4.7}$$

where $f = f(\boldsymbol{x}, t)$, $g = g(\boldsymbol{x}, t)$ are some fluid dynamic fields, $\boldsymbol{x} = (x_1, x_2, x_3)$, a is a constant, s in (4.6) is x_i, $i = 1, 2, 3$, or t. More details on the decomposition given by (4.1) and the derivation of the Reynolds equations can be found in such books as [16; 57; 58].

In the next two subsections, 4.1.2 and 4.1.3, standard methods for obtaining smooth quantities are briefly described. In section 4.1.4 both approaches are compared. Finally, one of the main problems of the theory of turbulence studied in the frame of the present work is formulated in section 4.1.5.

4.1.2 Averaging over time and space

While conducting experiments or numerical simulations, it is more convenient to apply averaging over time discussed in this subsection, because all data needed for analysis can be obtained during one experiment (or one run) as opposed to the method discussed below in section 4.1.3. In a simple case, a field $f = f(\boldsymbol{x}, t)$ given at some fixed point $\boldsymbol{x} = (x_1, x_2, x_3)$ is averaged over time by using the general equation

$$\overline{f}(t) = \int_{-\infty}^{+\infty} f(t - \tau)\omega(\tau)\,\mathrm{d}\tau, \tag{4.8}$$

where function ω is a weighting function normalized as

$$\int_{-\infty}^{+\infty} \omega(\tau)\,\mathrm{d}\tau = 1. \tag{4.9}$$

Equation (4.8) can be written in the simplest form when the time averaging is done over some interval T:

$$\overline{f}(t) = \frac{1}{T} \int_{t-T/2}^{t+T/2} f(\tau)\,\mathrm{d}\tau. \tag{4.10}$$

In general, the function ω can be chosen depending on moments of time which are more important during averaging. Averaging over space coordinates, x_i, $i = 1, 2, 3$, is done similar to the time averaging by applying (4.8) with a chosen function ω or by (4.10) over some space intervals.

It can be seen that in the case of averaging over time done by applying (4.10), the four conditions in (4.3)-(4.6) are satisfied exactly. As for the fifth condition given by (4.7), it is not exactly satisfied for any time interval (see e.g. [57]). This

condition can be fulfilled up to certain accuracy, when the interval is assumed to be large enough in comparison with characteristic periods of fluctuating parts (which means $\overline{f'} = 0$) but small enough in comparison with characteristic periods of mean quantities ($\overline{\overline{f}} = \overline{f}$). The problem of choosing such intervals for a turbulent motion still exists and is discussed in [57].

Due to the problem of the averaging done by (4.10), when the fifth condition is not satisfied exactly, and due to the choice of the most suitable ω included in (4.8), which can depend on a particular flow, it can be advantageous to take another procedure for averaging turbulent fields. This is the method which is based on a statistical approach and described below in section 4.1.3. The method does not have the aforementioned problems and is applied commonly in the theory of turbulence.

4.1.3 Averaging over ensemble

The extensive theory on the statistical approach described in this subsection can be found in [57]. Here only the information which is relevant to the main problem of the present work is given.

The method of averaging discussed here is based on the use of data obtained from a series of independent experiments which can be considered as realizations of a particular flow and constitute a statistical ensemble of similar flows. Flows observed in all these experiments have the same control parameters, the same boundary conditions, and similar initial conditions, which differ by small disturbances. Each flow of an experiment provides a single set of data applied for averaging, as opposed to the averaging over time, when all data are obtained during a single long-term experiment discussed above in section 4.1.2. In the case of ensemble of experiments, a mean value of any fluid dynamic quantity f at a fixed space-time point $M = (\boldsymbol{x}, t)$ is computed as an arithmetic mean of a series of values of f obtained in every realization of a flow at the same point M. As it is mentioned above in section 4.1.1, all values of f obtained from the experiments of the series (or the statistical ensemble) have different unpredictable irregular values and can be considered as random. If the numbers of realizations is large, the obtained arithmetic mean of f differs slightly and fluctuates near some value $\overline{f(\boldsymbol{x}, t)}$ called a probability mean of the quantity f at the point M. By applying the probability theory, one can introduce the probability density function (the p.d.f. or the probability density), $\rho(f)$, of the quantity f which has random values

for each flow of the ensemble at the fixed point $M = (\boldsymbol{x}, t)$:

$$P\{f \in (f_0, f_0 + \Delta f)\} = \rho(f_0)\,\Delta f, \tag{4.11}$$

where P is the probability that a value of f belongs to the interval $(f_0, f_0 + \Delta f)$. By knowing $\rho(f)$, the mean probability $\overline{f(\boldsymbol{x}, t)}$ is defined by equation

$$\overline{f(\boldsymbol{x}, t)} = \int_{-\infty}^{+\infty} f\,\rho(f)\,\mathrm{d}f. \tag{4.12}$$

In addition, the probability mean of any function of f, $F(f)$, is computed as

$$\overline{F\,(f(\boldsymbol{x}, t))} = \int_{-\infty}^{+\infty} F(f)\,\rho(f)\,\mathrm{d}f. \tag{4.13}$$

It should be noted once again that the quantity f has random values at the fixed point $M = (\boldsymbol{x}, t)$.

In the case of turbulent flows which occur in domains and during some time, their study involves analysis of fluid dynamic fields assumed to be random. This means that the random quantity f used above as the example is given at multiple space-time points $M_i = (\boldsymbol{x}_i, t_i)$, $i = 1, \ldots, n$, where n is the number of such points. In addition to the probability density functions given for every fixed point M_i, $i = 1, \ldots, n$, the arithmetic mean of two values $f(M_1)$ and $f(M_2)$, at the first two points $M_i = (\boldsymbol{x}_i, t_i)$, $i = 1, 2$, is needed also to be statistically stable. This in turn implies the existence of a two-dimensional probability function $\rho_{M_1 M_2}(f(M_1), f(M_2))$ which is defined similar to (4.11). In a general case of n values of f given at n points $M_i = (\boldsymbol{x}_i, t_i)$, $i = 1, \ldots, n$, an n-dimensional density function $\rho_{M_1 \ldots M_n}(f(M_1), \ldots, f(M_n))$ is introduced by using the probability P_n:

$$\begin{aligned} P_n &= P\left\{f(M_i) \in \left(f_i^{(0)}, f_i^{(0)} + \Delta f_i\right), i = 1, \ldots, n\right\} = \\ &= \rho_{M_1 \ldots M_n}(f_1^{(0)}, \ldots, f_n^{(0)})\,\Delta f_1 \ldots \Delta f_n. \end{aligned} \tag{4.14}$$

Thus, the random field $f(\boldsymbol{x}, t)$ given at n space-time points implies the existence of all possible density functions of the form given by (4.14), which have some properties discussed in the above-mentioned book. Two turbulent flows are considered to be identical, if their density functions are the same.

In the case of a turbulent incompressible convection flow, there are at least five fields to be found ($\boldsymbol{u} = (u_1, u_2, u_3)$, p, T) given at any space-time point,

and these fields are assumed to be random and have their own set of probability density functions. Moreover, different fields are statistically connected to each other, which means the existence of so-called joint probability density functions given at different space-time points. Thus, the mean value of any function of fluid dynamic quantities is determined as the integral of the product of the function with corresponding joint probability densities.

The main idea of the approach is that mean quantities are well determined by using probability densities and equations similar to (4.12) and (4.13). In this case, the conditions given by (4.3)-(4.7) are satisfied exactly. From a mathematical point of view, it is a universal and reliable definition of the mean quantity obtained by averaging over ensemble. This mathematical approach was initially developed A.N. Kolmogorov, and it is nicely described in [57], where a number of references to other works are also provided.

4.1.4 Relation between averaging over time and ensemble

Before going into details on the relation between the two approaches described above in sections 4.1.2 and 4.1.3, both methods should be illustrated. This can be done by introducing a concept of a dynamical system together with its generalized coordinates (or degrees of freedom), which form a space of states. A state of the system at any moment of time corresponds to a point of this space (see e.g. [1; 57]). In this regard, a turbulent flow with its complicated structure of the velocity field and other quantities can be considered as a system but with very large number of generalized coordinates. Mathematically it means a decomposition of the flow motion into elementary components by representing the velocity field as a series expansion of orthogonal functions when expansion coefficients are coordinates in the space of states. For flows which occur in bounded domains (the case of a convection cell), the number of generalized coordinates is a countable set, and this number is limited due to the presence of the viscosity (see e.g. [57]). In addition, a generalized velocity is defined to describe the dynamics of the dynamical system, and generalized coordinates with components of the generalized velocity form a so-called phase space. Thus, a complete state of the system at any moment of time is determined by a point in the phase space, and the transition from one state to another one is represented by a trajectory in the phase space.

The diagrams of a phase space of a turbulent flow (e.g. a convection flow in a cell) are shown in figures 4.1(a) and 4.1(b). A trajectory of a long-term experiment (or a so-called run) observed during a long period of time is shown in figure 4.1(a). Trajectories of a series of short-term experiments (or runs) which evolve during

a shorter period of time are shown in figure 4.1(b). The flow in the long-term experiment and all realizations of this flow in the short-term experiments begin with the same boundary conditions but different (perturbed) initial conditions and evolve with exactly the same control parameters (Ra, Pr, Γ) which correspond to the turbulent regime. The external conditions of the experiments are stationary, and the flows come to the state of developed turbulent flow denoted by different points of a subdomain Φ of the phase space shown in figures 4.1(a) and 4.1(b). It should be noted that due to uncontrollable infinitesimal perturbations of initial conditions, all the trajectories cannot be identical. In the case of the long-term experiment shown in figure 4.1(a), the flow achieves the state of developed turbulent flow which correspond to some point of the subdomain Φ and remains inside Φ during the rest of the observation time. The short-term experiments shown in figure 4.1(b) are observed until they achieve the state of developed turbulent flow represented by points of Φ of the phase space.

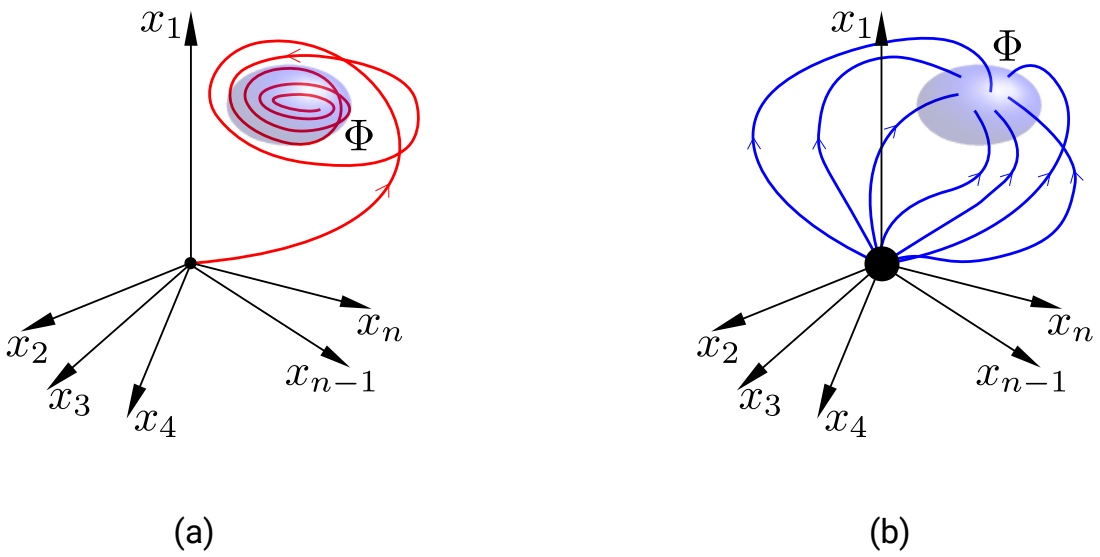

Figure 4.1: The sketches show system's trajectories of the long-term run *(a)* and the series of short-term runs *(b)* in the phase space. Axes x_i, $i = 1, \ldots, n$ represent the generalized coordinates and indicate that this space is multidimensional. The arrows of the trajectories denote directions of transitions from initial states to the state of developed turbulent flow. All the runs shown have the same parameters and the boundary conditions but different perturbed initial conditions. Subdomain Φ of the phase space consists of points which correspond to the state of developed turbulent flow.

Both figures, 4.1(a) and 4.1(b), can be used for illustrating the two approaches described in subsections 4.1.2 and 4.1.3. In the case of the time averaging done by (4.10), data to be averaged are generated in the long-term run shown in figure

4.1(a) when the flow has the state of developed turbulent flow, which belongs to the subdomain Φ. For computing statistical means, which are defined similar to the simplest case given by (4.12) and (4.13), data obtained at the final states of the series of the short-term runs shown in figure 4.1(b) are used (their final states also belong to Φ). The averaging is done over all the runs of the series (the ensemble), and this type of averaging is referred to as the ensemble averaging.

As it is mentioned above in section 4.1.2, the method of the averaging over time or space is more convenient from a practical point of view and is applied commonly to obtain data during one single experiment (or a run) but has the disadvantages. In contrast, probability means related to the averaging over an ensemble are more suitable for theoretical investigations but hardly applicable in practice. For simple dynamic systems, it is possible to prove strictly that both methods give identical results (see references to the corresponding literature in [57]). In a general case, an "ergodic" hypothesis is introduced. It states that the averaging over time or space converges to the averaging over an ensemble, if the time or space interval for averaging is large enough (see [57]).

4.1.5 Problem of the ergodicity

The following general question, which is important in the theory of turbulence and which gives the motivation for performing this study, can be formulated: are the time-averaged data identical to results obtained by averaging over an ensemble?

In this work the comparison of both procedures of averaging is done on the base of data obtained by means of three-dimensional direct numerical simulations of turbulent Rayleigh-Bénard convection in a closed extended rectangular box. The main goal is to find similarities and differences (if any) between quantities averaged over time (section (4.1.2)) and those averaged over an ensemble (section 4.1.3). Time-averaged data are obtained during a long-term run, which is more convenient in practice while studying turbulence. Data averaged over an ensemble are obtained from short-term runs which are almost identical (up to uncontrollable infinitesimal disturbances of initial conditions). Averaging over space coordinates, which is not studied in this work, is applied only to reduce time-averaged or ensemble-averaged three-dimensional data to one-dimensional profiles (by averaging over area) or to ordinary values (by averaging over volume). Eventually, reduced data are analysed.

The numerical experiments for generating data used for averaging by the two approaches are schematically shown in figures 4.1(a) and 4.1(b): figure (a)

shows the trajectory of the long-term run in the phase space (the case of the time averaging); figure (b) shows the trajectories of the ensemble of short-term runs in the phase space (the ensemble averaging). The code applied for performing direct numerical simulations of turbulent convection flows is described above in chapter 3. The description of the problem, parameters of all runs, and the discussion of analysis and results are given below in the next sections of the current chapter.

4.2 Description of problem

4.2.1 General requirements of numerical experiments

The governing equations (1.11)-(1.13) are solved numerically for a flow in a rectangular box schematically shown in figure 1.1(b) for the case of $L = W$. To study the problem of the ergodic hypothesis, one long-term run and an ensemble of short-term runs were performed. The total number of the short-term runs of the ensemble is 101. The total duration of the long-term run starting from some perturbed initial conditions amounts to $3351.05\,T_f$. The time of simulation of the short-term runs is discussed in section 4.3.2

While performing numerical simulations, the following requirements were satisfied for all runs:

1. The control parameters Ra, Pr, Γ are the same (section 4.2.2).
2. The standard boundary conditions are the same (section 1.2).
3. Initial conditions have small differences with respect to each other (section 4.2.4).
4. Duration of each run of the ensemble is fixed (section 4.3.2).
5. Settings of the solvers of the elliptic equations are the same (section 4.2.5).

As the consequence of the first requirement, the chosen grid resolution also does not change for all runs (see below in section 4.2.3). As it can be seen, only initial conditions of all runs are different according to the third requirement.

4.2.2 Control parameters

All runs were performed with the same control parameters which are introduced in section 1.1. The Rayleigh number Ra and the Prandtl number Pr defined in

(1.16) and (1.17), respectively, and included in the governing equations (1.11)-(1.13) were the following:

$$Ra = 10^5, \qquad Pr = 0.7. \tag{4.15}$$

In addition, the following aspect ratio of the rectangular box was used in all DNS:

$$\Gamma = 25. \tag{4.16}$$

The choice of the moderate Rayleigh number is dictated by the total number of runs, their duration, and the large aspect ratio of the cell, which make computational costs high. Nevertheless, the chosen Rayleigh number leads to a turbulent convection flow and corresponds to the soft convective turbulence introduced first in work [59], which describes several states of turbulence observed in a convection flow of gaseous helium in a cylindrical cell of $\Gamma = 1$. Particularly, it was found that the chaotic state, which occurs up to $Ra = 2.5 \times 10^5$, corresponds to the state of a convection flow when the time coherence is lost, but the coherent structure remains (see [59; 60]). In this regard, the persistent space coherence can show a qualitative difference of the two approaches, which is discussed in more details below in subsection 4.3.3.

It should be noted that the temperature is normalized in the current code for DNS of a convection flow as

$$T = \frac{\tilde{T} - \tilde{T}_{mid}}{\tilde{T}_1 - \tilde{T}_2}, \tag{4.17}$$

where $\tilde{T}_1$ and $\tilde{T}_2$ are the temperatures of the heated bottom and cooled top plates shown in figure 1.1(b), and $\tilde{T}_{mid} = (\tilde{T}_1 + \tilde{T}_2)/2$. The coordinate $z \in [-0.5, 0.5]$. Thus, $T(-0.5) = 0.5$ at the bottom plate, and $T(0.5) = -0.5$ at the top plate.

4.2.3 Grid resolution

All the boundaries of a closed rectangular cell has rigid walls, and corresponding boundary layers form in the vicinity of them: the viscous boundary layers at all the walls; the thermal boundary layers at the horizontal plates. Thus, to avoid excessive number of nodes in the bulk of the cell and to properly resolve the boundary layers, the applied grid is non-uniform in all directions.

The following procedure is applied for generating grids for convection problems in extended rectangular boxes, $\Gamma > 1$ (the length and the width of the cell are equal). According to the reference units given by (1.6), in dimensionless units the

N_x	N_y	N_z	$n_h^{(BL)}$	$n_v^{(BL)}$	Δh_u
1209	1209	64	11	12	2.1^{-2}

Table 4.1: Parameters of the grid: N_x, N_y, N_z are the numbers of nodes along x, y, z, respectively; $n_h^{(BL)}$, $n_v^{(BL)}$ the numbers of space intervals within the boundary layers near the horizontal and vertical walls, respectively; Δh_u the space interval of the uniform part of the distributions in the horizontal directions x, y.

height of the cell is $H = 1$, and the horizontal dimensions are $L = W = \Gamma$. In the vertical direction z the distribution of nodes is clustered near the horizontal plates and is generated by using any analytical formula, particularly Gauss-Lobatto points. In the horizontal direction x the distribution is also clustered near lateral walls but only in the intervals $[0, 0.5]$ and $[\Gamma - 0.5, \Gamma]$ (it is assumed that $x \in [0, \Gamma]$. Thus, the distribution of nodes in the x direction in the middle part in uniform (i.e. $x \in [0.5, \Gamma - 0.5]$). The distribution of nodes in the y direction is exactly the same as in the x direction.

In the case of Gauss-Lobatto points, the number of nodes within the boundary layers increases significantly as long as the total number of nodes of the distribution grows. To avoid the excessive number of nodes within the boundary layers, distributions of Gauss-Lobatto points are blended by uniform distributions added with some weighting coefficients:

$$p_i = w\, p_i^{(GL)} + (1 - w)\, p_i^{(U)}, \tag{4.18}$$

where w is a weighting coefficient, $0 < w < 1$, p_i the coordinate of the ith node along a direction, $p_i^{(GL)}$ the coordinate of the pure Gauss-Lobatto node, $p_i^{(U)}$ the coordinate of the node of the uniform distribution (see e.g. [47]).

For the control parameters given by (4.15) and (4.16), the the sizes of the applied grid are $1209 \times 1209 \times 65$ (the numbers of nodes). Some parameters of the grid are given in table 4.1. The space intervals of the applied grid are shown in figures 4.2(a) for the distribution of nodes in the x direction and 4.2(b) in the z direction.

4.2.4 Initial conditions

Initial conditions of every run mentioned above in subsection 4.2.1 are represented by decomposition of a fixed base part and imposed random noise. As for

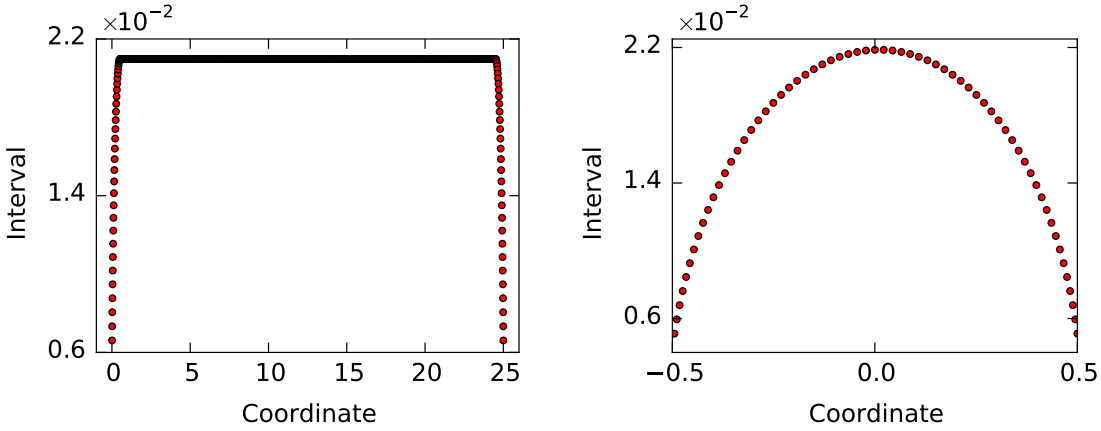

(a) (b)

Figure 4.2: Space intervals between neighbour nodes. Figure (a): in the horizontal directions x. Figure (b): in the vertical directions z. Both horizontal directions, x and y, have the same distribution of nodes.

the base part, the velocity is zero,

$$\boldsymbol{u} = 0, \tag{4.19}$$

and the temperature has the linear profile,

$$T = -z \tag{4.20}$$

where the conversion given by (4.17) is taken into account.

The base initial conditions given by (4.19) and (4.20) are perturbed by a random field which serves as uncontrollable small disturbances occurred in experiments. Values of random fields are in the range $(-1, 1)$ for the velocity components and $(0, 1)$ for the temperature, which are additionally multiplied by some constant (or amplitude). The variety of different initial conditions is achieved by different unique random fields and different combinations of the quantities u_x, u_y, u_z, and T to be perturbed. For example, the parameter u_x can be perturbed, while the other quantities are set according to the base conditions given by (4.19) and (4.20). Another variant is the perturbation of the parameters u_x and u_y, when the rest parameters are not perturbed, and so on. The permutation of the parameters being perturbed can give up to 15 different combinations of parameters being perturbed by different random fields. Moreover, each parameter can be perturbed by imposing a random field multiplied by a constant (an amplitude), which also varies.

Thus, one can obtain multiple realizations of the flow with the same control parameters and the same boundary conditions but different initial conditions by following the above strategy. In this case, each realization of the flow has a unique trajectory in the phase space illustrated in figure 4.1(b).

4.2.5 Parameters of multigrid solvers

The numerical method, which is described above in chapter 3 and which is based on the two multigrid solvers of the Hypre package, SMG and PFMG, is applied for solving the Poisson equation for the pressure (3.6) and the Helmholtz equation for the temperature (3.15). Both elliptic partial differential equations have the different matrices obtained after the discretization of the corresponding equations together with their boundary conditions. This means that two multigrid solvers are simultaneously created for solving both elliptic equations, exist while performing numerical simulations, and require different settings. Both multigrid solvers of Hypre are iterative, and the main parameter to be set is their tolerance used as the stopping criterion.

As for the temperature, which is directly computed from equation (3.15), the tolerance of an applied solver is connected directly with the error of the obtained solution. In the current work, the tolerance $\sim 10^{-6}$ was set for solving numerically the Helmholtz equation for the temperature.

In the case of the Poisson equation for the pressure, the obtained solution is used for correcting the velocity and velocity fluxes introduced above in section 3.2. The main criterion of a proper solution is the fulfilment of the incompressibility condition given by (1.11) and computed by approximation (3.9) with using fluxes. Only one problem is that the tolerance required to obtain a given level of the divergence of the velocity found by using (3.35) depends on the time step Δt used for the time-discretization done by (3.5). This partly can be explained by the fact that the best known choice of an initial guess required by all iterative methods for the iterative process is the solution obtained on the previous moment of time. As long as the time step increases, a flow changes more significantly between two sequential moments of time. Thus, the tolerance of the solver for the pressure equation should be chosen carefully to satisfy the condition of an incompressible flow. In this work, the level of the divergence of the velocity was in the range

$$5 \times 10^{-6} < \sup_{\Omega} |\operatorname{div} \boldsymbol{u}| < 1 \times 10^{-5}, \tag{4.21}$$

where $\operatorname{div} \boldsymbol{u}$ is computed by applying (3.9).

4.3 Results and analysis

4.3.1 General procedures of averaging

The procedures of averaging over time, $\langle * \rangle_t$, and averaging over ensemble, $\langle * \rangle_e$, are technically identical. When the type of averaging is not important, an averaged quantity is denoted by the bar, $\overline{*}$.

Sets of three-dimensional fields of the velocity components and of the temperature (or so-called snapshots) are sequentially written after the same interval of time, $5\,T_f$, during the long-term run (corresponding time intervals are discussed below in section 4.3.2). The written snapshots of 3D fields are used then to obtain time-averaged 3D fields. Because snapshots are written after the same time interval, the time averaging can be done simply by computing arithmetic mean. For example, a field $f(x, y, z, t)$ is averaged over time as

$$\langle f \rangle_t = \langle f(x, y, z) \rangle_t = \frac{f(x, y, z, t_1) + \cdots + f(x, y, z, t_N)}{N}, \tag{4.22}$$

where t_i, $i = 1, \ldots, N$, are moments of time when fields are written (the time step is $5\,T_f$). The initial moment of time when snapshots are taken for averaging as well as the number of snapshots applied for averaging are discussed below in section 4.3.2.

In the case of averaging over an ensemble, all short-term runs of the ensemble are performed for the same interval of time, and at the end of this time interval a snapshot of 3D fields of every run is written out. Thus, the number of generated snapshots is equal to the number of short-term runs of the ensemble. These snapshots are used for computing ensemble-averaged fields, and the ensemble averaging is done by arithmetic mean similar to the time averaging. For example, a field $f(x, y, z, t_0)$ is averaged over an ensemble as

$$\langle f \rangle_e = \langle f(x, y, z) \rangle_e = \frac{f^{(1)}(x, y, z, t_0) + \cdots + f^{(M)}(x, y, z, t_0)}{M}, \tag{4.23}$$

where the upper indices are used to distinguish fields of different short-term runs, M is the number of these runs, t_0 is the moment of time when the short-term runs are finished and the snapshots are written.

To reduce the complexity of large 3D fields to be compared, vertical area-averaged profiles of corresponding quantities denoted by $\langle * \rangle_A$ are analysed in most cases. An area-averaged profile is obtained by extracting data from 3D fields at a fixed coordinate z (between the top and bottom plates of the cell) and by averaging

the extracted data over area of a square which is formed by the intersection of the horizontal plane at the given coordinate z and the rectangular box and has the sizes 25×25 (according to the aspect ratio $\Gamma = 25$). The averaging is done at all fixed z between the two horizontal plates resulting in the vertical area-averaged profile. In some cases averaging is done over smaller area of some part of the square cross section, but this is emphasized. To compare two area-averaged profiles, $f(z)$ and $g(z)$, the relative difference defined by equation (2.61) is applied. In this chapter the norm of any function $f = f(z)$ of one argument, which is included in the equation of the relative difference, is computed by using the supremum, and the final equation for δr is as follows:

$$\delta r = \frac{\sup\limits_{z}|f - g|}{\sup\limits_{z}|f|}\,. \tag{4.24}$$

where z belongs to the interval between the horizontal plates of a convection cell.

In addition, an area-averaged profile can be integrated over the coordinate z and divided by $H = 1$. The obtained valued is called the volume averaged quantity (or the volume average) and is denoted by $\langle * \rangle_V$.

The abbreviation "L.R." and "E." used in the legend in many figures of this chapter mean data which were obtained in the long-term run (L.R.) and in the short-term runs of the ensemble (E.).

4.3.2 Duration of runs and first results

As it is mentioned in section 4.2.1, the duration of the long-term run is $3351.05\,T_f$. The required time of simulation of the 101 short-term runs of the ensemble starting from an initial state until the state of developed turbulent flow was initially estimated by analysing distributions of an instantaneous volume averaged Nusselt number $Nu'_V(t)$ and an instantaneous total kinetic energy $E'_{\mathrm{TKE}}(t)$ which were obtained during the long-term run. The distribution of Nu'_V is computed at different moments of time t by using the equation

$$Nu'_V(t) = \sqrt{Ra\,Pr}\,\langle u_z T \rangle_V + 1, \tag{4.25}$$

when the term $u_z T$ is averaged only over volume as opposed to Nu_V computed by (1.22). Similarly the distribution of $E'_{\mathrm{TKE}}(t)$ is computed at different moments of time as

$$E'_{\mathrm{TKE}}(t) = \frac{1}{2}\,\langle \boldsymbol{u}^2 \rangle_V, \tag{4.26}$$

when $\boldsymbol{u}^2$ is also averaged only over volume as opposed to E_{TKE} computed by (1.26). The obtained possible simulation time of short-term runs turned out to be approximately $55\,T_f$. The plots of $Nu'_V(t)$ and $E'_{\mathrm{TKE}}(t)$ of 30 short-term runs of the ensemble are shown in figures 4.3(a) and 4.3(b), respectively.

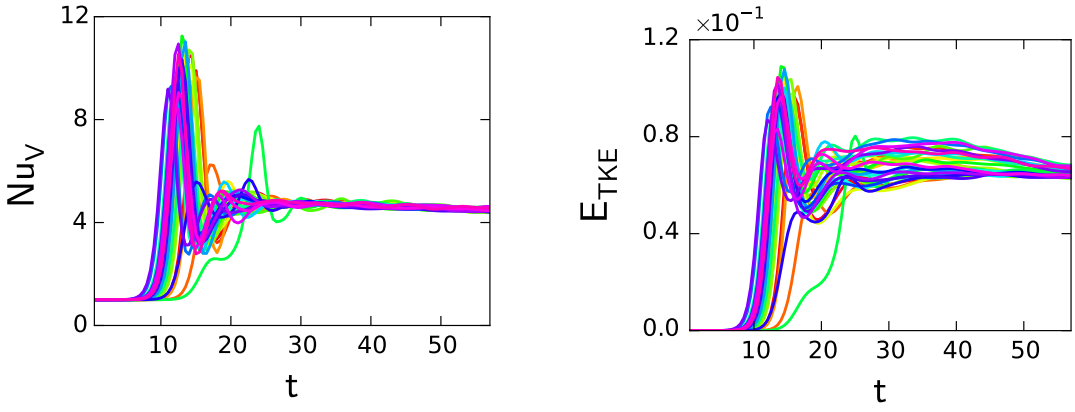

(a) (b)

Figure 4.3: The distributions of the instantaneous quantities with respect to time (in units of T_f) of 30 short-term runs: (a) the instantaneous volume averaged Nusselt number Nu'_V; (b) the instantaneous total kinetic energy E'_{TKE}.

Nevertheless, more accurate analysis of an instantaneous root mean square velocity u'_{rms} defined by

$$u'_{rms} = \sqrt{\langle \boldsymbol{u}^2 \rangle_V} \tag{4.27}$$

reveals that the velocity u'_{rms} levels off much slower than it can be found by studying plots of Nu'_v and E'_{TKE}. It can be seen that values of $u'_{rms}(t)$ shown in figure 4.4(a) stop to decrease after $t_A = 171.14\,T_f$, which is much greater than the initial estimation $55\,T_f$. Thus, the duration of all the short-term runs amounts to $171.14\,T_f$. At this moment of time, $t_A = 171.14\,T_f$, data used for the ensemble averaging were obtained. Values of u'_{rms}, Nu'_V and E'_{TKE} obtained at $t_A = 171.14\,T_f$ in the short-term runs of the ensemble are shown in figures 4.4(b), 4.5(a), 4.5(b), respectively (the black solid lines represent the mean values).

The detailed information on the duration of the runs and the parameters of the averaging can be found in table 4.2. The preliminary results such as the root mean square velocity u_{rms}, the Reynolds number Re, and the volume averaged Nusselt number Nu_V are provided in table 4.3.

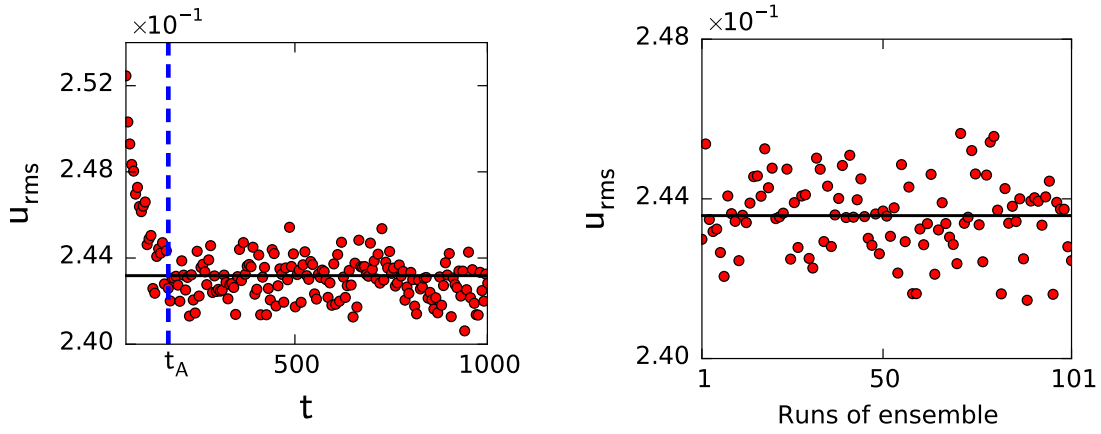

(a) (b)

Figure 4.4: The instantaneous root mean square velocity u'_{rms} computed by (4.27) and the root mean square velocity u_{rms} computed by (1.25) and represented by the horizontal black solid line: (a) the distribution $u'_{rms}(t)$ obtained in the long-term run, the vertical blue dashed line $t_A = 171.14\,T_f$ indicates the moment when $u'_{rms}(t)$ stops to decrease and only fluctuates near $u_{rms} = 0.24$ (averaging over $3170\,T_f$ after $t = t_A$); (b) values of u'_{rms} at $t_A = 171.14\,T_f$ obtained in the 101 short-term runs of the ensemble, $u_{rms} = 0.24$ (averaging over the ensemble).

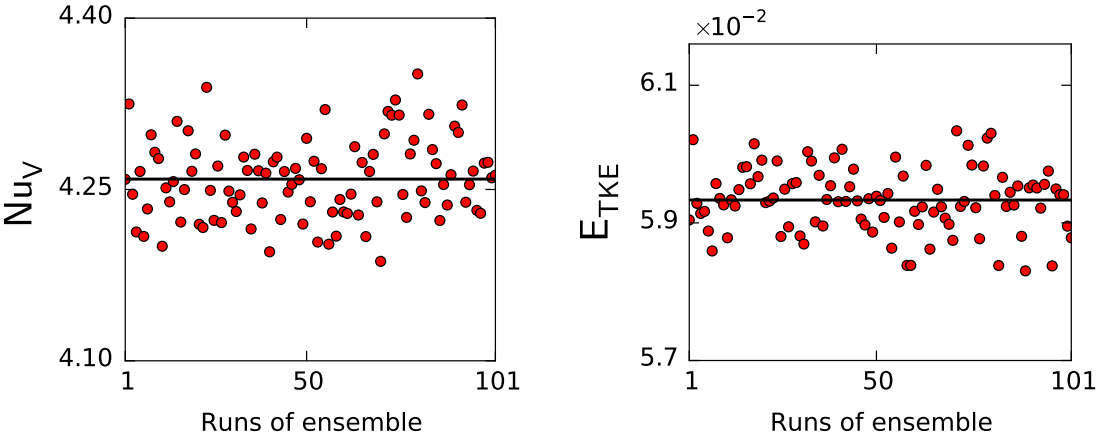

(a) (b)

Figure 4.5: The instantaneous volume averaged Nusselt number Nu'_V (a) and the instantaneous total kinetic energy E'_{TKE} (b) obtained in the 101 short-term runs of the ensemble at the moment of time $t_A = 171.14\,T_f$. The horizontal black solid lines shown in both figures represent the ensemble-averaged quantities: $\langle Nu'_V \rangle_e = 4.26$; $\langle E'_{\mathrm{TKE}} \rangle_e = 5.93 \times 10^{-2}$.

	t_{sim}, T_f	t_{aver}, T_f	N_{snap}
Long-term run	3351.05	3170	635
Short-term run	171.14	N/A	101

Table 4.2: The duration and the parameters of averaging of the runs: t_{sim} is the duration of runs of both types (in units of T_f); t_{aver} the time during which snapshots of the long-term run were written and used for averaging over time (in T_f, the interval of writing is $5\,T_f$); N_{snap} the number of snapshots used for averaging over time and over ensemble.

	u_{rms}	Re	Nu_V
Long-term run	0.24 (9.43×10^{-4})	91.88 (3.56×10^{-1})	4.26 (3.33×10^{-2})
Short-term run	0.24 (9.41×10^{-4})	92.07 (3.56×10^{-1})	4.26 (3.50×10^{-2})

Table 4.3: The preliminary results obtained in the long-term run and in the short-term runs of the ensemble: u_{rms} is the root mean square velocity defined by (1.25); Re the Reynolds number defined by (1.24); Nu_V the volume averaged Nusselt number defined by (1.22). The standard deviation of each quantity is given in brackets.

4.3.3 Analysis of planar cuts

The qualitative comparison which shows the difference is done by studying planar cuts of three-dimensional fields of the vertical velocity component u_z and the temperature T in a horizontal plane which is fixed at the middle of the box with $z = 0$ (a so-called midplane). The 3D fields are averaged over time and over the ensemble by applying the procedures given by (4.22) and (4.23). Throughout the present work planar cuts considered in any horizontal plane (including the midplane) are also called two-dimensional fields (the vertical coordinate is fixed).

Contour plots of instantaneous two-dimensional fields of u_z and T are considered first before discussing the averaged fields. Figures 4.6(a) and 4.6(c) are obtained from instantaneous data of the long-term run, and figures 4.6(b) and 4.6(d) are obtained from instantaneous fields of one short-term run of the ensemble. Irregular fluctuations of the fields seen in the figures reveal the turbulent regime and confirm what is discussed above in section 4.2.2. The fields of the velocity component u_z shown in figures 4.6(a) and 4.6(b), and the fields of the temperature T shown in 4.6(c) and 4.6(d) have the same colour bars. Despite chaotic irregular structures of the flows, the contour plots in figure 4.6 do not demonstrate any significant differences, as it can be expected.

Nevertheless, the averaged two-dimensional fields of u_z shown in figures 4.7(a) and 4.7(b), and those of T in figures 4.7(c) and 4.7(d) reveal some differences. At first, the patterns of the time-averaged flow shown in figures 4.7(a) and 4.7(c)

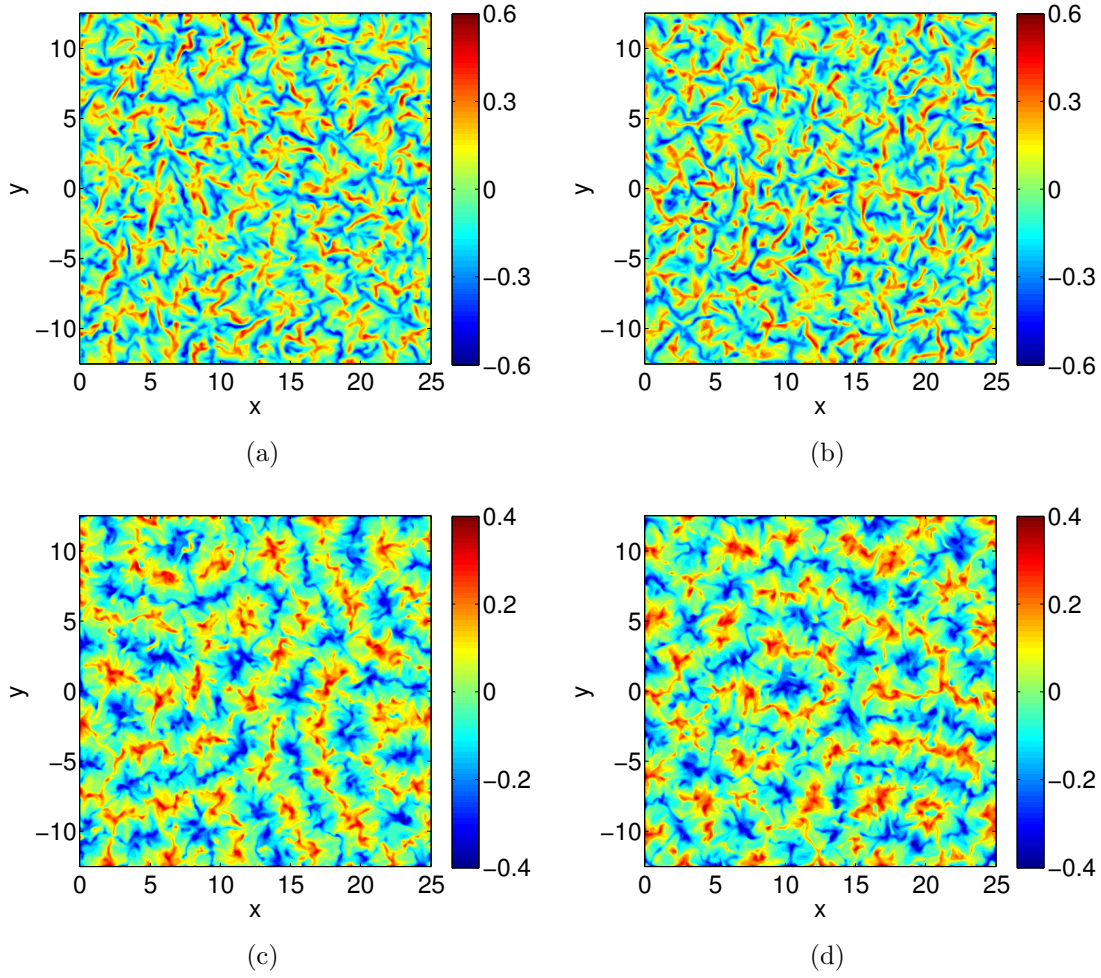

Figure 4.6: Contours of 2D instantaneous fields of the velocity component u_z shown in figures (a) and (b) (top row), and the temperature T in figures (c) and (d) (bottom row). All the 2D fields are taken at the horizontal midplane extracted from 3D data ($z = 0$). Figures on the left-hand side, (a) and (c), are obtained from data of the long-term run. Figures on the right-hand side, (b) and (d), are obtained from data of one short-term run of the ensemble.

have more coherent structures as opposed to the case of the flow averaged over the ensemble shown in figures 4.7(b) and 4.7(d). In other words, the averaging over the ensemble tends to destroy large coherent structures, while the time averaging tends to preserve such structures. Both types of averaging eliminate irregular fluctuations, which change rapidly in time and in space, as it can be seen by comparing the averaged fields shown in figure 4.7 with the instantaneous fields in figure 4.6: in the latter case the average level of the amplitudes of the quantities is larger by approximately one order of magnitude (for both u_z and T).

Secondly, quantitative difference can be found by considering the plots in figure 4.7 taking into account that all the contour plots of the figure have the

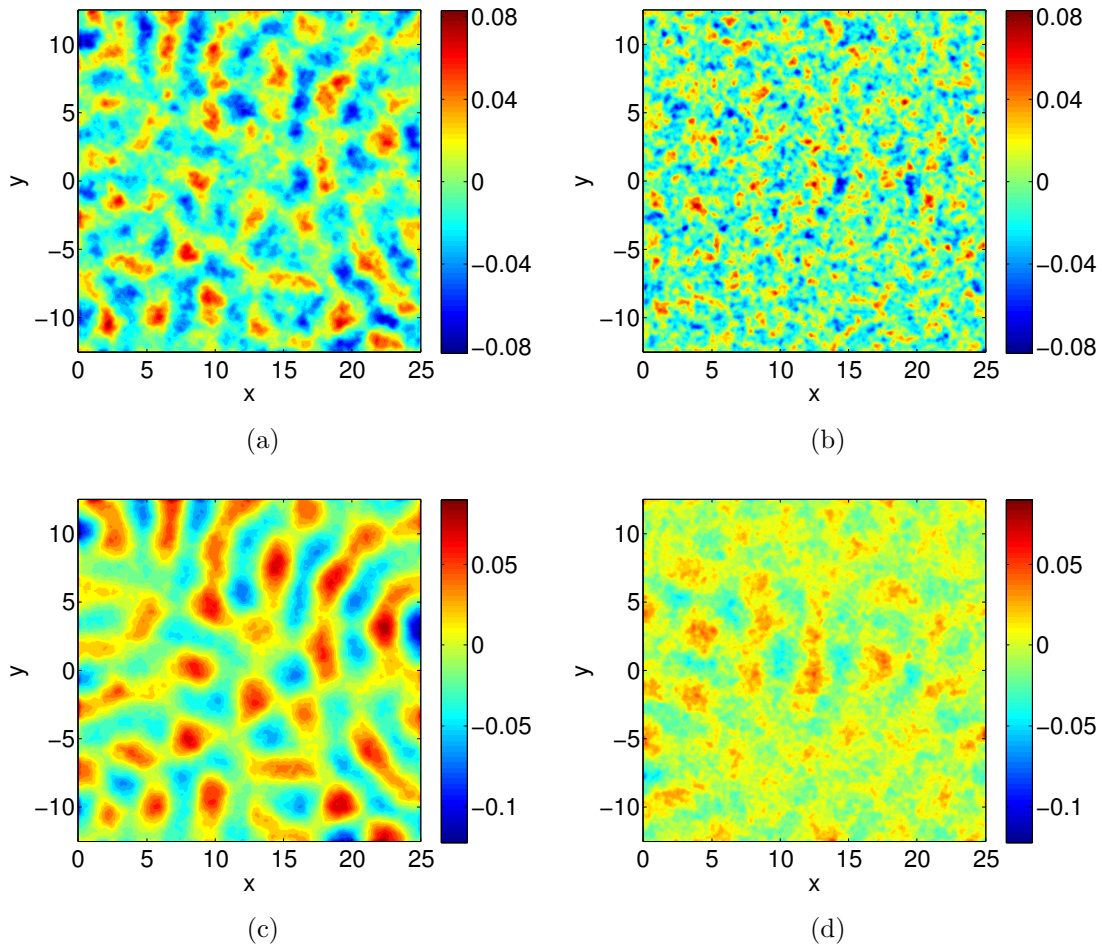

Figure 4.7: Contours of 2D averaged fields of the velocity component u_z shown in figures (a) and (b) (top row) and the temperature T in figures (c) and (d) (bottom row). All 2D fields applied for averaging are taken at the horizontal midplane extracted from 3D data ($z = 0$). Figures (a) and (c): the time-averaged fields. Figures (b) and (d): the fields averaged over the ensemble. The parameters used for averaging are given in table 4.2.

same range of the color bar. It can be seen that the average level of the amplitude is approximately the same in the case of the velocity component u_z (figures 4.7(a) and 4.7(b)) but much smaller in the case of the temperature T (figures 4.7(c) and 4.7(d)). To estimate the levels of the amplitudes and to make quantitative comparison, the area average of the 2D fields of both u_z and T is computed by using the equation

$$\langle |f| \rangle_A = \frac{1}{S} \int_s |f| \, \mathrm{d}S, \tag{4.28}$$

where S is the area of the square cross section of the box. Further, $f = f(x, y)$ is the 2D field of u_z or T, and the absolute value of f is used for integrating

due to different signs of both quantities depending on a point (x, y) of the cross section. The obtained values of the averages of u_z and T computed by (4.28) are given in table 4.4, which shows that the averaging over the ensemble in the case of u_z makes the averaged field smaller in amplitude (the corresponding relative difference is $\delta r = 17.93\,\%$) than it is in the case of T (the relative difference is $54.95\,\%$). In addition, the maximum and the minimum (i.e. the range) of each 2D averaged field are also given in table 4.4: the ranges of both types of averaging in the case of u_z are almost the same, while in the case of T the range of the time-averaged field is much wider than the one of the ensemble-averaged field.

	Velocity component u_z		Temperature T	
	Average	Range, $\times 10^{-2}$	Average	Range, $\times 10^{-2}$
Time averaging	$1.84 \cdot 10^{-2}$	$(-7.57, 8.27)$	$2.35 \cdot 10^{-2}$	$(-12.11, 8.99)$
Ensemble averaging	$1.51 \cdot 10^{-2}$	$(-7.56, 8.02)$	$1.06 \cdot 10^{-2}$	$(-6.41, 5.98)$

Table 4.4: The table of the area averages of the 2D fields of u_z and T computed by 4.28. The 2D fields are planar horizontal cuts extracted from the corresponding 3D fields (averaged over time or over the ensemble) at the midplane ($z = 0$). The columns "range" contains intervals between the minimum and the maximum of a corresponding 2D field. The relative differences δr between the area averages of the time-averaged 2D fields and the ensemble-averaged 2D fields: $17.92\,\%$ for u_z; $54.95\,\%$ for T.

Both qualitative and quantitative differences discussed just above in the current subsection can be confirmed by considering horizontal profiles of u_z and T extracted from the corresponding 2D fields. Such profiles are shown in figure 4.8: (a) and (b) for the velocity component u_z; (c) and (d) for the temperature T. All the horizontal profiles are extracted at the fixed y at the center of the midplane. One can note that large structures are less prominent in the case of the ensemble averaging (figures 4.8(b) and 4.8(d)) than those in the case of the time averaging (figures 4.8(a) and 4.8(c)). Moreover, the decrease of the level of the amplitude of T can be seen by comparing figures 4.8(c) and 4.8(c), while in the case of u_z it is not found (see figures 4.8(a) and 4.8(b)).

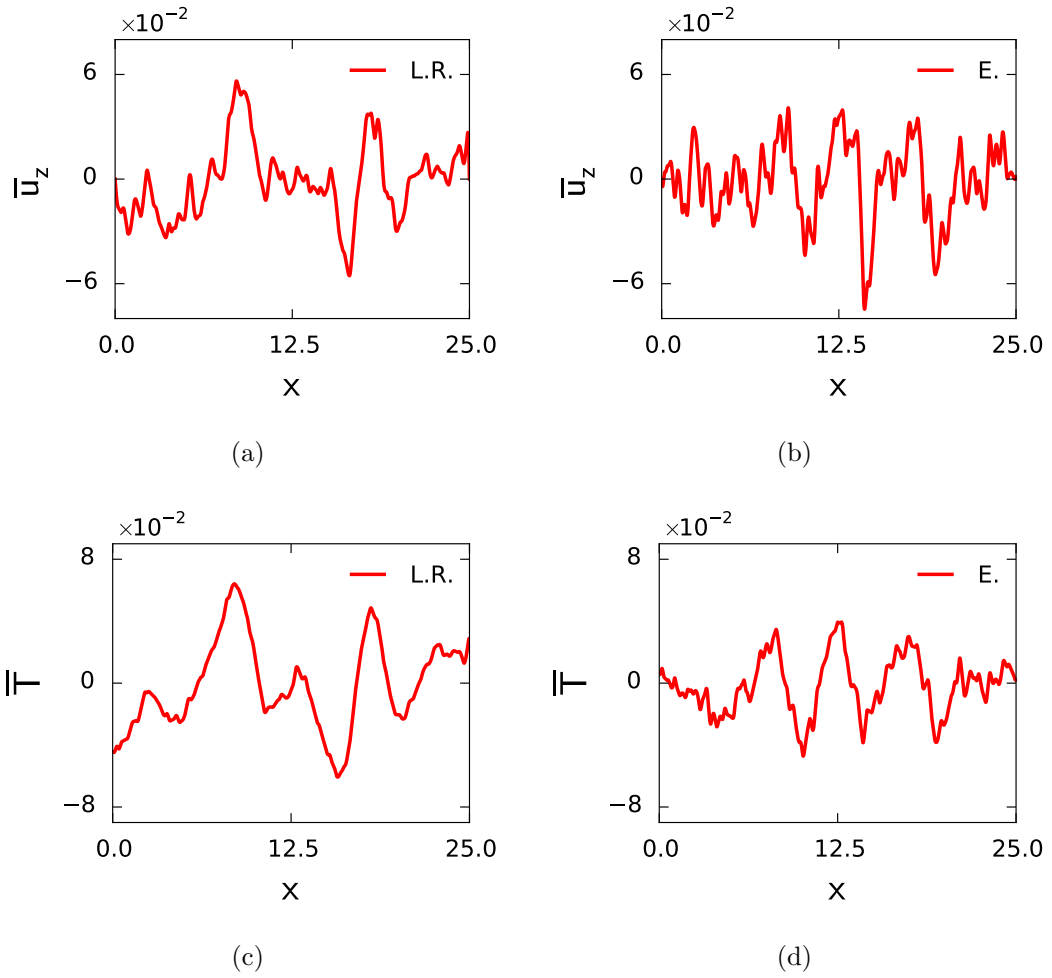

Figure 4.8: The horizontal profiles of the quantities: the velocity component u_u is shown in figures (a) and (b); the temperature T is shown in figures (c) and (d). The profiles are extracted at the horizontal midplane ($z = 0$) and at the fixed y which corresponds to the center of the plane. The time-averaged data are shown in figures (a), (c). The data averaged over the ensemble are in figures (b), (d).

4.3.4 Nusselt number and mean temperature

The next step of the analysis is to compare the second key response of the system which is the heat transfer measured by the Nusselt number Nu. The obtained profiles computed by equation (1.21) are shown in figure 4.9(a). Again, both vertical profiles of Nu are almost identical, and both have almost the same shape (see table 4.5). In actual fact, the profiles should be straight lines, but every numerical simulation will find some small deviations.

Small difference is also found in the vertical profiles of the mean temperature $\overline{T}$ shown in figure 4.9(b): the averaging is done over time (the blue solid curves) and over the ensemble (the red dashed curves). In this case, the profiles of the mean temperature demonstrate the behaviour consistent with predictions of the theory. The corresponding relative difference is given in table 4.5.

Thus, both mean global quantities, Nu and $\overline{T}$, agree well, and the similarity of their profiles can confirm that the number of short-term runs is quite enough for the analysis.

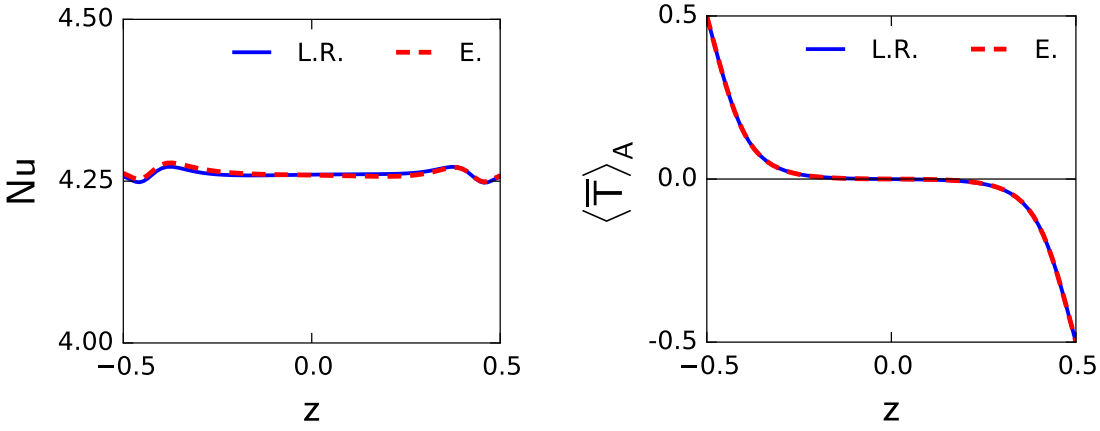

(a) (b)

Figure 4.9: The area-averaged profiles of the quantities: (a) the Nusselt number Nu; (b) the mean temperature $\overline{T}$. The profiles are obtained from data averaged over time (the blue solid curves) and averaged over the ensemble (the red dashed curves).

	Nusselt number Nu	Mean temperature $\overline{T}$
δr, %	0.15	0.16

Table 4.5: The relative difference δr computed by equation (4.24) for the area-averaged profiles of the Nusselt number Nu and of the mean temperature $\overline{T}$. The comparison is done between the time-averaged and the ensemble-averaged data.

4.3.5 Moments of the second order

In this part of the analysis, the second-order ordinary and central moments of the one-point type are compared (see e.g. [57]). After computing the moments at every point, obtained 3D fields are reduced to vertical area-averaged profiles introduced above in section 4.3.1. These profiles are used in the analysis. As usually, in all the figures the blue solid curves correspond to the time averaging, and the red dashed curves are obtained by averaging over the ensemble.

The first set of data is related to the moments of the velocity components which are computed as $\overline{u_i\, u_j}$, $i = \{x, y, z\}$, $j = \{x, y, z\}$, and the averaging, $\overline{*}$, is done over time or over the ensemble. The analysis shows that values of the obtained profiles of the moments $\overline{u_i\, u_j}$ when $i \neq j$ are smaller by 2-4 orders of magnitude than values of the profiles of the moments $\overline{u_x\, u_x}$, $\overline{u_y\, u_y}$, and $\overline{u_z\, u_z}$. Thus, the profiles of the moments $\overline{u_i\, u_j}$, $i \neq j$, are not included in the analysis. The plots of the area-averaged profiles of $\overline{u_x\, u_x}$, $\overline{u_y\, u_y}$, and $\overline{u_z\, u_z}$ are shown in figures 4.10(a), 4.10(b), and 4.10(c), respectively. The relative difference computed by equation (4.24) for every pair of the profiles is provided in table 4.6. It can be seen that the profiles are similar, but this is more prominent in the case of $\overline{u_z\, u_z}$.

Similar to the first set of the moments, the central second-order moments of the velocity components $\overline{u_i'\, u_j'}$, $i = \{x, y, z\}$, $j = \{x, y, z\}$, are compared. Again, the area-averaged profiles $\overline{u_i'\, u_j'}$, $i \neq j$, are not considered, because their values are smaller by 2-4 orders of magnitude than values of $\overline{u_x'\, u_x'}$, $\overline{u_y'\, u_y'}$, $\overline{u_z'\, u_z'}$, which are shown in figures 4.11(a), 4.11(b), 4.11(c), respectively. The relative difference between the time-averaged data and those averaged over the ensemble is provided in table 4.7. It can be seen that the type of averaging does not affect the vertical area-averaged profiles of these central second-order moments similar to the case of $\overline{u_i\, u_i}$, $i = \{x, y, z\}$, and this is especially notable for the profiles of $\overline{u_z'\, u_z'}$.

Finally, the moments $\overline{u_i\, T}$ and $\overline{u_i'\, \theta'}$, $i = \{x, y, z\}$ are considered and are shown in figure 4.12 and 4.13. Values of the profiles of $\overline{u_i\, T}$, $\overline{u_i'\, \theta'}$, when $i = \{x, y\}$ (the horizontal velocity components), are smaller by 3 orders of magnitude than values of $\overline{u_z\, T}$ and $\overline{u_z'\, \theta'}$, which are also shown in the corresponding figures, but it is not reasonable to compare with each other such small quantities. The relative difference δr computed by (4.24) and given in table 4.8 reveals that the profiles of $\overline{u_z\, T}$ and $\overline{u_z'\, \theta'}$ are unaffected by the type of averaging. The same can be said about the profiles of $\overline{\theta'\, \theta'}$ shown in figure 4.14 with the relative difference provided in table 4.8.

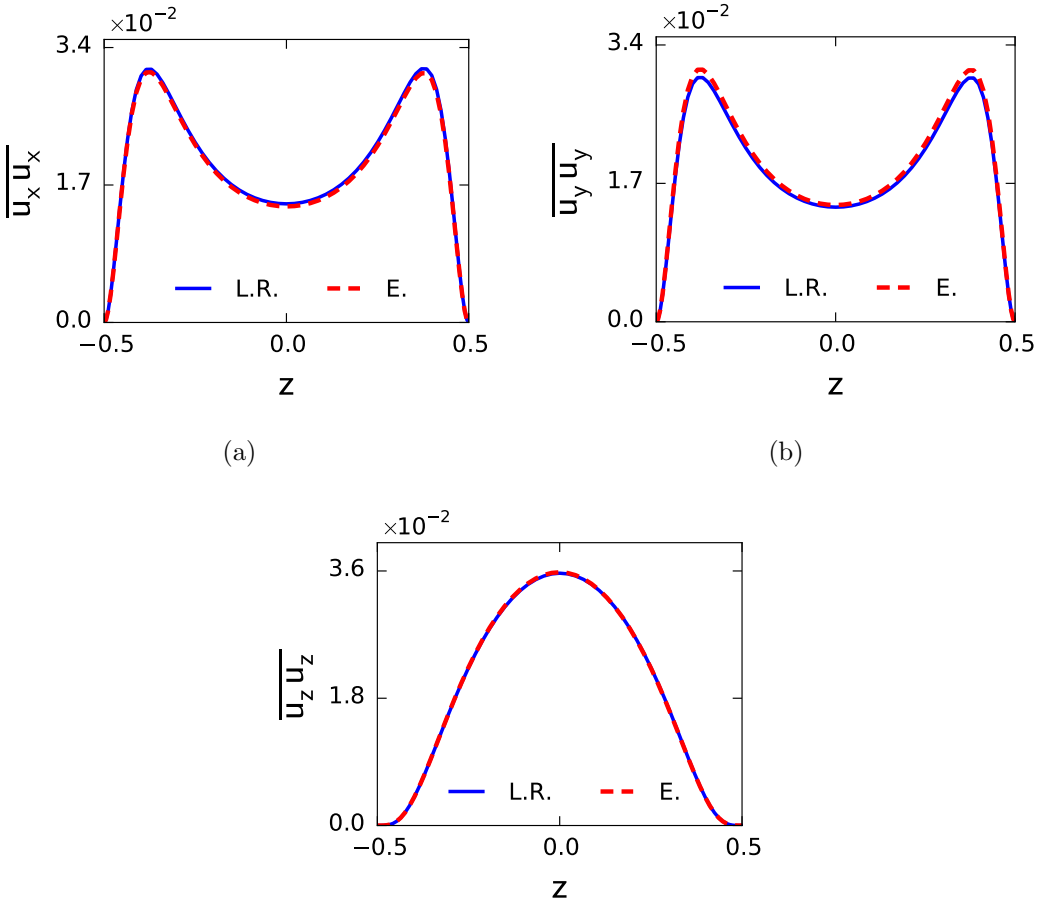

Figure 4.10: The vertical area-averaged profiles of the second-order moments (the one-point type): (a) $\overline{u_x\,u_x}$; (b) $\overline{u_y\,u_y}$; (c) $\overline{u_z\,u_z}$. The blue solid curves correspond to the time averaging. The red dashed curves correspond to the ensemble averaging.

	Profiles of $\overline{u_x\,u_x}$	Profiles of $\overline{u_y\,u_y}$	Profiles of $\overline{u_z\,u_z}$
δr, %	1.76	3.26	0.43

Table 4.6: The relative difference δr computed by equation (4.24) for the vertical area-averaged profiles of the moments $\overline{u_x\,u_x}$, $\overline{u_y\,u_y}$, $\overline{u_z\,u_z}$. The comparison is done between the time-averaged and the ensemble-averaged data.

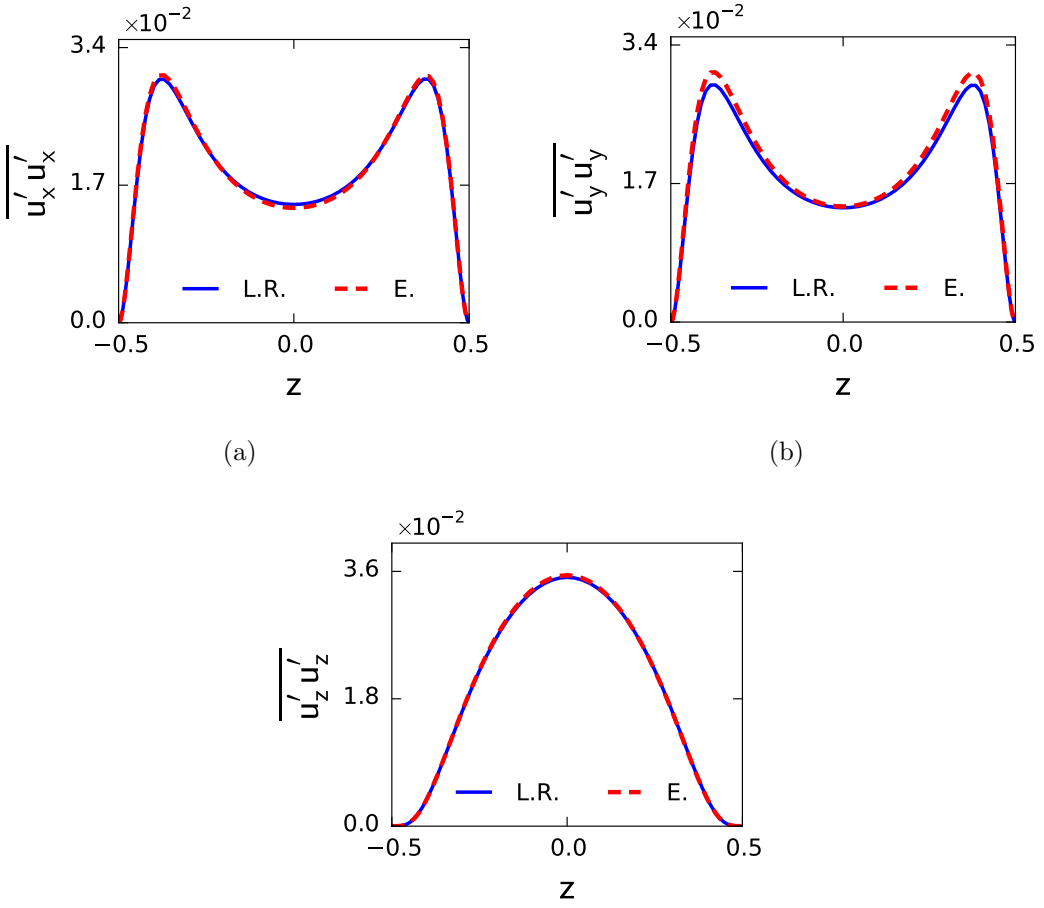

Figure 4.11: The vertical area-averaged profiles of the second-order central moments (the one-point type): (a) $\overline{u'_x\,u'_x}$; (b) $\overline{u'_y\,u'_y}$; (c) $\overline{u'_z\,u'_z}$. The blue solid curves correspond to the time averaging. The red dashed curves correspond to the ensemble averaging.

	Profiles of $\overline{u'_x\,u'_x}$	Profiles of $\overline{u'_y\,u'_y}$	Profiles of $\overline{u'_z\,u'_z}$
δr, %	1.66	5.32	0.87

Table 4.7: The relative difference δr computed by equation (4.24) for the vertical area-averaged profiles of the moments $\overline{u'_x\,u'_x}$, $\overline{u'_y\,u'_y}$, $\overline{u'_z\,u'_z}$. The comparison is done between the time-averaged and the ensemble-averaged data.

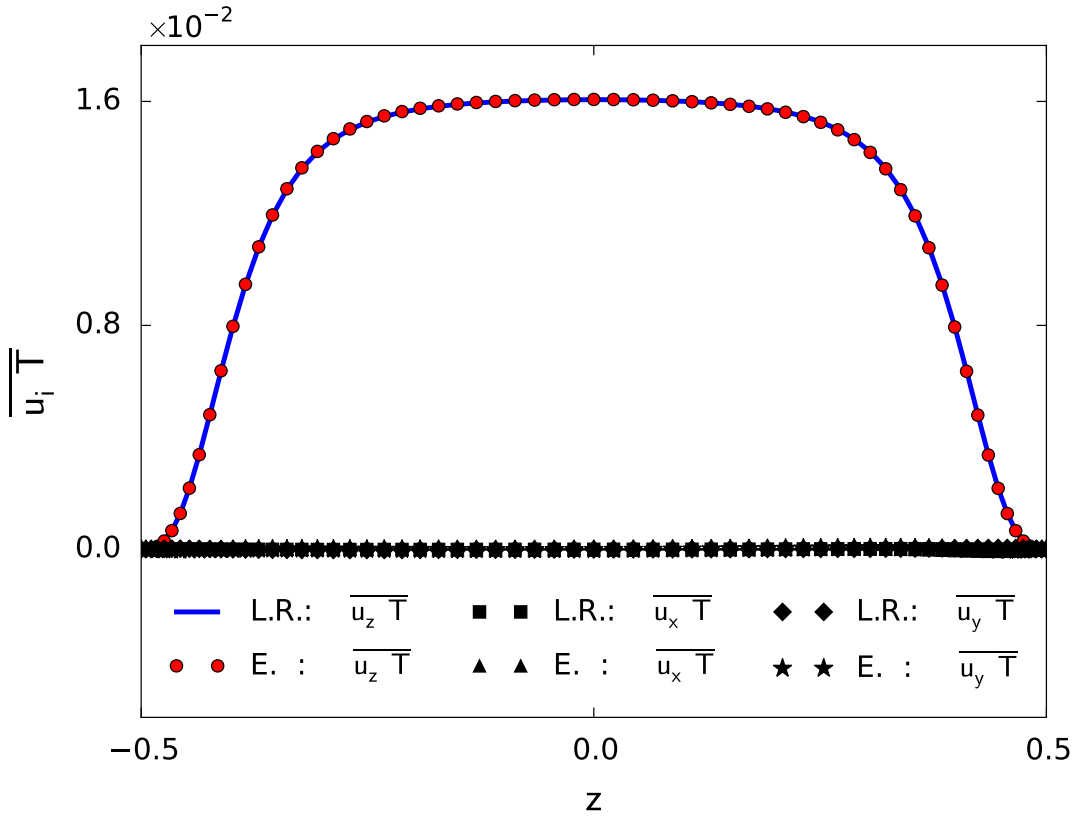

Figure 4.12: The vertical area-averaged profiles of the second-order moments $\overline{u_i\,T}$, $i = \{x, y, z\}$ (the one-point type). Values of the profiles of $\overline{u_x\,T}$ and $\overline{u_y\,T}$ obtained from both time-averaged and ensemble-averaged data are three orders of magnitude smaller than those of the profiles of $\overline{u_z\,T}$.

	Profiles of $\overline{u_z\,T}$	Profiles of $\overline{u_z'\,\theta'}$	Profiles of $\overline{\theta'\,\theta'}$
δr, %	0.15	2.61	2.69

Table 4.8: The relative difference δr computed by equation (4.24) for the vertical area-averaged profiles of the moments $\overline{u_z\,T}$, $\overline{u_z'\,\theta'}$, $\overline{\theta'\,\theta'}$. The comparison is done between the time-averaged and the ensemble-averaged data.

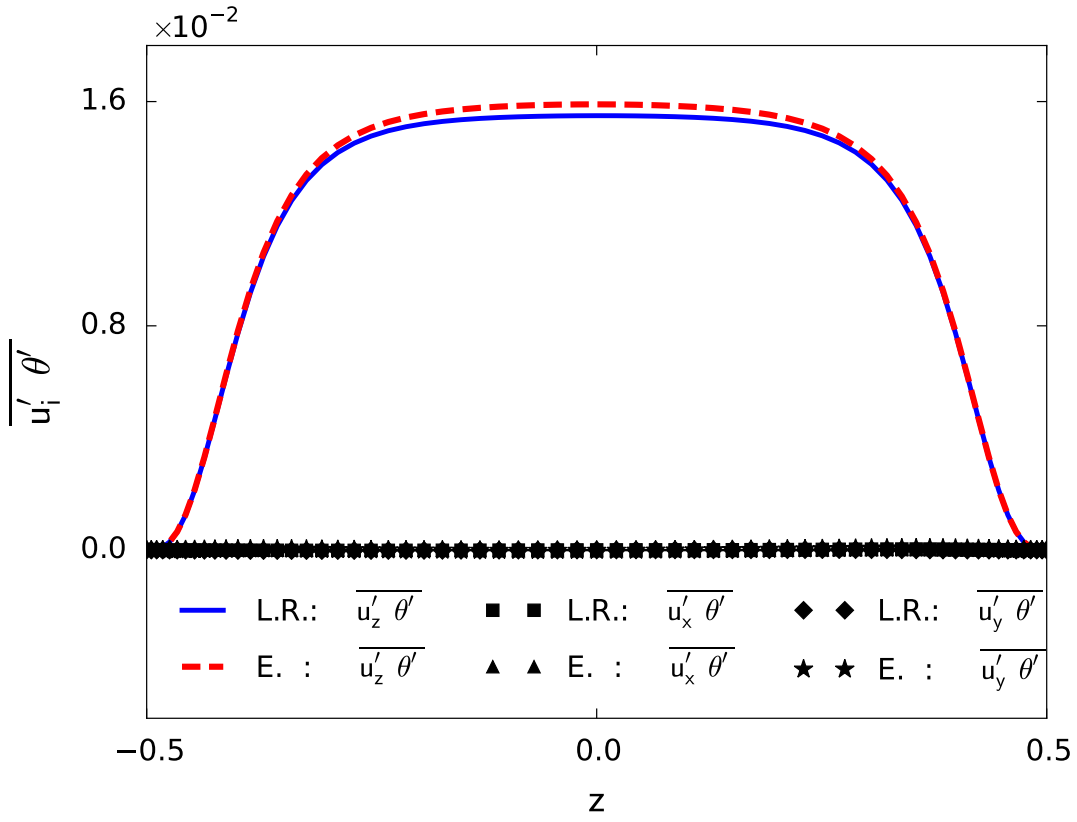

Figure 4.13: The vertical area-averaged profiles of the second-order central moments $\overline{u_i' \theta'}$, $i = \{x, y, z\}$ (the one-point type). Values of the profiles of $\overline{u_x' \theta'}$ and $\overline{u_y' \theta'}$ obtained from both time-averaged and ensemble-averaged data are three orders of magnitude smaller than those of the profiles of $\overline{u_z' \theta'}$.

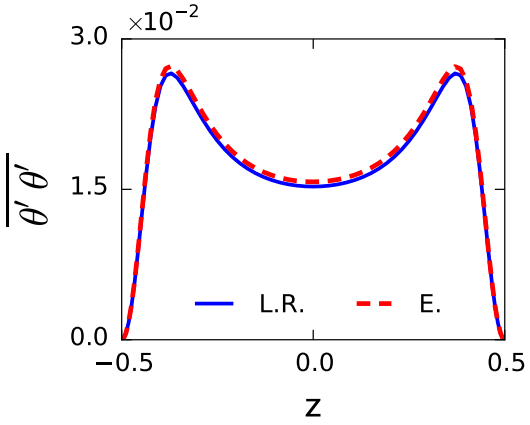

Figure 4.14: The vertical area-averaged profiles of the second-order central moment $\overline{\theta' \theta'}$ (the one-point type). The blue solid curve corresponds to the time averaging. The red dashed curve corresponds to the ensemble averaging.

4.3.6 Spectral analysis

This subsection is devoted to the analysis of one-dimensional spectra obtained for the two-dimensional fields of u_z and T which are used in the analysis in section 4.3.3. This kind of analysis is usually done to determine characteristic scales of structures of averaged 2D fields by determining the wavelength which corresponds to the maximum of a 1D spectrum.

The procedure applied for generating 1D spectra is similar to that used in works [7; 8]. In the present work it is done by performing two steps. First, a 2D field $f = f(x, y)$ is represented by a Fourier series which is obtained by applying the discrete Fourier transform in the x and y directions:

$$\hat{f}(p,q) = \sum_{j=0}^{N_y-1} \sum_{k=0}^{N_x-1} \exp\left(-\frac{2\pi i}{N_X}\, k\, p\right) \exp\left(-\frac{2\pi i}{N_y}\, j\, q\right) f(x_k, y_j), \tag{4.29}$$

where $p = 0, \ldots, N_x - 1$, $q = 0, \ldots, N_y - 1$, and N_x, N_y are the numbers of nodes along x and y, respectively. After shifting zero-frequency components to the center of the 2D spectrum, the obtained field $\hat{f}$ has typically a distinct round spot of large values close to the center. To reduce the complexity of the analysis of the 2D field $\hat{f}$, it is averaged in the azimuthal direction at a fixed radius r starting from the center towards the periphery as follows:

$$E_f(r) = \frac{1}{2\pi} \int_0^{2\pi} \hat{f}\big(x(\phi, r), y(\phi, r)\big)\ \mathrm{d}\phi, \tag{4.30}$$

where $r = 0, 1, \cdots, N_r$, and N_r is some limit which can be equal to $N_x/2$. Values of the wavenumber k which correspond to r are computed as

$$k = \frac{2\pi r}{L}, \tag{4.31}$$

where L is the size of the square (i.e. the length of the rectangular box). It should be noted that the above procedure is applicable when the length of the box is equal to its width (i.e. $L = W$ according to the notation used in figure 1.1(b)).

By applying the above procedure to the 2D fields of the velocity component u_z and the temperature T averaged over time and over the ensemble, the plots of the 1D spectra $E_u(k)$ for u_z and $E_T(k)$ for T are obtained and are shown in figure 4.15 in double logarithmic scale. Figure 4.15(a) stands for the fields of u_z and figure 4.15(b) for the fields of T. In both figures the blue solid curves are the spectra obtained for time-averaged data, and the red dashed curves correspond to the

averaging over the ensemble. It is found that all the spectra in figures 4.15(a) and 4.15(b) have the same value of the wavenumber $k = 1.51$ which corresponds to the extrema of the spectra and which is represented by the vertical black dashed lines in both figures.

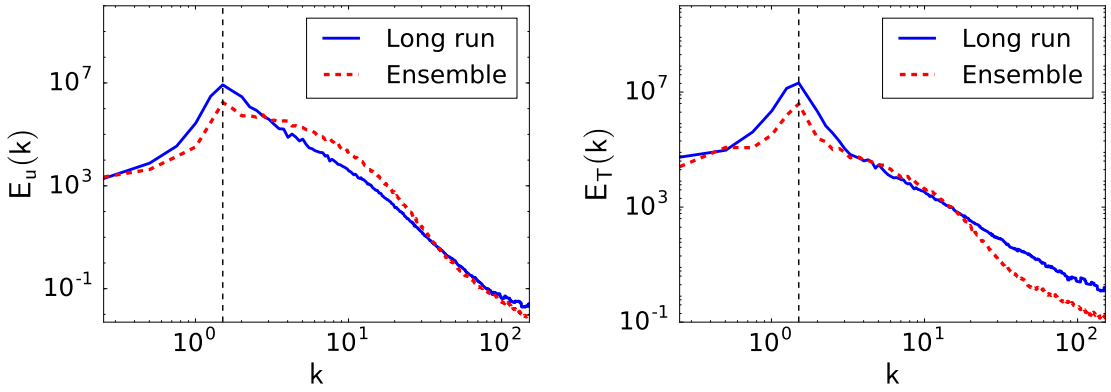

(a) (b)

Figure 4.15: The 1D spectra in the log-log scale obtained by applying procedure described in section 4.3.6 and by using the 2D averaged fields: (a) the velocity component u_z; (b) the temperature T. The applied 2D fields are obtained at the horizontal midplane ($z = 0$) extracted from the corresponding 3D fields. The blue solid curves correspond to the time-averaged data. The red dashed curves correspond to the ensemble-averaged fields. The dashed vertical lines $k = 1.51$ represent the wavenumber which corresponds to the maxima of the spectra.

The further analysis of the 1D spectra is done by the comparison of values of the correlation length ξ applied in [7] and defined as

$$\xi = \frac{1}{\sqrt{\langle k^2 \rangle - \langle k \rangle^2}}, \tag{4.32}$$

where the moments $\langle k \rangle$ and $\langle k^2 \rangle$ are computed as follows

$$\langle k \rangle = \frac{\int_0^\infty k^2 S(k)\,\mathrm{d}k}{\int_0^\infty k S(k)\,\mathrm{d}k} \tag{4.33}$$

$$\langle k^2 \rangle = \frac{\int_0^\infty k^3 S(k)\,\mathrm{d}k}{\int_0^\infty k S(k)\,\mathrm{d}k}. \tag{4.34}$$

The correlation length ξ defined in 4.32 is inversely proportional to the standard deviation, and the decrease in ξ shows how far the state of the system from the

chaotic state. The computed values of ξ are given in table 4.9. It is seen that the relative difference of ξ between the values obtained for the time-averaged and ensemble-averaged fields in the case of the velocity component u_z is 50.86 %, while the same quantity in the case of the temperature T amounts to 4.12 %. The significant difference in ξ can signify that the structures in the patterns of the averaged velocity u_z are more random and decorrelated when averaging over the ensemble than those of the time averaging. This can also be qualitatively observed by comparing the patterns shown in figures 4.7(a) and 4.7(b). As opposed to u_z, the structures recognized in the averaged fields of T are more persistent to the type of averaging, which again can be confirmed by considering the patterns shown in figures 4.7(c) and 4.7(d).

Type of averaging	Velocity component u_z	Temperature T
Time averaging	0.35	0.20
Ensemble averaging	0.17	0.19

Table 4.9: The correlation length ξ computed by (4.32) for the 1D spectra of the 2D fields of the velocity component u_z and the temperature T obtained at the horizontal midplane ($z = 0$) extracted from the corresponding 3D fields and averaged over time and over the ensemble. The relative differences between values of ξ in the cases of u_z and T are 50.86 % and 4.12 %, respectively.

4.3.7 Turbulent viscosity

In this subsection the turbulent (or eddy) viscosity is considered and analysed (see e.g. [16; 57; 58; 61]). The turbulent viscosity is introduced to express the Reynolds stresses π_{ij} defined in dimensionless units as

$$\pi_{ij} = -\overline{u_i' \, u_j'}, \tag{4.35}$$

where u_i', $i = 1, 2, 3$, and u_j', $j = 1, 2, 3$, are the fluctuating parts of the velocity components (in the Cartesian coordinate system) defined in (4.2). The terms π_{ij} given by (4.35) appear in the momentum equation of the system of the Reynolds equations obtained after the procedure of averaging the Navier-Stokes equations described in section 4.1.1. The presence of π_{ij} results in the number of unknowns which is greater than the number of equations, so that the system cannot be solved in a usual way. All efforts to express these second-order moments lead to equations which contain moments of the third order, and the number of equations is again less than the number of unknowns, and so on. This is a well-known closure problem (see e.g. [57; 58]). Thus, to close the system of the Reynolds

equations and to express π_{ij}, it is necessary to include additional assumptions based on dimensional considerations, experimental observations, and so on.

One of the first significant steps to express the Reynolds stresses was done by J. Boussinesq for a simple plane-parallel flow by introducing the concept of the turbulent viscosity included as a coefficient in a relation which is analogous to Newton's law of viscous friction (see e.g. [57; 58]). This equation was generalized to a three-dimensional case when the Reynolds stresses π_{ij}, $i = 1, 2, 3$, $j = 1, 2, 3$, given by (4.35) can be found by using the equation

$$-\overline{u_i' \, u_j'} = -\frac{2}{3} \, b \, \delta_{ij} + \nu_{ijkl} \, \Phi_{kl}, \tag{4.36}$$

where the Einstein summation is applied to the repeated indices, δ_{ij} is the Kronecker delta, the term b is called the turbulent kinetic energy of the fluctuating motion,

$$b = \frac{1}{2} \overline{u_k' \, u_k'}, \tag{4.37}$$

the term Φ_{kl} is computed as

$$\Phi_{kl} = \left(\frac{\partial \overline{u}_k}{\partial x_l} + \frac{\partial \overline{u}_l}{\partial x_k} \right) \tag{4.38}$$

and is equal to the component of the mean rate-of-strain tensor multiplied by a factor of two. The components ν_{ijkl} included in (4.36) are the components of the fourth-rank tensor, which is the generalization of the turbulent viscosity initially introduced by J. Boussinesq (see e.g. [57]). To avoid the analysis of all 81 components ν_{ijkl} of the tensor, it is reasonable to assume a local isotropy of turbulent mixing and to consider one scalar value ν_t instead of the full tensor ν_{ijkl}. Then the following relation between the value ν_t and the Reynolds stress π_{ij} can be written:

$$-\overline{u_i' \, u_j'} = -\frac{2}{3} \, b \, \delta_{ij} + \nu_t \, \Phi_{ij}, \tag{4.39}$$

where Φ_{ij} is computed by using (4.38).

To incorporate the effect of all the components π_{ij} and to eliminate the term with b on the left-hand side of equation (4.39), this equation is multiplied by the term $\partial \overline{u}_i / \partial x_j$, and all the obtained equations for $i = 1, 2, 3$ and $j = 1, 2, 3$ are summed. After completing this procedure, the sum $\partial \overline{u}_i / \partial x_i$ vanishes, because the flow is incompressible, and the following expression is obtained:

$$-\overline{u_i' \, u_j'} \, \frac{\partial \overline{u}_i}{\partial x_j} = \frac{1}{2} \, \nu_t \, \Phi_{ij} \, \Phi_{ij}, \tag{4.40}$$

where the summing on the left-hand side and on the right-hand side is done over the repeated indices i and j, and the term Φ_{ij}^2 appears on the left-hand side of equation (4.40) due to the relation

$$\Phi_{ij}\,\frac{\partial \overline{u}_i}{\partial x_j} = \Phi_{ij}\,\frac{\partial \overline{u}_j}{\partial x_i} = \frac{1}{2}\,\Phi_{ij}\,\Phi_{ij}. \tag{4.41}$$

A more convenient and symmetrical form of equation (4.40) is obtained after a simple transformation which results in the equation

$$-\overline{u_i'\,u_j'}\,\Phi_{ij} = \nu_t\,\Phi_{ij}\,\Phi_{ij}, \tag{4.42}$$

The final equation for computing the turbulent viscosity at any point where the fields of the flow are given is obtained from (4.42):

$$\nu_t = -\frac{\overline{u_i'\,u_j'}\,\Phi_{ij}}{\Phi_{ij}\,\Phi_{ij}}, \tag{4.43}$$

where the summing in the numerator and in the denominator is done over the repeated indices i and j. Values of ν_t computed by (4.43) at grid points are used to obtain the area-averaged profile $\langle \nu_t \rangle_A$ according to the procedure described above in section 4.3.1.

The vertical area-averaged profiles of ν_t computed by (4.43) are shown in figures 4.16(a) and 4.16(b), where the blue solid curves correspond to the time-averaged data of the long-term run, the red dashed curves correspond to the data averaged over the ensemble. The vertical profiles in figure 4.16(a) are obtained by averaging over area of the whole cross section which is described at the end of section 4.3.1 and has the sizes 25×25 (in non-dimensional units). The vertical profiles in figure 4.16(b) are obtained by averaging over a smaller square which is located at the center of the original square and which has the sizes 4.2×4.2 (in non-dimensional units). The second variant of the area used for averaging is applied due to reasons discussed below in this subsection.

One can see in figure 4.16(a) that values of the profile of ν_t in the case of the time-averaged data are greater in magnitude than those of the profile obtained by averaging over the ensemble, which are mostly negative. It should be noted that ν_t obtained from the relation given by (4.36) implies positive values, which means that the turbulent kinetic energy density at corresponding points increases at the expense of the energy of the mean motion. This is a typical situation, which can be expected in such systems as a convection cell. Nevertheless, the

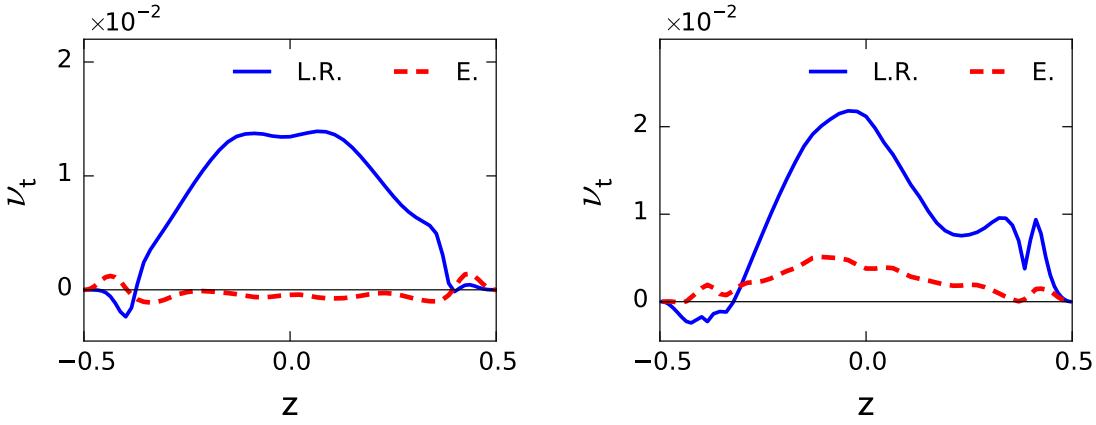

(a) (b)

Figure 4.16: The vertical area-averaged profiles of the turbulent viscosity ν_t computed by equation (4.43). The blue solid curves correspond to the time-averaged data. The red dashed curves correspond to the data averaged over the ensemble. Figure (a): the profiles are obtained by averaging over area of the original square of the sizes 25×25 (a cross section of a horizontal plane and the rectangular box). Figure (b): the profiles are obtained by averaging over area of the smaller square of the sizes 4.2×4.2 located at the center of the original square.

variant of transition of energy in the opposite direction is still possible but in a very specific cases (e.g. atmospheric phenomena). A more detailed discussion on this subject can be found in [57]. Here the negative values of ν_t in the case of the averaging over the ensemble can be attributed to the fact that the hypothesis of the local isotropy used in deriving (4.39) seems not to be valid. The problem can be related to the area applied for computing the area-averaged profiles, namely the square 25×25, which crosses horizontally the whole domain including the bulk and regions of the boundary layers. Particularly the latter can be not suitable for applying the aforementioned hypothesis because of the existence of large gradients of the velocity near the walls.

To confirm this fact, the smaller square of the sizes 4.2×4.2 is used for averaging over area, and the obtained profiles of ν_t are shown in figure 4.16(b), where it is seen that the profile obtained from the data averaged over the ensemble has mostly positive values but still smaller in magnitude in comparison with the case of the time averaging. In the case of the time averaging, the profile of ν_t averaged over the smaller square of 4.2×4.2 and shown in figure 4.16(b) is greater in magnitude than that averaged over the original square and shown in figure 4.16(a). The former is less symmetrical than the latter, which can be explained by

the influence of large-scale structures located chaotically in the cell (the smaller square does not cover all the structures as opposed to the original square). The negative values of the profiles of the turbulent viscosity close to $z = \pm 0.5$ can be also caused by the presence of large gradients of the velocity near the top and bottom plates of the cell. For this reason, the regions near the top and bottom plates should not be taken into account. The maximum values of the profiles of ν_t shown in figures 4.16(a) and 4.16(b) are given in table 4.10. In the case of the area of the smaller square used for averaging, the difference between the maxima of the profiles of time-averaged and ensemble-averaged data amounts to 4.26 times (the third column of table 4.10).

Type of averaging	Original square 25×25	Smaller square 4.2×4.2
Time averaging	1.39×10^{-2}	2.18×10^{-2}
Ensemble averaging	Negative value	5.12×10^{-3}

Table 4.10: The table of the maxima of the vertical area-averaged profiles of the turbulent viscosity ν_t compute by (4.43). The profiles are obtained from the time-averaged data and from the data averaged over the ensemble. The averaging over area is done by applying the original square of the sizes 25×25 and the smaller square of 4.2×4.2.

The turbulent viscosity included in the simplest relation suggested by J. Boussinesq is added to the ordinary molecular viscosity and increases effects of viscosity (see e.g. [58]). A similar statement can be applied to the quantity ν_t introduced in equation (4.39) as a generalization of Boussinesq's assumption. Despite the criticism of this general equation for ν_t (see e.g. [58; 61]), the obtained results shown in figures 4.16(a) and 4.16(b) can reveal some qualitative difference. If equation (4.39) somehow works and the hypothesis of isotropy is valid, the mean flow obtained by averaging over the ensemble has weaker effects related to the overall viscosity due to the turbulent motion than it is in the case of the time averaging. Thus, regardless the quantitative side of the analysis, it seems that the mean flow obtained by applying the two types of averaging has different properties depending on the type of the averaging.

4.3.8 Turbulent thermal diffusivity

In the last part of the analysis the turbulent (or eddy) thermal diffusivity is considered and analysed (see e.g. [16; 57; 58; 61]).

Similar to the turbulent viscosity, the turbulent thermal diffusivity is introduced

to express the turbulent heat fluxes q_i defined in dimensionless units as

$$q_i = -\overline{u_i' \, \theta'}, \tag{4.44}$$

where u_i', $i = 1, 2, 3$, are the fluctuating parts of the velocity components (in the Cartesian coordinate system), and θ' the fluctuating part of the temperature (the corresponding definitions are given in equation (4.2)). The terms defined in (4.44) appear in the energy equation and belongs to the system of the Reynolds equations obtained after the procedure of averaging the Navier-Stokes equations described in 4.1.1. The presence of the terms given by (4.44) also leads to the closure problem discussed above in section 4.3.7.

The turbulent convective heat fluxes q_i, $i = 1, 2, 3$, defined by (4.44) are expressed in almost the same way as the Reynolds stresses in equation (4.36):

$$-\overline{u_i' \, \theta'} = \kappa_{ij} \frac{\partial \overline{T}}{\partial x_j}, \tag{4.45}$$

where the components κ_{ij} are the components of the second-rank tensor. For the sake of simplicity and for rough estimations, assuming the hypothesis of isotropy to be valid (see above in section 4.3.7), the tensor with κ_{ij} can be replaced by one value κ_t resulting in the equation

$$-\overline{u_i' \, \theta'} = \kappa_t \frac{\partial \overline{T}}{\partial x_i}. \tag{4.46}$$

To include the effect of each term $\overline{u_i' \, \theta'}$, equation (4.46) is multiplied by $\partial \overline{T} / \partial x_i$, and the obtained equations for $i = 1, 2, 3$ are summed. After summing, the final equation for computing the turbulent thermal diffusivity κ_t is written as

$$\kappa_t = -\frac{\overline{u_i' \, \theta'} \left(\dfrac{\partial \overline{T}}{\partial x_i} \right)}{\left(\dfrac{\partial \overline{T}}{\partial x_i} \right) \left(\dfrac{\partial \overline{T}}{\partial x_i} \right)} \tag{4.47}$$

where the summing in the numerator and in the denominator is done over the repeated index i. Values of κ_t computed by equation (4.47) at points are used to obtain the vertical area-averaged profile $\langle \kappa_t \rangle_A$ by applying the same procedure (see sections 4.3.1 and 4.3.7).

The area-averaged profiles of the turbulent thermal diffusivity κ_t computed by (4.47) are shown in figures 4.17(a) and 4.17(b), where the blue solid curves correspond to the time-averaged data of the long-term run, the red dashed curves

correspond to the data averaged over the ensemble. The vertical profiles shown in figure 4.17(a) are obtained by averaging over area of the original square of 25×25 (a cross section of a horizontal plane at a fixed z and the rectangular box). The vertical profiles in figure 4.17(b) are obtained by averaging over the smaller square of the sizes 4.2×4.2 used in the analysis in section 4.3.7. The motivation for generating these additional profiles is the same as in the case of the turbulent viscosity, namely to exclude the influence of the boundary layers.

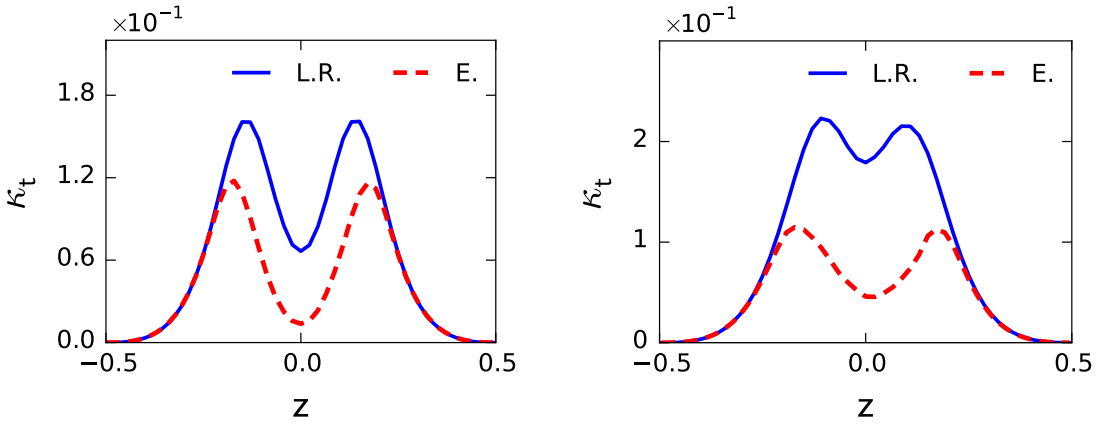

(a) (b)

Figure 4.17: The vertical profiles of the turbulent thermal diffusivity κ_t computed by equation (4.47). The blue solid curves correspond to the time-averaged data. The red dashed curves correspond to the data averaged over the ensemble. Figure (a): the profiles are obtained by averaging over area of the original square of the sizes 25×25 (a cross section of a horizontal plane and the rectangular box). Figure (b): the profiles are obtained by averaging over area of the smaller square of the sizes 4.2×4.2 located at the center of the original square.

In the case of the turbulent thermal diffusivity κ_t, all the area-averaged profiles shown in figures 4.17(a), 4.17(b) have positive values. One can see in both figures that values of the profiles in the case of the time averaging are greater in magnitude than those obtained from the data averaged over the ensemble only in the central part, which corresponds to the bulk of the convection cell. Meanwhile, in both cases of the averaging over area (the original square of 25×25 and the smaller square of 4.2×4.2), the two area-averaged profiles (averaged over time and over the ensemble) coincide in the regions close to $z = \pm 0.5$ (i.e. near the top and bottom plates of the cell). The extrema of the area-averaged profiles are given in table 4.11. As it seen in the table, the difference between the maximum and the minimum of each profile decreases when the area of the smaller square is used for averaging, and this is more prominent in the case of the averaging over the

ensemble. Another notable thing which can be found in table 4.11 and observed in figures 4.17(a), 4.17(b) is that the difference between the maxima of the profiles averaged over time and over the ensemble is much greater in the case of the averaging over the smaller square than in the case of the original square. The same can be said regarding the minima of the area-averaged profiles of κ_t. Thus, the difference between the two profiles becomes more significant when the area of averaging decreases. It is also worth noting that the minima of all the profiles of κ_t are located at the center of the convection cell along the vertical direction ($z = 0$) or very close, as it can be also seen in figures 4.17(a), 4.17(b).

	Original square 25×25		Smaller square 4.2×4.2	
	Minimum	Maximum	Minimum	Maximum
Time averaging	6.65×10^{-2}	1.61×10^{-1}	1.79×10^{-1}	2.23×10^{-1}
Ensemble averaging	1.37×10^{-2}	1.18×10^{-1}	4.56×10^{-2}	1.15×10^{-1}

Table 4.11: The table of extrema of the vertical area-averaged profiles of the turbulent thermal diffusivity κ_t compute by (4.47). The maximum values are found as global, meanwhile the minima are found in the central part, which corresponds to the bulk of the convection cell. Data are averaged over time and over the ensemble. Averaging over area is done by applying the original square of the sizes 25×25 and the smaller square of 4.2×4.2.

The difference in magnitude of values of the area-averaged profiles of κ_t also can confirm the conclusion regarding the turbulent viscosity given at the end of section 4.3.7, and all remarks on the quantity ν_t are related to the turbulent thermal diffusivity as well. The effect of the quantity κ_t can be explained similar to Boussinesq's assumption about the turbulent viscosity: it increases the overall thermal diffusivity and amplifies heat flux due to diffusion. If the hypothesis of isotropy is valid, this effect is more considerable in the case of the time averaging than in the case of the averaging over the ensemble. Thus, the difference in the turbulent thermal diffusivity can signify the difference in the mean flows obtained by the two types of averaging, the averaging over time and the averaging over the ensemble.

4.4 Conclusions

In the present chapter, the data obtained by means of three-dimensional DNS were averaged by the two methods and compared. The analysis provided above in section 4.3 reveals similarity between many integral quantities represented mostly by vertical area-averaged profiles. Nevertheless, there are some features which cannot be considered as completely identical.

It is worth noting that the turbulent flow in the convection system of this large aspect ratio $\Gamma = 25$ achieves the state of a developed turbulent flow at a late time than expected by observing the volume-averaged instantaneous Nusselt number and the instantaneous total kinetic energy given by 4.25 and 4.26, respectively. An interesting question could be, if this property of a flow is observable in other cells of large aspect ratios at different values of the control parameters.

The qualitative difference in coherent structures of the flow is demonstrated in section 4.3.3 by comparing the averaged fields in the horizontal midplane: the velocity component u_z shown in figures 4.7(a) (averaging over time) and 4.7(b) (averaging over the ensemble); the temperature T in figures 4.7(c) (averaging over time) and 4.7(d) (averaging over the ensemble). One can see that the typical roll structures disappear in the case of the ensemble averaging, while those of the time-averaged fields persist after the long period of time used for averaging, $3170\,T_f$ (see table 4.2). Instead of large coherent structures the ensemble-averaged fields consist of structures which are smaller in size and look sharper in terms of magnitude of the quantities than those of the time-averaged fields. The general tendency is that values of the ensemble-averaged fields of u_z and T are smaller in magnitude than those in the case of the time averaging, and this is more notable for T (see table 4.4 and the plots in figure 4.8).

Other quantities such as the Nusselt number, the Reynolds number, the root mean square velocity (see table 4.3) are very close. The same can be said about vertical area-averaged profiles of such quantities as the Reynolds stresses $\overline{u_i' u_i'}$ (not summed over i), $i = \{x, y, z\}$, the turbulent heat flux $\overline{u_z' \theta'}$, and the second-order moments $\overline{u_i u_i}$ (not summed over i), $i = \{x, y, z\}$, which are very identical as well as the profiles of $\overline{u_z T}$, $\overline{\theta' \theta'}$ and of the mean temperature $\overline{T}$. The area-averaged profiles of the quantities $\overline{u_i' u_j'}$ and $\overline{u_i u_j}$, when $i \neq j$, $i = \{x, y, z\}$, $j = \{x, y, z\}$, as well as $u_i' \theta'$ and $u_i T$, $i = \{x, y\}$ were not analysed, because they are much lower in magnitude than those which were compared (see section 4.3.5). The fact that values of these profiles are smaller by several orders of magnitude can signify a weaker correlation between corresponding quantities of the pairs (e.g. u_x and T, or u_x' and θ' in comparison to u_z and T, or u_z' and θ').

The differences were found by analysing the one-dimensional spectra obtained from the two-dimensional fields of u_z and T in section 4.3.6, namely the correlation length ξ computed by (4.32). The correlation length for u_z in the case of the time averaging is greater than the same quantity in the case of the ensemble averaging, while the correlation length for T almost does not change (see table 4.9). This can tell about decorrelated structures observed in the field of u_z. It should be noted

that the scaling of the 1D spectra for both u_z and T shown in figures 4.15(a) and 4.15(b) are similar despite the type of averaging. In other words, the characteristic scale is not forgotten in the ensemble mean.

The final part of the analysis devoted to the turbulent viscosity ν_t and the turbulent thermal diffusivity κ_t also reveals some differences. But it is difficult to rely on these quantities computed by equations (4.43) and (4.47), because their application is very limited and questionable for a turbulent convection flow in a cell (see e.g. [58; 62]). Instead of these simple relations between the Reynolds stresses and the turbulent viscosity, and the heat fluxes and the turbulent diffusivity, it could be more proper to analyse quantities obtained from nonlinear constitutive relations (see e.g. [62]).

To summarize, one can say that the ergodicity is confirmed by our analysis but with some exceptions, which are related to structures of mean flows and which should be further examined. As for analysis, there are still some quantities to be compared in addition to those mentioned above in this section. For example, it would be interesting to analyse spatial correlations and their integrals which determine the length of turbulent structures (see e.g. [16]). It remains open, if a longer run and a larger number of short-term runs lead to completely new results. One more interesting problem is to do similar analysis but for data of a new turbulent convection flow at a higher Rayleigh number. In work [59] mentioned above in section 4.2.2 it is stated that the several regimes of turbulence were found in a convection cell, and one of them, namely the state of "soft" turbulence, is characterized by the lost of the space coherence. The control parameters which correspond to this regime is of a particular interest, while the aspect ratio of a rectangular box could be slightly decreased.

Chapter 5

Summary and outlook

In the present work we studied turbulent Rayleigh-Bénard convection in closed cylindrical and rectangular cells. Two subproblems of convection, which were introduced in section 1.3, were solved, and corresponding numerical and theoretical studies were performed. The first part of the work contains analysis of the boundary layers of a convection flow in a cylindrical cell. The second part is devoted to turbulent convection in a rectangular box and the problem of the ergodicity. This part included the development of the code for solving the elliptic partial differential equations for the pressure and for the temperature. The results of the present work are as follows.

The extended laminar boundary layer model described in chapter 2 does show better agreement between the obtained solutions of the model and the profiles of the data of the DNS for the lower Prandtl number $Pr = 0.7$. As for the higher Prandtl number $Pr = 7$ the inclusion of the buoyancy effect does not influence the result significantly. The reason for this can be the fact that in the fluid with the higher Pr the coherent structure represented by the LSC, which is assumed to induce the prescribed pressure gradient, is much weaker than that in the fluid of the lower Pr. One of possible improvements of the model can be inclusion of additional terms of the series of the solutions, but this inevitably will lead to a more complex system of equations. Another possibility is to consider the buoyancy effect as dominant and to include the effect of the prescribed pressure gradient as small perturbations. In any case, one should remember all deficiencies of the concept of the boundary layer introduced by L. Prandtl, if it is applied to the boundary layers of a turbulent convection flow in a cell.

The developed DNS code in chapter 3 was tested and was applied for numerical simulations needed for studying convection in the container of the large aspect ratio. The potential of the solver has not been yet realized, and large problems

for Rayleigh numbers higher than $Ra = 10^5$ have not been tested so far. However, such problems are interesting, and this would be one task for future research. As the Rayleigh number increases, parameters of turbulent flows and required grids become challenging. First, the influence of the time step of the numerical scheme for such flows becomes essential due to more significant change of a turbulent flow between two sequential moments of time. How the previous solution is useful as an initial guess for a solution on the next time moment is under question. Second, the application of denser grids leads to larger coefficients of the matrix of the linear system, because coefficients of the matrix are inversely proportional to h^2, where h is a space interval. In this regard, the question is related to the stability of the solution method and its behaviour in general.

The problem of the ergodicity given in chapter 4 was studied, and the ergodic hypothesis was confirmed for the particular case of a convection flow, but there is some work which requires further investigations. First, it is not clear, how the results will change, if the number of realizations of the flow (or the number of short-term runs) increases as well as the time for averaging. Second, the analysis was performed thoroughly, but it still does not include all quantities which might be interesting for comparison, and there is some space for the future work. One of problems of such analysis of large data is to find the way for reducing them (e.g. area-averaged profiles, 1D spectra) without losing important features of a turbulent flow. Finally, higher Rayleigh numbers and other states of turbulence should also be investigated, and it is of a special interest, when the spatial coherence is destroyed.

Appendix A

Boundary layer model

A.1 Details on derivation of model equations

In this appendix some derivation steps which are necessary to obtain the four ordinary differential equations of the extended boundary layer model given by (2.39)-(2.42) are provided in more detail. These equations are obtained by substituting series solutions (2.37) and (2.38) into boundary layer equations (2.14)-(2.16). The terms which have the same multipliers ε^m, $m = 0, 1 \ldots$, are grouped together and give corresponding left- and right-hand sides of the equations. First, the velocity components $\tilde{u}$ and $\tilde{w}$ can be expressed via the stream function $\tilde{\psi}(\tilde{x}, \tilde{z})$ in the case of an incompressible flow (see continuity equation (2.15))

$$\tilde{u} = \frac{\partial \tilde{\psi}}{\partial \tilde{z}}, \quad \tilde{w} = -\frac{\partial \tilde{\psi}}{\partial \tilde{x}}. \tag{A.1}$$

By substituting the stream function from (2.37) into (A.1), the following expressions for the components and their partial derivatives are obtained:

$$\tilde{u} = \frac{\tilde{\nu} B^2 n x^{2n-1}}{\tilde{d}} \sum_{m=0}^{\infty} \varepsilon^m f'_m, \tag{A.2}$$

$$\tilde{w} = (-1)\, \frac{\tilde{\nu} B x^{n-1}}{\tilde{d}} \sum_{m=0}^{\infty} \varepsilon^m \big(n f_m + \xi(n-1) f'_m + m(3-5n) f_m \big), \tag{A.3}$$

$$\frac{\partial \tilde{u}}{\partial \tilde{x}} = \frac{\tilde{\nu} B^2 n x^{2n-2}}{\tilde{d}^2} \sum_{m=0}^{\infty} \varepsilon^m \big((2n-1) f'_m + \xi(n-1) f''_m + m(3-5n) f'_m \big), \tag{A.4}$$

$$\frac{\partial \tilde{u}}{\partial \tilde{z}} = \frac{\tilde{\nu} B^3 n^2 x^{3n-2}}{\tilde{d}^2} \sum_{m=0}^{\infty} \varepsilon^m f''_m, \tag{A.5}$$

$$\frac{\partial^2 \tilde{u}}{\partial \tilde{z}^2} = \frac{\tilde{\nu} B^4 n^3 x^{4n-3}}{\tilde{d}^3} \sum_{m=0}^{\infty} \varepsilon^m f'''_m. \tag{A.6}$$

The definitions of B and n follow from (2.27). In addition, the pressure gradient, which is included in momentum equation (2.14), is expressed by applying Bernoulli's equation (assuming the potential flow outside the BL)

$$-\frac{1}{\tilde{\rho}} \frac{\partial \tilde{p}_h}{\partial \tilde{x}} = \tilde{U} \frac{\partial \tilde{U}}{\partial \tilde{x}}, \tag{A.7}$$

which is rewritten by a substitution of the power law for $\tilde{U}$. This results to

$$-\frac{1}{\tilde{\rho}} \frac{\partial \tilde{p}_h}{\partial \tilde{x}} = \frac{\tilde{\nu}^2 B^4 n^2 (2n-1) x^{4n-3}}{\tilde{d}^3} \tag{A.8}$$

where the constant $\tilde{U}_0$ and the power k are expressed via constant B and coefficient n, respectively, according to (2.27).

The integral included in (2.14), which contains the temperature difference $\tilde{T}' = \tilde{T} - \tilde{T}_{mid}$, is expressed via the dimensionless function θ defined in (2.28):

$$\tilde{\alpha} \tilde{g} \int_{\tilde{z}}^{\infty} \frac{\partial}{\partial \tilde{x}} (\tilde{T} - \tilde{T}_{mid})\, \mathrm{d}\tilde{\lambda} = \tilde{\alpha} \tilde{g} \frac{\Delta \tilde{T}}{2} \int_{\tilde{z}}^{\infty} \frac{\partial \theta}{\partial \tilde{x}}\, \mathrm{d}\tilde{\lambda}. \tag{A.9}$$

The variable $\tilde{\lambda}$ in the integral is substituted by a new variable $\hat{\xi}$ according to (2.26) when x is fixed:

$$\hat{\xi} = \frac{\tilde{\lambda}}{\tilde{d}} B n x^{n-1}, \quad \mathrm{d}\tilde{\lambda} = \frac{\tilde{d}}{B n x^{n-1}}\, \mathrm{d}\hat{\xi}. \tag{A.10}$$

With

$$\frac{\partial\theta}{\partial\tilde{x}} = \frac{1}{x\tilde{d}}\sum_{m=0}^{\infty}\varepsilon^m\big(\xi(n-1)\theta'_m + m(3-5n)\theta_m\big), \tag{A.11}$$

one obtains the final expression for the integral in (A.9) which is rewritten with the new variable $\hat{\xi}$ from (A.10):

$$\tilde{\alpha}\tilde{g}\int_{\tilde{z}}^{\infty}\frac{\partial\tilde{T}'}{\partial\tilde{x}}\,\mathrm{d}\tilde{\lambda} = \frac{\tilde{\alpha}\tilde{g}\,\Delta\tilde{T}}{2Bnx^n}\int_{\xi}^{\infty}\Big(\sum_{m=0}^{\infty}\varepsilon^m\big(\hat{\xi}(n-1)\theta'_m + m(3-5n)\theta_m\big)\Big)\,\mathrm{d}\hat{\xi}. \tag{A.12}$$

The substitution of the expressions (A.2)-(A.12) into momentum equation (2.14) and a subsequent grouping terms with the same multiplier ε^m results in the final set of ordinary differential equations (2.39) and (2.41). The other two equations, (2.40) and (2.42), are obtained from the temperature equation (2.16). This equation is changed to an equation for the dimensionless θ as defined in (2.28):

$$\tilde{u}\frac{\partial\theta}{\partial\tilde{x}} + \tilde{w}\frac{\partial\theta}{\partial\tilde{z}} = \tilde{\kappa}\frac{\partial^2\theta}{\partial\tilde{z}^2}, \tag{A.13}$$

where

$$\frac{\partial\theta}{\partial\tilde{z}} = \frac{Bnx^{n-1}}{\tilde{d}}\sum_{m=0}^{\infty}\varepsilon^m\theta'_m, \tag{A.14}$$

$$\frac{\partial^2\theta}{\partial\tilde{z}^2} = \frac{B^2n^2x^{2n-2}}{\tilde{d}^2}\sum_{m=0}^{\infty}\varepsilon^m\theta''_m. \tag{A.15}$$

A.2 Numerical solution of equations

In this section of the appendix, we provide details of the numerical solution of the boundary layer equations. We found that the well-known shooting method, which has been used in the Blasius case, is not applicable for the present set of equations. That is why, a numerical approach similar to the Adams-Bashforth relaxation method is applied in the present work.

To solve (2.39)-(2.42) numerically, the computational domain $\xi \in [0,\, \xi_\infty]$ is divided by M nodes forming a uniform grid with a step size h so that $\xi_i = (i-1)h$, $i = 1, \ldots, M$, $h = \xi_\infty/(M-1)$. Equations (2.39) and (2.41) are non-linear and set a boundary value problem. Equation (2.39) can be written as

$$f_0''' + f_0''f_0 + \beta\big(1 - (f_0')^2\big) = 0. \tag{A.16}$$

Instead of solving equation (A.16), an extended equation is considered which

contains a relaxation term on the left hand side. With a new time-dependent function $F(\xi, \tau)$ introduced, in which τ is a relaxation parameter similar to time, the following equation has to be solved:

$$\frac{\partial F}{\partial \tau} = F''' + F''F + \beta\big(1 - (F')^2\big). \tag{A.17}$$

Here, the derivatives F''', F'' and F' are computed with respect to ξ by applying standard finite difference formulas. The numerical solution of (A.17) requires the extension of the computational domain with respect to τ such that an extended grid consists of uniformly distributed points (ξ_i, τ_j), $i = 1, \ldots, M$, $\Delta\tau = \tau_{j+1} - \tau_j$, $j = 0, 1, 2 \ldots$ The size step $\Delta\tau$ is chosen arbitrarily to achieve numerical stability and convergence. It depends on h. If the auxiliary equation has the solution which does not depend on τ, i.e. $F(\xi, \tau) \to F_\infty$ as $\tau \to \infty$, then the following natural condition is satisfied:

$$\frac{\partial F_\infty}{\partial \tau} = 0. \tag{A.18}$$

In this case, the function F_∞ can be considered as the solution of original Falkner-Skan equation (A.16). The right-hand side of (A.17) is denoted by R so that

$$R = F''' + F''F + \beta\big(1 - (F')^2\big), \quad \frac{\partial F}{\partial \tau} = R. \tag{A.19}$$

From now on, the values of F and R at a point (ξ_i, τ_j) are denoted by F_i^j and R_i^j, respectively, where $i = 1, \ldots, M$, $j = 0, 1, \ldots$ On the one hand, the derivative of F with respect to τ at a point (ξ_i, τ_{j+1}) is expressed by using the one-sided second-order finite difference formula as

$$\Big(\frac{\partial F}{\partial \tau}\Big)_i^{j+1} = \frac{3F_i^{j+1} - 4F_i^j + F_i^{j-1}}{2\Delta\tau} + O(\Delta\tau^2). \tag{A.20}$$

On the other hand, this derivative at the same point (ξ_i, τ_{j+1}) can be extrapolated linearly by uisng the values of R at points (ξ_i, τ_{j-1}) and (ξ_i, τ_j), in the following way:

$$\Big(\frac{\partial F}{\partial \tau}\Big)_i^{j+1} = 2R_i^j - R_i^{j-1} + O(\Delta\tau^2). \tag{A.21}$$

Equations (A.20) and (A.21) give an expression to compute values of F on the level τ_{j+1} at grid points $\xi_3, \xi_4, \ldots, \xi_{M-1}$. This is given by

$$F_i^{j+1} = \frac{1}{3}\left[2\Delta\tau(2R_i^j - R_i^{j-1}) + 4F_i^j - F_i^{j-1}\right]. \tag{A.22}$$

To compute the values of F at the boundary points ξ_1, ξ_2 and ξ_M, the derivatives

$F'(\xi_1)$ and $F'(\xi_M)$ are approximated by the one-sided finite difference formulas, and the boundary conditions written in (2.43) are used:

$$F_1 = 0, \quad F_2 = \frac{1}{4} F_3, \quad F_M = \frac{1}{3} \big(2h + 4F_{M-1} - F_{M-2}\big). \tag{A.23}$$

Thus, by knowing the values of F at the points $\xi_1, \ldots, \xi_M$ on a level τ_j, $j = 0, 1, \ldots$, the values of F at the same points on the new level τ_{j+1} are computed by performing the two steps written in (A.22) and (A.23). In addition, to initialize the iterative procedure, solutions on the levels τ_0 and τ_1 are required. For τ_0 we take an initial guess, for τ_1 we use the simple Euler formula

$$\frac{F_i^1 - F_i^0}{\Delta\tau} = R_i^0, \quad i = 3, \ldots, M-1. \tag{A.24}$$

Again, the remaining values F_1, F_2, F_M on the level τ_1 are computed by using equations (A.23). Finally, the iterative process is stopped when the norm of the difference of two adjacent solutions obtained on timestamps τ_j and τ_{j+1}, $j = 0, 1, \ldots$, is less then a tolerance. This means that the criterion in (A.18) is satisfied. The norm of a function g is computed by searching its supremum over the nodes of the grid:

$$\| g \| = \sup_{i=1,\ldots,M} |g_i| \tag{A.25}$$

The non-linear equation (2.41) is solved by the same procedure together with boundary conditions (2.45). The integral included in this equation is computed by using the trapezoidal algorithm.

For the remaining linear equations (2.40) and (2.42) with their boundary conditions in (2.44) and (2.46), the derivatives of the functions θ_0 and θ_1 at the points $\xi_2, \ldots, \xi_{M-1}$ are replaced with finite differences forming a set of linear algebraic equations. They are written in matrix-vector form, $A\vec{x} = \vec{b}$, and solved by inversion of matrix A:

$$\vec{x} = A^{-1}\vec{b}. \tag{A.26}$$

For the particular case at hand, this matrix is tridiagonal and easily inverted by the tridiagonal matrix algorithm. The values $\theta_j(\xi_1)$, $\theta_j(\xi_M)$, $j = 0, 1$, are determined according to the boundary conditions given in (2.44) and (2.46).

Appendix B

Numerical method for convection in rectangular boxes

In this appendix the main approximations of the Laplacian and the first derivatives on non-uniform regular grids are provided. The seven-point stencil shown in figure 3.3(a) is applied for discretization. At a given node of a regular grid with the coordinates (x_i, y_j, z_k), where i, j, and k are indices which specifies the node along the axes x,y,z, respectively, the entries of the stencil correspond to the following nodes: entry C is the central node with (x_i, y_j, z_k); entry F is the node with (x_{i-1}, y_j, z_k); entry B is the node with (x_{i+1}, y_j, z_k); entry S is the node with (x_i, y_{j-1}, z_k); entry N is the node with (x_i, y_{j+1}, z_k); entry W is the node with (x_i, y_j, z_{k-1}); entry E is the node with (x_i, y_j, z_{k+1}). The arrangement of the stencil entries can be chosen differently, but it must be done explicitly before the formation of the system of linear equations of the form given by (3.22). In the current version of the code for DNS of turbulent convection flows in rectangular boxes this arrangement was done in the way described just above.

B.1 Approximation of the Laplacian on non-uniform grid

In the Cartesian coordinate system the approximation of the second order partial derivatives included in the Laplacian of some function $f = f(x, y, z)$ which is written as

$$\Delta f = \nabla^2 f = \frac{\partial^2 f}{\partial x^2} + \frac{\partial^2 f}{\partial y^2} + \frac{\partial^2 f}{\partial z^2} \tag{B.1}$$

can be done by using the approach described in [63].

In essence, if $\phi = \phi(x)$ is a function known at three successive points with

the coordinates x_{i-1}, x_i, x_{i+1} (non-uniform distribution), its second derivative at point x_i can be found as

$$\left(\frac{\partial^2\phi}{\partial x^2}\right)_i \approx \frac{\left(\frac{\partial\phi}{\partial x}\right)_{i+1/2} - \left(\frac{\partial\phi}{\partial x}\right)_{i-1/2}}{\frac{x_{i+1}-x_{i-1}}{2}}, \tag{B.2}$$

where the first order derivatives included in (B.2) are found at the centers between the three points and are approximated by the central difference scheme as

$$\left(\frac{\partial\phi}{\partial x}\right)_{i+1/2} \approx \frac{\phi(x_{i+1})-\phi(x_i)}{x_{i+1}-x_i}, \qquad \left(\frac{\partial\phi}{\partial x}\right)_{i-1/2} \approx \frac{\phi(x_i)-\phi(x_{i-1})}{x_i-x_{i-1}}. \tag{B.3}$$

By substituting the expressions from (B.3) into (B.2), the final approximation of the second derivative is written as

$$\begin{aligned}\left(\frac{\partial^2\phi}{\partial x^2}\right)_i \approx{}& \frac{2}{(x_{i+1}-x_{i-1})(x_i-x_{i-1})}\,\phi(x_{i-1}) \\ &+ \frac{-2}{(x_{i+1}-x_i)(x_i-x_{i-1})}\,\phi(x_i) \\ &+ \frac{2}{(x_{i+1}-x_{i-1})(x_{i+1}-x_i)}\,\phi(x_{i+1}),\end{aligned} \tag{B.4}$$

which is rewritten in a simpler form as

$$\left(\frac{\partial^2\phi}{\partial x^2}\right)_i \approx \hat{a}_x\,\phi(x_{i-1}) + \hat{b}_x\,\phi(x_i) + \hat{c}_x\,\phi(x_{i+1}). \tag{B.5}$$

If a grid is regular, and the seven-point stencil shown in figure 3.3(a) is applied for discretizing the Laplacian, the approximation (B.4) or (B.5) can be applied for approximating all the second partial derivatives of $f = f(x, y, z)$ included in (B.1). After gathering all the approximations, which have the same form as (B.5), the following approximation of the operator at a node with the coordinates (x_i, y_j, z_k) is obtained:

$$\begin{aligned}\Delta f \approx{}& \hat{a}_x\,f(x_{i-1}, y_j, z_k) + \hat{c}_x\,f(x_{i+1}, y_j, z_k) \\ &+ \hat{a}_y\,f(x_i, y_{j-1}, z_k) + \hat{c}_y\,f(x_i, y_{j+1}, z_k) \\ &+ \hat{a}_z\,f(x_i, y_j, z_{k-1}) + \hat{c}_z\,f(x_i, y_j, z_{k+1}) \\ &+ (\hat{b}_x + \hat{b}_y + \hat{b}_z)\,f(x_i, y_j, z_k).\end{aligned} \tag{B.6}$$

The function f in equation (B.6) is given at nodes which form the seven-point

stencil with the central node at (x_i, y_j, z_k). The coefficients $\hat{a}_*$, $\hat{b}_*$, $\hat{c}_*$, $* = \{x, y, z\}$, included in (B.6) are values of the entries of the stencil of the current node. The Laplacian is approximated at every node of a grid similar to (B.6), and the system of linear equations is obtained. Values of the entries included in (B.6) are modified, if a node is near the boundary or belongs to it. This depends on the type of boundary condition and on the computational strategy in the case of the Neumann condition (see above in sections 3.3.3 and 3.3.4).

B.2 Approximations of the first derivatives on non-uniform grid

To obtain the approximations of the left, right and central derivatives of the first order, the approach suggested in [63] is applied. A function $\phi = \phi(x)$ and its values ϕ_i, $i = 1, 2, 3$, at three successive points x_1, x_2 and x_3 are considered (non-uniform distribution), $\phi_i = \phi(x_i)$, $i = 1, 2, 3$. The function ϕ is approximated by the quadratic polynomial

$$y(x) = \alpha\, x^2 + \beta\, x + \gamma \tag{B.7}$$

which satisfies $y(x_i) = \phi_i$, $i = 1, 2, 3$. The coefficients α, β, γ are defined by knowing ϕ_i, $i = 1, 2, 3$. The approximations of the first derivative of $\phi(x)$ at x_i, $i = 1, 2, 3$ are assumed to be equal to $y'(x_i)$.

The final approximations of $\phi'(x)$ are written as follows.

1. The approximation of the right derivative $\phi'(x)$ at x_1:

$$\begin{aligned}\phi'(x_1) \approx 2\,\alpha x_1 + \beta = {} & \frac{2x_1 - x_2 - x_3}{(x_2 - x_1)(x_3 - x_1)}\,\phi_1 \\ & + \frac{x_3 - x_1}{(x_2 - x_1)(x_3 - x_2)}\,\phi_2 \\ & + \frac{x_1 - x_2}{(x_3 - x_1)(x_3 - x_2)}\,\phi_3.\end{aligned} \tag{B.8}$$

2. The approximation of the central derivative $\phi'(x)$ at x_2:

$$\begin{aligned}\phi'(x_2) \approx 2\,\alpha x_2 + \beta = {} & \frac{x_2 - x_3}{(x_2 - x_1)(x_3 - x_1)}\,\phi_1 \\ & + \frac{x_1 + x_3 - 2x_2}{(x_2 - x_1)(x_3 - x_2)}\,\phi_2 \\ & + \frac{x_2 - x_1}{(x_3 - x_1)(x_3 - x_2)}\,\phi_3.\end{aligned} \tag{B.9}$$

3. The approximation of the left derivative $\phi'(x)$ at x_3:

$$\begin{aligned}\phi'(x_3) \approx 2\,\alpha x_3 + \beta = {} & \frac{x_3 - x_2}{(x_2 - x_1)(x_3 - x_1)}\,\phi_1 \\ & + \frac{x_1 - x_3}{(x_2 - x_1)(x_3 - x_2)}\,\phi_2 \\ & + \frac{2x_3 - x_1 - x_2}{(x_3 - x_1)(x_3 - x_2)}\,\phi_3.\end{aligned} \tag{B.10}$$

Approximations (B.8)-(B.10) can be written in a general form as

$$\phi'(x_i) \approx a_x\,\phi_1 + b_x\,\phi_2 + c_x\,\phi_3 \qquad i = 1, 2, 3. \tag{B.11}$$

In a 3D case of a regular grid, the same approach is applied for approximating the first partial derivatives of a function $f = f(x, y, z)$:

$$\frac{\partial f}{\partial x} \approx a_x\,f(x_{i-1}, y_j, z_k) + b_x\,f(x_i, y_j, z_k) + c_x\,f(x_{i+1}, y_j, z_k), \tag{B.12}$$

$$\frac{\partial f}{\partial y} \approx a_y\,f(x_i, y_{j-1}, z_k) + b_y\,f(x_i, y_j, z_k) + c_y\,f(x_i, y_{j+1}, z_k), \tag{B.13}$$

$$\frac{\partial f}{\partial z} \approx a_z\,f(x_i, y_j, z_{k-1}) + b_z\,f(x_i, y_j, z_k) + c_z\,f(x_i, y_j, z_{k+1}), \tag{B.14}$$

where the partial derivatives are approximated at nodes with (x_i, y_j, z_k) or $(x_{i\pm1}, y_j, z_k)$ for the partial derivative in (B.12), (x_i, y_j, z_k) or $(x_i, y_{j\pm1}, z_k)$ for the partial derivative in (B.13), (x_i, y_j, z_k) or $(x_i, y_j, z_{k\pm1})$ for the partial derivative in (B.14).

The approximations given by (B.12)-(B.14) are applied for incorporating the Neumann boundary conditions in the linear system of the form given by (3.22) according to the second computational strategy describe in section 3.3.4. If the Laplacian is discretized at some node with (x_i, y_j, z_k), and the seven-point stencil with the center at this node has an entry which belongs to a boundary with the Neumann condition (which in turn is reduced to a partial derivative as it is said in section 3.3.1), the corresponding partial derivative is approximated by applying one of the approximations given by (B.12)-(B.14). The node of the entry which belongs to the boundary with the Neumann condition is expressed from the corresponding approximate formula and substituted into the discretization of the Laplacian at the node with (x_i, y_j, z_k) given by (B.6). While doing this, the boundary node is excluded, the value of the opposite entry and of the central entry are modified together with the right-hand side. The example of the use of this approach is given in section 3.3.4. Thus, the solution of the system contains unknowns only at nodes of the internal domain. The solution at nodes of boundaries (with the Neumann condition) are computed by using corresponding approximations, (B.12), (B.13), or (B.14). The edges which belong to two boundaries with the Neumann conditions are not defined and can be computed by extrapolating (see section 3.3.5 and figure 3.4).

Bibliography

[1] L.D. Landau and E.M. Lifshitz. *Fluid Mechanics*, volume 6. Pergamon Press, 2nd edition, 1987.

[2] F. Chillà and J. Schumacher. New perspectives in turbulent Rayleigh-Bénard convection. *Eur. Phys. J. E*, 35:58, 2012.

[3] G. Ahlers, S. Grossmann, and D. Lohse. Heat transfer and large scale dynamics in turbulent Rayleigh-Bénard convection. *Rev. Mod. Phys.*, 81: 503–537, 2009.

[4] S. Chandrasekhar. *Hydrodynamic and Hydromagnetic Stability.* Oxford University Press, 1961.

[5] H. Bénard. Les tourbillons cellulaires dans une nappe liquide. *Rev. Gén. Sciences Pure Appl.*, 11:1261, 1900.

[6] Lord Rayleigh. On convection currents in a horizontal layer of fluid, when the higher temperature is on the under side. *Phil. Mag. Ser.6*, 32:529–526, 1916.

[7] S.W. Morris, E. Bodenschatz, D.S. Cannell, and G. Ahlers. Spiral defect chaos in large aspect ratio Rayleigh-Bénard convection. *Phys. Rev. Lett.*, 71: 2026, 1993.

[8] F. Zhong and R. Ecke. Pattern dynamics and heat transport in rotating Rayleigh-Bénard convection. *Chaos*, 2:163–171, 1992.

[9] S. Grossmann and D. Lohse. Scaling in thermal convection: a unifying view. *J. Fluid Mech.*, 407:27–56, 2000.

[10] E. M. Sparrow and W. J. Minkowycz. Buoyancy effects on horizontal boundary-layer flow and heat transfer. *Int. J. Heat Mass Transfer*, 5:505–511, 1962.

[11] R. J. A. M. Stevens, R. Verzicco, and D. Lohse. Radial boundary layer structure and Nusselt number in turbulent Rayleigh-Bénard convection. *J. Fluid Mech.*, 643:495–507, 2010.

[12] S. Wagner, O. Shishkina, and C. Wagner. Boundary layers and wind in cylindrical Rayleigh-Bénard cells. *J. Fluid Mech.*, 697:336–366, 2012.

[13] N. Shi, M. S. Emran, and J. Schumacher. Boundary layer structure in turbulent Rayleigh-Bénard convection. *J. Fluid Mech.*, 706:5–33, 2012.

[14] J. D. Scheel, E. Kim, and K. R. White. Thermal and viscous boundary layers in turbulent Rayleigh-Bénard convection. *J. Fluid Mech.*, 711:281–305, 2012.

[15] R. Du Puits, L. Li, C. Resagk, A. Thess, and C. Willert. Turbulent boundary layer in high Rayleigh number convection in air. *Phys. Rev. Lett.*, 112:124301, 2014.

[16] H. Schlichting and K. Gersten. *Boundary Layer Theory.* Springer, 8th edition, 2000.

[17] K. Stewartson. On the free convection from a horizontal plate. *Z. Angew. Math. Phys.*, 9a:276–282, 1958.

[18] Z. Rotem and L. Claassen. Natural convection above unconfined horizontal surfaces. *J. Fluid Mech.*, 39:173–192, 1969.

[19] G. S. Gunasegarane and B. A. Puthenveettil. Dynamics of line plumes on horizontal surfaces in turbulent convection. *J. Fluid Mech.*, 749:37–78, 2014.

[20] C. A. Hieber. Mixed convection above a heated horizontal surface. *Int. J. Heat Mass Transfer*, 16:769–785, 1973.

[21] V. M. Falkner and S. W. Skan. Some approximate solutions of the boundary layer equations. *Phil. Mag.*, 12:865–896, 1931.

[22] O. Shishkina, S. Horn, and S. Wagner. Falkner-Skan boundary layer approximation in Rayleigh-Bénard convection. *J. Fluid Mech.*, 730:442–463, 2013.

[23] O. Shishkina, S. Wagner, and S. Horn. Influence of the angle between the wind and the isothermal surfaces on the boundary layer structures in turbulent thermal convection. *Phys. Rev. E*, 89:033014, 2014.

[24] M. Ovsyannikov, D. Krasnov, M.S. Emran, and J. Schumacher. Combined effects of prescribed pressure gradient and buoyancy in boundary layer of turbulent Rayleigh-Bénard convection. *Eur. J. Mech. B/Fluids*, 57:64–74, 2016.

[25] R. Verzicco and R. Camussi. Numerical experiments on strongly turbulent thermal convection in a slender cylindrical cell. *J. Fluid Mech.*, 477:19–49, 2003.

[26] R. Verzicco and P. Orlandi. A finite-difference scheme for three-dimensional incompressible flows in cylindrical coordinates. *J. Comput. Phys.*, 123:402–414, 1996.

[27] J. Bailon-Cuba, M. S. Emran, and J. Schumacher. Aspect ratio dependence of heat transfer and large-scale flow in turbulent convection. *J. Fluid Mech.*, 655:152–173, 2010.

[28] E. Pohlhausen. Der Wärmeaustausch zwischen festen Körpern und Flüssigkeiten mit kleiner Reibung und kleiner Wärmeleitung. *Z. Angew. Math. Mech.*, 1:115–121, 1921.

[29] E. Brown and G. Ahlers. Rotations and cessations of the large-scale circulation in turbulent Rayleigh-Bénard convection. *J. Fluid Mech.*, 568:351–386, 2006.

[30] J. D. Scheel and J. Schumacher. Local boundary layers scales in turbulent Rayleigh-Bénard convection. *J. Fluid Mech.*, 758:344–373, 2014.

[31] O. Shishkina, S. Horn, S. Wagner, and E. S. C. Ching. Thermal boundary layer equation for turbulent Rayleigh-Bénard convection. *Phys. Rev. Lett.*, 114:114302, 2015.

[32] D. Funfschilling, E. Brown, and G. Ahlers. Torsional oscillations of the large-scale circulation in turbulent Rayleigh-Bénard convection. *J. Fluid Mech.*, 607:119–139, 2008.

[33] G. Zocchi, E. Moses, and A. Libchaber. Coherent structures in turbulent convection, an experimental study. *Physica A*, 166:387–407, 1990.

[34] X.-L. Qiu and K.-Q. Xia. Viscous boundary layers at the sidewall of a convection cell. *Phys. Rev. E*, 58:486, 1998.

[35] X.-L. Qiu and K.-Q. Xia. Spatial structure of the viscous boundary layer in turbulent convection. *Phys. Rev. E*, 58:5816, 1998.

[36] C. Sun, Y.-H. Cheung, and K.-Q. Xia. Experimental studies of the viscous boundary layer properties in turbulent Rayleigh-Bénard convection. *J. Fluid Mech.*, 605:79–113, 2008.

[37] Q. Zhou and K.-Q. Xia. Thermal boundary layer structure in turbulent Rayleigh-Bénard convection in a rectangular cell. *J. Fluid Mech.*, 721:199–224, 2013.

[38] Z.A. Daya and R.E. Ecke. Does turbulent convection feel the shape of the container? *Phys. Rev. Lett.*, 87(18):184501, 2001.

[39] J. Wang and K.-Q. Xia. Spatial variations of the mean and statistical quantities in the thermal boundary layers of turbulent convection. *Eur. Phys. J. B*, 32:127–136, 2003.

[40] T. Hartlep, A. Tilgner, and F.H. Busse. Transition to turbulent convection in a fluid layer heated from below at moderate aspect ratio. *J. Fluid Mech.*, 554:309–322, 2005.

[41] M. S. Emran and J. Schumacher. Large-scale mean patterns in turbulent convection. *J. Fluid Mech.*, 776:96–108, 2015.

[42] Y.-B. Xin and K.-Q. Xia. Boundary layer length scales in convective turbulence. *Phys. Rev. E*, 56:3010, 1997.

[43] J.J. Niemela and K.R. Sreenivasan. Turbulent convection at high rayleigh numbers and aspect ratio 4. *J. Fluid Mech.*, 557:411–422, 2006.

[44] D. Krasnov, O. Zikanov, and T. Boeck. Comparative study of finite difference approaches in simulation of magnetohydrodynamic turbulence at low magnetic reynolds number. *Comput. Fluids*, 50:46–59, 2011.

[45] Y. Morinishi, T.S. Lund, O.V. Vasilyev, and P. Moin. Fully conservative higher order finite difference schemes for incompressible flow. *J. Comput. Phys.*, 143:90–124, 1998.

[46] Y. Saad. *Iterative Methods for Sparse Linear Systems*. SIAM, 2nd edition, 2003.

[47] X. Lv and O. Zikanov. Mixed convection in horizontal duct flow with transverse magnetic field and heating of side wall. *Phys. Fluids*, 26:097106, 2014.

[48] P. Swarztrauber and R. Sweet. Efficient fortran subprograms for the solution of elliptic partial differential equations. *NCAR Technical Note IA-109, Boulder*, 1975.

[49] I.S. Duff, A.M. Erisman, and J.K. Reid. *Direct Methods for Sparse Matrices*. Oxford University Press, 2nd edition, 2017.

[50] T.A. Davis. *Direct Methods for Sparse Linear Systems*. SIAM, 2006.

[51] J.J. Dongarra, I.S. Duff, D.C. Sorensen, and H.A. van der Vorst. *Numerical Linear Algebra for High-Performance Computers*. SIAM, 1998.

[52] M.T. Heath, E. Ng, and B.W. Peyton. Parallel algorithms for sparse linear systems. *SIAM Rev.*, 33:420–460, 1991.

[53] P.R. Amestoy, I.S. Duff, J.-Y. L'Excellent, and J. Koster. Parallel algorithms for sparse linear systems. *SIAM J. Matrix Anal. Appl.*, 23:15–41, 2001.

[54] W.L. Briggs, Van Emden Henson, and S.F. McCormick. *A Multigrid Tutorial*. SIAM, 2nd edition, 2000.

[55] R.D. Falgout and U.M. Yang. hypre: A library of high performance preconditioners. *Springer, Berlin, Heidelberg*, 2331:632–641, 2002.

[56] R.D. Falgout, J.E. Jones, and U.M. Yang. The Design and Implementation of hypre, a Library of Parallel High Performance Preconditioners. In A.M. Bruaset and A. Tveito, editors, *Numerical Solution of Partial Differential Equations on Parallel Computers*, volume 51, pages 267–294. Springer-Verlag, 2006.

[57] A.S. Monin and A.M. Yaglom. *Statistical Fluid Mechanics: Mechanics of Turbulence*, volume 1. The MIT Press, 1971.

[58] P.A. Davidson. *Turbulence: An introduction for scientists and engineers*. Oxford University Press, 2004.

[59] F. Heslot, B. Castaing, and A. Libchaber. Transitions to turbulence in helium gas. *Phys. Rev. A*, 36:5870–5873, 1987.

[60] B. Castaing, G. Gunaratne, F. Heslot, L. Kadanoff, A. Libchaber, S. Thomae, X.-Z. Wu, S. Zaleski, and G. Zanetti. Scaling of hard thermal turbulence in Rayleigh-Bénard convection. *J. Fluid Mech.*, 204:1–30, 1989.

[61] S.B. Pope. *Turbulent Flows*. Cambridge University Press, 2000.

[62] D.C. Wilcox. *Turbulence Modeling for CFD*. DCW Industries, 3rd edition, 2010.

[63] J.H. Ferziger and M. Perić. *Computational Methods for Fluid Dynamics*. Springer, 3rd edition, 2002.

Acknowledgements

First of all, I would like to thank my supervisor Prof. Jörg Schumacher for his devoted guidance and for his great support. This work would not be possible without ideas which Professor suggested and which make the work meaningful. We did something new and very interesting, and that required to study deeper some aspects of fundamental and applied science. I am very grateful to Prof. Jörg Schumacher for the important scientific discussions, his help and willingness to share knowledge and experience. I knew a lot of very useful things during my work at the TU Ilmenau, and I highly appreciate the great time I worked in the group of Prof. Jörg Schumacher.

I am very thankful to Dr. Dmitry Krasnov for useful discussions and suggestions on numerical methods and for his code which was generously provided and used as a base for the work on the new numerical method. I would like to thank Dr. Mohammad Emran for his data used in the analysis and for his recommendations on post-processing. I would also like to express my gratitude to Dr. Olga Shishkina for the fruitful discussions on boundary layer models.

Moreover, I wish to thank my colleagues at the Institute of Thermodynamics and Fluid Mechanics of the TU Ilmenau for a friendly healthy working atmosphere. Especially I thank people who helped me so much and gave useful advice on my work, I wish to thank Paul Götzfried, Dr. Ambrish Pandey, Dr. Thomas Boeck, Sebastian Prinz, Prof. Yuri Kolesnikov and Dr. Vinodh Bandaru.

This work was founded by Deutsche Forschungsgemeinschaft with grant FOR 1182. Computer resources were provided by the computing center of the TU Ilmenau, by the Jülich Supercomputing Centre (project HIL10), by the SuperMUC Cluster at the Leibniz Supercomputing Centre Garching (project pr62se).

Finally, I wish to express my gratitude to my parents and other members of my family for their support and encouragement. I would like to thank my small family for their great patience, and especially my wife Yulia for being with me all this time and for her understanding. I also thank members of her family for their timely help and advice.